DIODE LASER PUMPED ND : YAG LASER FOR 946-NM AND ITS FREQUENCY DOUBLING

Junhua Hong

A Thesis Submitted for the Degree of PhD
at the
University of St Andrews

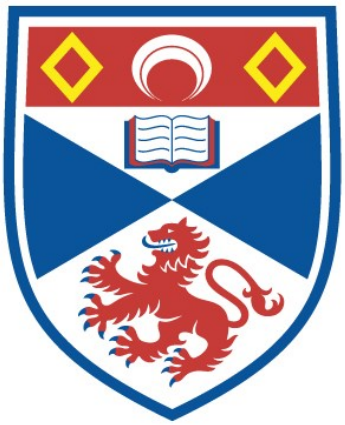

1992

DIODE LASER PUMPED ND:YAG LASER FOR 946-NM AND ITS FREQUENCY DOUBLING

A thesis presented by

Junhua Hong, BSc.

to the

University of St. Andrews

in application for the degree of

Doctor of Philosophy

January 1992

DECLARATION

I, Junhua Hong, hereby certify that this thesis has been composed by myself, that it is a record of my own work, and that it has not been accepted in partial or complete fulfilment of any other degree of professional qualification.

I was admitted to the Faculty of Science of the University of St. Andrews under Ordinance General No. 12 and as a candidate for the degree of Ph.D. in October 1987.

In submitting this thesis to the University of St. Andrews I understand that I am giving permission for it to be made available for use in accordance with the regulations of the University Library for the time being in force, subject to any copyright vested in the work not being affected thereby. I also understand that the title and abstract will be published, and that a copy of the work may be made and supplied to any bona fide library or research worker.

J. Hong

January 1992

CERTIFICATE

I hereby certify that the candidate has fulfilled the conditions of the Resolution and Regulations appropriate to the Degree of Ph.D.

M. H. Dunn

January 1992

ACKNOWLEDGEMENT

I am greatly indebted to Professor Malcolm H. Dunn for his invaluable guidance, continuous encouragement and sincere help throughout the course of this study. I am also much obliged to Dr. Bruce D. Sinclair for his precious time taking up in many useful and informative discussions and advice. I thank all the technical staff of the department, in particular, Mr. Jim Lindsay in the mechanical workshop, for their assistance. I also wish to express my appreciation to the Chinese government and the British Council for granting me a scholarship to study in the United Kingdom. Finally, I own debts of gratitude to my wife and all my friends for their support and understanding over the last few years.

ABSTRACT

The development of a pulsed all-solid-state blue laser system is described in this thesis. The laser system was constructed on the basis of the latest diode laser pumping technology and the availability of the nonlinear material, potassium niobate, in single crystals of high optical quality. With the advantages of diode laser pumping, the 946-nm line in Nd:YAG was successfully made to lase at room temperature, both in cw and Q-switched operation. By frequency doubling the Q-switched 946-nm pulses in a $KNbO_3$ nonlinear crystal, pulses of coherent blue light at a wavelength of 473 nm were obtained with high conversion efficiency.

The 946 nm laser line differs from the more usual transitions used in the Nd:YAG laser in having a lower laser level in the ground state manifold. As a result it experiences significant reabsorption loss due to the (thermally excited) lower level population. Because of this reabsorption loss, the length of the crystal is an important parameter, and as a result of a trade-off between the pumping efficiency and the reabsorption loss, there is an optimum crystal length for every pump power level. A theoretical model was developed to describe this system, and with output coupler transmission, pump beam size and cavity mode size as parameters, optimum conditions for laser oscillation were obtained numerically. The theoretical model was tested with both a diode laser and a Ti:Sapphire laser as a pump source for the 946-nm laser. The theory was found to be in excellent agreement with the results. When pumping with the Ti:Sapphire laser, a slope efficiency of 58 % was obtained with a 2-mm long Nd:YAG crystal, but this dropped to about 11 % with diode laser pumping, which shows the advantage of pumping with a beam of high optical quality.

The Q-switched version of the 946-nm Nd:YAG laser was also studied theoretically, and a modified four level model was developed to describe the dynamic behaviour of the laser in the presence of lower state reabsorption. The relation of this quasi-three level model to the ideal four level model used in the absence of such absorption was explored.

The experiments on Q-switching described here were the first to be reported on the application of this technique to a diode laser pumped 946-nm Nd:YAG laser. Q-switching was achieved by a Brewster-angled acoustic-optic Q-switch, which also acted as a linear polariser. When the laser was pumped by a 0.5 W diode-laser array, pulses with an energy of 4.9 μJ and pulse duration of 68.5 ns were observed at room temperature. Cooling the Nd:YAG crystal to 5 °C improved the laser performance to give pulses of 5.6 μJ pulse energy and 62 ns pulse duration, corresponding to peak powers of 76 W. The pulse repetition rate was kept at 1.5 kHz throughout.

Blue light was generated by passing the 946-nm laser pulses along the a-axis of a 5.1-mm long potassium niobate nonlinear crystal, which was kept at 185 °C to obtain noncritical phase matching. The nonlinear coefficient used in this case was d_{32} (~19.5 pm/V @946 nm). Problems connected with crystal depoling were successfully solved both by the use of a uniform and well controlled temperature environment for the crystal and by providing a poling electric field during heating/cooling. Pulses of coherent blue light at 473 nm with 42 ns duration and 22 W peak power were generated from the output of the 946 nm laser described above, corresponding to an internal peak-power conversion efficiency of 40 %, which was in excellent agreement with the second-harmonic-generation theory.

CONTENTS

Chapter 1

Introduction

1.1 Review of Diode Laser Pumped Solid-State Lasers

The concept of using semiconductor sources to pump solid-state lasers was introduced at a very early stage of laser development. In 1963, Newman was the first investigator [1], to our knowledge, who demonstrated this potential. He found that radiation near 880 nm, which was generated by electron-hole recombination in GaAs light emitting diodes (LED), could excite fluorescence near 1.06 μm in Nd:$CaWO_4$. He also recognised some of the potential advantages of semiconductor pump sources, such as compactness and high efficiencies. As time went on, these advantages were more widely recognised and experimentally demonstrated by other researchers [2-5].

Immediately after the announcement of the first laser based on GaAs in the early sixties [6-8], experimental demonstrations of diode laser pumping of solid-state lasers were reported [9,10]. All these early experiments, whether using LEDs or diode lasers as their pump sources, were performed with very low-power diodes and were often carried out at liquid nitrogen temperature or even at liquid helium temperature to keep the diodes working. Nevertheless, these pioneering experiments demonstrated that a laser system with simple structure, compact size and high efficiency could be expected from diode pumped solid-state lasers.

In the 1970s, the majority of the research work was focused on the

exploration of new laser materials for diode pumping [11-18] and the transverse pumping scheme was still the primary pumping geometry. Since the emission spectra of both the GaAs diode laser and LED can be matched very well with the absorption band of the Nd^{3+} ion, most interest was shown in the materials which contained Nd^{3+} either as a dopant (e.g. Nd:YAG) [11-13] or as a chemical component of the crystal itself (e.g. NdP_5O_{14} [14,15] and $LiNdP_4O_{12}$ [16,17]). At the same time, a different pumping geometry, which is particularly suitable for low power diode laser and LED pumping, was also under investigation, that is, the end-pumping or longitudinal pumping geometry [19]. Although this pumping geometry limits the number of diode lasers or LEDs that can be used, it does offer the advantage of maximum overlap between the pump light and the laser mode. With such a geometry, a cw Nd:YAG laser pumped by a single LED was successfully demonstrated in 1977 [20].

As time went on into the 1980s, enormous improvements in diode-laser technology stimulated growing interest in diode pumped solid-state lasers. The diode laser pumped solid-state laser became a potential rival to the conventional flashlamp pumped solid-state laser, as the diode pumped solid-state laser enjoys the advantages of being all-solid-state. The name of *holosteric* laser (from the Greek, meaning entirely solid) has been coined to describe such systems.

By the early 1990s, diode laser pumped solid-state lasers reached power levels high enough to compete with some of their conventional flashlamp pumped counterparts. This was largely due to the availability of high power diode lasers. Current commercially available quasi-cw diode lasers can provide up to 60 W peak power in a single 10-mm wide linear array (12 mJ per pulse) and 1.5 kW peak power in a 1 cm^2 25-layer array (300 mJ per

pulse) with up to 4% duty factor. Available cw laser diodes can provide up to 20-W power in a single 10-mm linear array. Lifetimes of the order of 10^5-10^6 hours are typical for sub-Watt cw devices. By varying the aluminium content in (GaAl)As laser diodes, devices can be fabricated with emitting wavelengths within the range from 700 nm to 900 nm. Any particular laser can be temperature tuned to set the emission wavelength to coincide exactly with the absorption band of a laser material, thus high pumping efficiency can be achieved. An optical conversion efficiency of 38 % has been reported for a 350-mJ Nd:YAG laser transverse pumped by 16 five-bar diode arrays [21]. Several other rare-earth ions have also been found to have strong absorption bands in this region. These rare-earth ions mostly are trivalent, including Ho^{3+}, Er^{3+}, Tm^{3+}, Pm^{3+} as well as the most familiar Nd^{3+} ion. More specifically, lasing from Ho:YAG (2.1 μm) [22-24], Tm,Ho:YLF (2.07 μm) [25], Tm:YAG (2.02 μm) [26], Er:YLF (2.8 μm) [27], Er doped silica fibre (1.6 μm) [28], and Pm doped phosphate glass (0.933 and 1.098 μm) [29] have been reported. With the availability of high power diode laser pumps, losses due to intracavity wavelength selection elements now can be more readily tolerated and thus lasing at new, but relatively weak, transitions is possible. In Nd^{3+}, two such possible transitions that have been made to oscillate by flashlamp pumping are the $^4F_{3/2}$-$^4I_{9/2}$ at 0.946 μm [30] and $^4F_{3/2}$-$^4I_{15/2}$ at 1.8 μm [31]. There have not been any reports about diode pumped 1.8-μm Nd:YAG lasers, this is probably not just because of the difficulty to make it lase due to its low cross section, but because there are other more efficient laser transitions in other materials available to cover the same wavelength region. The 946-nm line in Nd:YAG has recently attracted considerable attention as blue light can be generated by frequency-doubling this wavelength. Although this transition (and some other transitions, such as the $^5I_5$-$^5I_8$ transition of Ho^{3+}, the $^4I_{13/2}$-$^4I_{15/2}$ transition of Er^{3+} and the $^3F_4$-$^3H_6$ transition of Tm^{3+}) suffers from lower laser level

thermal population, efficient diode laser pumping has already made it a practical and attractive laser line.

To summarize, we can see that diode laser pumping will have a bright future in the development of lasers. Diodes with high electrical-optical conversion efficiency of more than 50 % are commercially available [32], and the excellent wavelength matches between laser diode emission and the absorption bands of solid-state laser materials allow an overall wallplug efficiency of the holosteric laser to be greater than 20 %. The efficient optical pumping means less heat is generated in the solid-state material and thus reduces the requirement for forced air or water cooling of the laser material, which in turn reduces the technical noise, and results in a much more stable device compared to a flashlamp pumped one.

1.2 Compact Blue and Green Laser Devices

A major motivation behind the development of compact blue and green laser devices is the large potential commercial markets, including optical data storage and laser printing. The commercial devices in these fields are currently working in the red or near infrared regions based on either semiconductor diode lasers themselves or HeNe lasers. Other applications of current interest requiring compact sources of blue or green light include undersea communications and large-screen displays.

Different approaches have been taken to develop such compact blue/green sources. The most direct approach, of course, is the diode laser itself emitting in this wavelength region. But so far the shortest wavelength of commercial products has only been pushed down to about 630 nm with

InGaAlP as its semiconductor materials [35]. In the laboratory, though, diode lasers made of the same material have been reported emitting in the yellow at 576 nm at a temperature of 109 K [36]. Although, the development of III-V diode lasers, in particular the GaAlAs diode laser, is approaching maturity, new opportunities for yet shorter wavelength are to be found in the high band-gap II-VI diodes. Only very recently, the first diode lasers fabricated from II-VI semiconductors have been demonstrated [37]. These devices emit light at a wavelength of 490 nm from a ZnSe-based single-quantum-well structure under pulsed current injection at 77 K. The most serious problem associated with these devices is the poor electrical contact between the Au electrode and the p-ZnSe, which generates considerable amount of heat, so a practical blue diode laser is probably still some years away.

The practical approaches for generating blue and green laser light at the moment are to use nonlinear crystals to frequency-double infrared light from either III-V diode lasers or diode laser pumped solid-state lasers. Also currently under investigation are some new exotic laser gain materials which can either double the laser frequency themselves or can be upconversion excited [38,39].

To gain an overview of recent developments in compact blue and green sources, we will summarise some of the work carried out to date. As the development of blue/green diode lasers is still in the experimental stage, the most basic approach is to frequency upconvert current commercial infrared diode lasers. A schematic set-up of such a device is shown in Fig. 1.2.1. The efficiency of the second harmonic generation process, as will be discussed in chapter 6, depends strongly on beam quality and optical power of the fundamental wave. Since the power of the most successful GaAlAs diode

lasers with good spatial and spectral mode properties is just over the 100 mW level, the simple configuration shown in Fig. 1.2.1 exhibits poor conversion efficiency, even with the best nonlinear crystals available today.

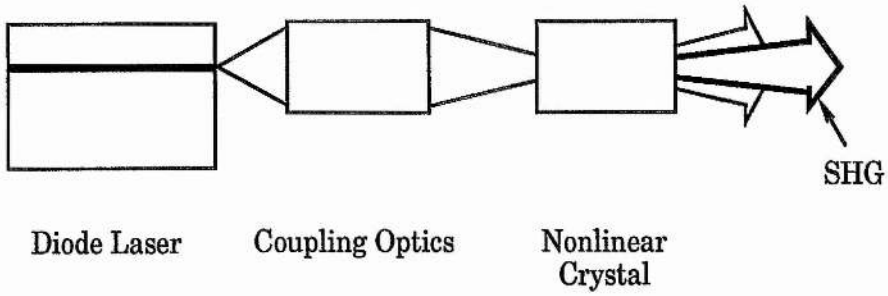

Figure 1.2.1 Schematic diagram of direct frequency doubling of a diode laser

Early studies in nonlinear optics have suggested some ways of increasing conversion efficiency by enhancing either the fundamental or second harmonic field in a passive resonator, or, if it is technically achievable, enhancing both the fundamental and the harmonic fields in a single passive resonator [40]. The most practical and widely studied way among these three has proved to be the first one, the fundamental enhancement scheme.

Of such schemes, the monolithic MgO:$LiNbO_3$ ring resonant cavity, which was first designed for frequency doubling the diode laser pumped cw 1.064-nm Nd:YAG laser [41], has been particularly successful. The recent $KNbO_3$ version of such a ring resonant cavity [42] has proved to be an efficient device in direct frequency doubling of GaAlAs diode lasers. As much as 41 mW of blue light at 428 nm has been generated from 140-mW of 856-nm diode laser input with this resonator [42]. The basic requirement for a field enhancement scheme is to match either the resonant frequency

of the passive resonator to the optical frequency or vice versa. In Fig. 1.2.2, the latter approach was chosen. The frequency of the diode laser was actively locked to the resonant frequency of the passive nonlinear cavity by a electronic feedback control loop. Another interesting locking technique, which utilises the optical response property of diode lasers, was demonstrated in Ref. [43], where optical feedback from the passive resonator successfully locked the frequency of the diode laser.

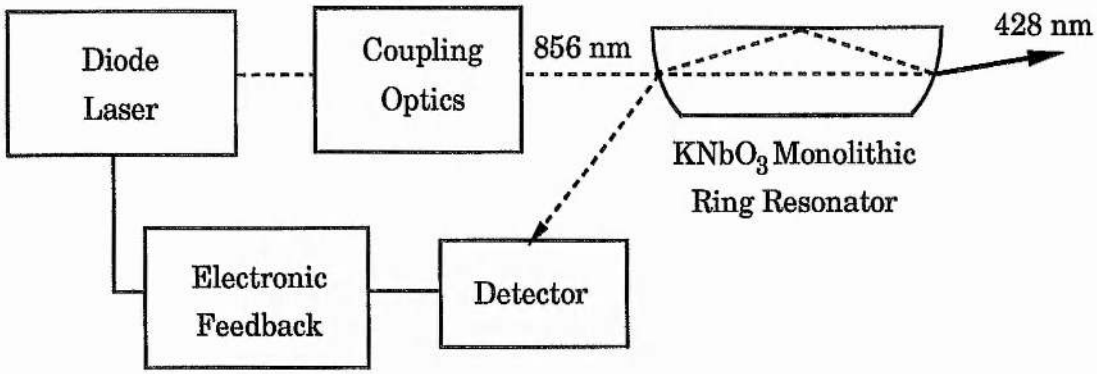

Figure 1.2.2 Schematic experimental diagram for generation of 428-nm light by direct frequency doubling of a GaAlAs laser diode using a monolithic ring resonator for efficiency enhancement

Second harmonic generation in the form of Cerenkov radiation has attracted considerable attention recently. The experiment for direct second harmonic generation of diode laser radiation with such doubling scheme was first demonstrated by using a proton exchanged lithium niobate waveguide [44]. Further investigations in this field have been carried out with other nonlinear waveguides, such as $TiO_2/LiNbO_3$ and KTP waveguides. The study of $TiO_2/LiNbO_3$ waveguide showed that the zero nonlinear coefficient of the TiO_2 guiding layer actually increases the conversion efficiency [45].

Having discussed the concepts of second harmonic generation, it is natural to accept the idea of frequency doubling compact infrared solid-state lasers. As a matter of fact, the historic development sequence is just the opposite, since the diode laser pumped solid-state laser met both the optical quality and power requirements for efficient nonlinear optical process long before the diode lasers. And these advantages of the diode laser pumped solid-state lasers remain today.

The TEM_{00} spatial mode and narrowband spectrum of diode laser pumped solid-state lasers make them ideal sources for efficient second harmonic generation. Experience gained from second harmonic generation of flashlamp pumped systems greatly facilitated the development of frequency doubled diode laser pumped solid-state lasers. Frequency doubled diode pumped cw Nd:YAG lasers based on the use of potassium titanyl phosphate (KTP) have already been commercially introduced. However, with these early commercial intracavity frequency doubled green lasers, the problem of large-amplitude fluctuations at the green wavelength was observed [46]. This was due to mode coupling between different longitudinal modes. To solve the problem, three other design routes have been investigated for low noise frequency doubled diode pumped Nd:YAG lasers. The first design route is to operate the Nd:YAG laser in a single longitudinal mode so that the mode coupling is nonexistent. The second is to use an external cavity to allow the Nd:YAG resonator and doubling resonator to be isolated from each other. By the combination of nonlinear ring laser oscillator design [33] and monolithic $MgO:LiNbO_3$ ring cavity doubler, 29.7 mW of single axial mode 532-nm radiation was produced when pumped with a 500 mW diode laser [41].

The third option is single-pass external frequency doubling of a Q-

switched diode pumped solid-state laser, which is the option discussed in this thesis. In later chapters, more detailed discussion about this will be given.

New high quality materials that have been developed recently have led to some exciting progress in the nonlinear optics and solid-state laser fields. One group of these newly developed materials includes Nd:MgO:$LiNbO_3$ and Nd:YAB ($Nd_xY_{1-x}Al_3(BO_3)_4$) which can act both as active laser materials and nonlinear materials, and are commonly referred to as self-doubling materials. The diode laser pumped Nd:YAB laser has produced up to 23 mW of laser output at 531 nm in the green with an incident diode laser pumping power of 375 mW at 800 nm [38]. Fig. 1.2.3 shows the diode laser pumped Nd:YAB system. The main advantage of self-doubling laser is its simple structure, which not only converts the multi diode laser modes into diffraction limited TEM_{00} solid-state laser mode, but also doubles the laser frequency into the visible range. Because of its self-doubling capability, such a device eliminates the use of expensive and quantity limited nonlinear crystals in the present commercial compact green lasers, which may open up a bright future for these self-doubling devices.

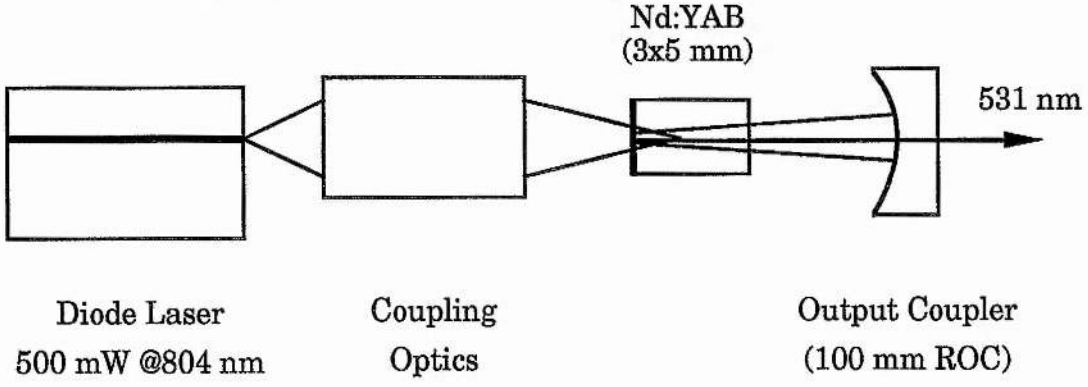

Figure 1.2.3 Diode laser pumped self-doubling Nd:YAB laser

A new pumping scheme, which introduces another group of laser materials, is the two-photon excitation process, which includes sequential two-step absorption and energy transfer upconversion. Both these pumping mechanisms have been demonstrated with erbium doped hosts. Fig. 1.2.4 and 1.2.5 illustrate these two pumping schemes with Er:$YAlO_3$ and Er:$YLiF_4$ respectively. Erbium doped hosts exhibit strong absorption lines in the wavelength range of GaAlAs diode laser emission, and they are the only choices for diode laser pumping at the moment. The best result so far was obtained with the experimental configuration shown in Fig. 1.2.6. An output power of 2.3 mW at 550 nm was reported with 95 mW of pump power at 802 nm from a single-frequency GaAlAs diode laser [39].

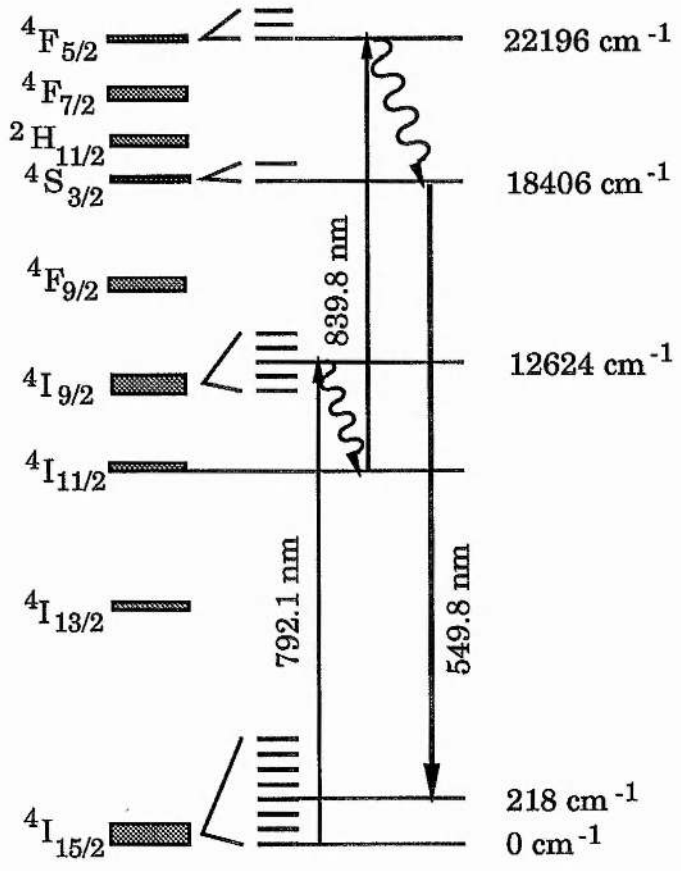

Figure 1.2.4 Two-photon sequential pumping scheme of Er:$YAlO_3$

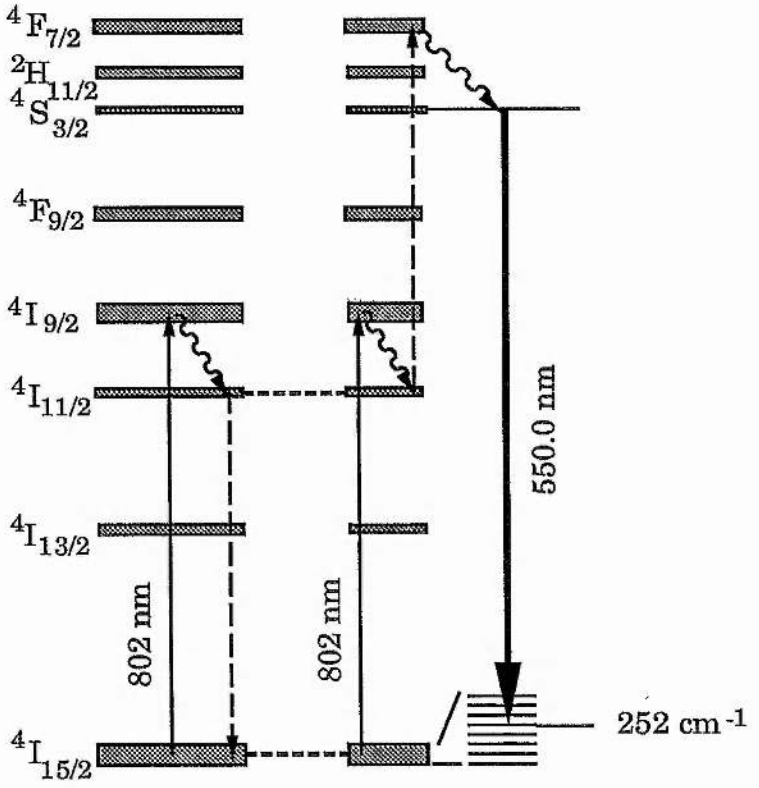

Figure 1.2.5 Energy transfer pumping scheme of Er:$YLiF_4$

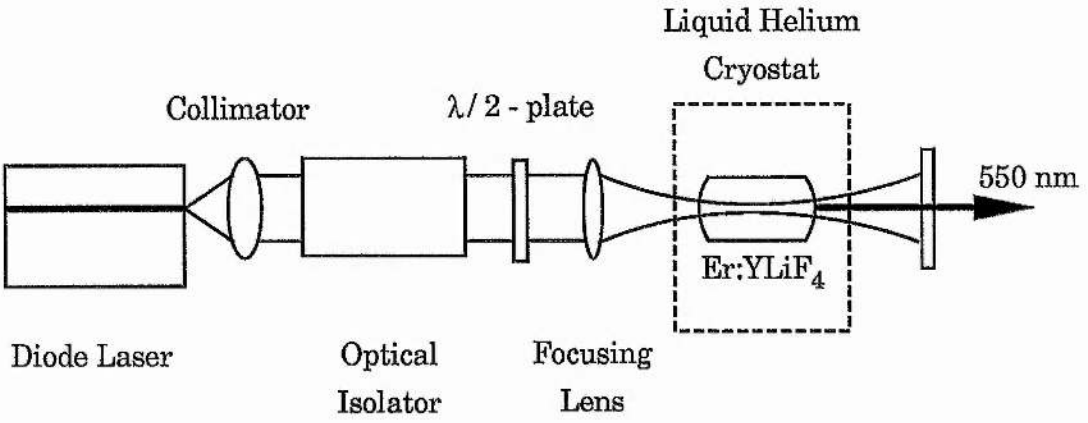

Figure 1.2.6 Experimental setup of diode laser pumped Er:$YLiF_4$ upconversion laser

The increasing spectral coverage of diode lasers, due to the introduction of strained-layer InGaAs lasers in the 900-nm to 1100-nm range and the quaternary AlGaInP lasers in the visible red range, enlarges the choices of laser and nonlinear materials. In the near future, compact blue and green lasers will meet most application requirements, not just in terms of optical performances but also in terms of single unit price.

Our contribution to the development of all-solid-state blue lasers was a research project investigating a rarely used laser line, at 946 nm, in Nd:YAG pumped by a diode laser and frequency doubling of this line. Further investigations were carried out on Q-switching of this diode laser pumped Nd:YAG laser and on second harmonic generation of this line with potassium niobate ($KNbO_3$) crystals. In the following chapter, we review the physics and technology of diode lasers. The theories of cw and Q-switched quasi-three level laser systems are given in chapter 3, and chapter 4 respectively. In chapter 5, the designs and details of the laser systems are described, and experimental results of both the cw and the Q-switched 946-nm Nd:YAG lasers are discussed. The theory and some interesting phase matching methods of second harmonic generation are discussed in chapter 6. In chapter 7 some nonlinear crystals considered to be suitable for frequency doubling the 946-nm light are evaluated, in particular, some special properties of potassium niobate crystals are discussed, and the results of SHG in potassium niobate are presented. Finally, in the conclusion, we summarise the achievements of this work, and discuss how further improvements in the performance of the laser systems may be brought about.

References

[1] R. Newman, "Excitation of the Nd^{3+} fluorescence in $CaWO_4$ by recombination radiation in GaAs", *J. Appl. Phys.*, Vol. 34, No. 2, (1963) 437;

[2] S. A. Ochs and J. I. Pankove, "Injection-luminescence pumping of a $CaF_2:Dy^{2+}$ lasser", *Proc. IEEE* , Vol. 52, No. 6, (1964) 713;

[3] R. B. Allen and S. J. Scalise, "Continuous operation of a YAIG:Nd laser by injection luminescent pumping", *Appl. Phys. Lett.*, Vol. 14, No. 6, (1969) 188;

[4] F. W. Ostermayer, Jr., R. B. Allen and E. G. Dierschke, "Room-temperature cw operation of a $GaAs_{1-x}P_x$ diode-pumped YAG:Nd laser", *Appl. Phys. Lett.*, Vol. 19, No. 8, (1971) 289;

[5] H. G. Danielmeyer and F. W. Ostermayer, Jr.,"Diode-pumped-modulated Nd:YAG laser", *J. Appl. Phys.*, Vol. 43, No. 6, (1972) 2911;

[6] R. N. Hall, G. E. Fenner, J. D. Kingsley, T. J. Soltys and R. O. Carlson, "Coherent light emission from GaAs junctions", *Phys. Rev. Lett.*, Vol. 9, No. 9, (1962) 366;

[7] M. I. Nathan, W. P. Dumke, G. Burns, F. H. Dill, Jr. and G. J. Lasher, "Stimulated emission of radiation from GaAs p-n junction", *Appl. Phys. Lett.*, Vol. 1, No. 3, (1962) 62;

[8] T. M. Quist, R. H. Rediker, R. J. Keyes, W. E. Krag, B. Lax, A. L. McWhorter and H. J. Zeiger, "Semiconductor maser of GaAs", *Appl. Phys. Lett.*, Vol. 1, No. 4, (1962) 91;

[9] R. J. Keyes and T. M. Quist, "Injection luminescent pumping of $CaF_2:U^{3+}$ with GaAs diode lasers", *Appl. Phys. Lett.*, Vol. 4, No. 3, (1964) 50;

[10] M. Ross, "YAG laser operation by semiconductor laser pumping", *Proc. IEEE* , Vol. 56, No. 2, (1968) 196;

[11] L. C. Conant and C. W. Reno, "GaAs laser diode pumped Nd:YAG laser", *Appl. Opt.*, Vol. 13, No. 11, (1974) 2457;

[12] J. E. Jackson and R. R. Rice, "Output fluctuations of high-frequency pulse-pumped Nd:YAG laser", *J. Appl. Phys.*, Vol. 45, No. 5, (1974) 2353;

[13] G. I. Farmer and Y. C. Kiang, "Low-current-density LED-pumped Nd:YAG laser using a solid cylindrical reflector", *J. Appl. Phys.*, Vol. 45, No. 3, (1974) 1356;

[14] H. P. Weber, "Nd pentaphosphate lasers", *Opt. Quantum Electron.*, Vol. 7, (1975) 431;

[15] S. R. Chinn, J. W. Pierce and H. Heckscher, "Low-threshold transversely excited NdP_5O_{14} laser", *Appl. Opt.*, Vol. 15, No. 6, (1976) 1444;

[16] M. Saruwatari, T. Kimura and K. Otauka, "Miniaturized cw $LiNdP_4O_{12}$ laser pumped with a semiconductor laser", *Appl. Phys. Lett.*, Vol. 29, No. 5, (1976) 291;

[17] K. Kubodera and K. Otsuka, "Efficient $LiNdP_4O_{12}$ lasers pumped with a laser diode", *Appl. Opt.*, Vol. 18, No. 23, (1979) 3882;

[18] B. I. Denker, A. A. Izyneev, I. I. Kuratev, Yu. V. Tsvetkov and A. V. Shestakov, "Lasing in phosphate glasses with high neodymium ion concentrations under pumping with light-emitting diodes", *Sov. J. Quantum Electron.*, Vol. 10, No. 9, (1980) 1167;

[19] L. J. Rosenkrantz, "GaAs diode-pumped Nd:YAG laser", *J. Appl. Phys.*, Vol. 43, No. 11, (1972) 4603;

[20] F. W. Ostermayer, Jr., "LED end-pumped Nd:YAG lasers", *IEEE J. Quantum Electron.*, Vol. QE-13, No. 1, (1977) 1;

[21] R. L. Burnham, "High-power transverse diode-pumped solid-state lasers", *Opt. & Photonics News*, Aug., (1990) 4;

[22] R. Allen, L. Esterowitz, L. Goldberg, J. R. Weller and M. Storm, "Diode-pumped 2 μm holmium laser", *Electron. Lett.*, Vol. 22, No. 18, (1986) 947;

[23] T. Y. Fan, G. Huber, R. L. Byer and P. Mitzscherlich, "Continuous wave operation at 2.1 μm of a diode laser pumped, Tm-sensitized Ho:$Y_3Al_5O_{12}$ laser at 300 K", *Opt. Lett.*, Vol. 12, No. 9, (1987) 678;

[24] J. M. Fujimoto and S. J. Brosnan, "Q-switched operation of a continuous wave pumed Tm,Ho:YAG laser at 300 K", CLEO 89, (1989) paper TUE4;

[25] H. Hemmati, "2.07 μm cw diode-laser-pumped Tm,Ho:$YLiF_4$ room-temperature laser", *Opt. Lett.*, Vol. 14, No. 9, (1989) 435;

[26] G. J. Kintz, R. Allen and L. Esterowitz, "Continuous-wave laser emission at 2.02 μm from diode-pumped Tm^{3+}:YAG at room temperature", CLEO 88, (1988) paper FB2;

[27] G. J. Kintz, R. Allen and L. Esterowitz, "CW and pulsed 2.8 μm laser emission from diode-pumped Er^{3+}:$LiYF_4$ at room temperature", *Appl. Phys. Lett.*, Vol. 50, No. 22, (1987) 1553;

[28] L. Reekie, I. M. Jauncey, S. B. Poole and D. N. Payne, "Diode-laser-pumped operation of an Er^{3+} doped single-mode fibre laser", *Electron. Lett.*, Vol. 23, No. 20, (1987) 1076;

[29] W. F. Krupke, M. D. Shinn, T. A. Kirchoff, C. B. Finch and L. A. Boatner, "Promethium-doped phophate glas laser at 933 and 1098 nm", *Appl. Phys. Lett.*, Vol. 51, No. 26, (1987) 2186;

[30] R. W. Wallace and S. E. Harris, "Oscillation and doubling of the 0.946 μ line in Nd^{3+}:YAG", *Appl. Phys. Lett.*, Vol. 15, No. 4, (1969) 111;

[31] R. W. Wallace, "Oscillation of the 1.833 μ line in Nd^{3+}:YAG", *IEEE J. Quantum Electron.*, Vol. QE-7, No. 5, (1971) 203;

[32] W. Streifer, D. R. Sefres, G. L. Harnagel, D. F. Welch, J. Berger, and M. Sakamoto, "Advances in diode laser pumps", *IEEE J. Quantum Electron.*, Vol. QE-24, No. 6, (1988);

[33] T. J. Kane, A. C. Nilson and R. L. Byer, "Frequency stability and offset locking of a laser-diode-pumped Nd:YAG monolithic nonplanar ring oscillator", *Opt. Lett.*, Vol. 12, No. 3, (1987) 175;

[34] W. R. Trutna, D. K. Donald and M. Nazarathy, "Unidirectional diode-laser-pumped Nd:YAG ring laser with a small magnetic field", *Opt. Lett.*, Vol. 12, No. 4, (1987)

248;

[35] *Lasers & Optronics*, Vol. 9, No. 3, (1990) 7;

[36] Y. Kaneko, A. Kikuchi, I. Nomura and K. Kishno, "Yellow (576-nm) laser emission from (GaInP/AlInP) MQW/AlInP double heterostructure at 109 K", CLEO 90, (1990) paper CMC4;

[37] M. A. Haase, J. Qiu, J. M. DePuydt and H. Cheng, "Blue-green laser diodes", *Appl. Phys. Lett.*, Vol. 59, No. 11, (1991) 1272;

[38] "Nd:YAB laser outputs green light for use in electronics", *Laser Focus World*, April (1990) 27;

[39] T. Herbert, W. P. Risk, R. M. Macfarlane and W. Lenth, OSA Topical Meeting on Advanced Solid-state Lasers, Salt Lake City, Utah, (1990) paper WE5.

[40] A. Ashkin, G. D. Boyd and J. M. Dziedzic, "Resonant optical second harmonic generation and mixing", *IEEE J. Quantum Electron.*, Vol. QE-2, No. 6, (1966) 109;

[41] W. J. Kozlovsky, C. D. Nabors and R. L. Byer, "Efficient second harmonic generation of a diode-laser-pumped cw Nd:YAG laser using monolithic MgO:$LiNbO_3$ external resonant cavityies", *IEEE J. Quantum Electron.*, Vol. QE-24, No. 6, (1988) 913;

[42] W. J. Kozlovsky, W. Lenth, E. E. Latta, A. Moser and G. L. Bona, "Generation of 41 mW of blue radiation by frequency doubling of a GaAlAs diode laser", *Appl. Phys. Lett.*, Vol. 56, No. 23, (1990) 2291;

[43] G. J. Dixon, C. E. Tanner and C. E. Wieman, "432-nm source based on efficient second-harmonic generation of GaAlAs diode-laser radiation in a self-locking external resonant cavity", *Opt. Lett.*, Vol. 14, No. 14, (1989) 731;

[44] G. Tohmon, K. Yamamoto and T. Taniuchi, "Blue light source using guided-wave frequency doubler with a diode laser", SPIE, Vol. 898, (1988) 70;

[45] T. Fujiwara, Y. Fujino and Y. Tanabe, "Cerenkove radiation from TiO_2/$LiNbO_3$

nonlinear waveguides", CLEO-90, (1990) paper CFE 1;

[46] T. Baer, "Laser-amplitude fluctuations due to longitudinal mode coupling in diode-pumped intracavity-doubled Nd:YAG lasers", *J. Opt. Soc. Amer. B*, Vol. 3, No. 9, (1986) 1175;

Chapter 2

Diode Lasers

2.1 Introduction

The development of semiconductor pumped solid-state lasers, as described in the previous chapter, is now into the production phase. The potential advantages of diode laser pumped solid-state lasers, or in other words, holosteric (all-solid-state) lasers, have been realised in practice and experimentally demonstrated, which greatly stimulates further research and development in this field. The recent renaissance in the solid-state laser field, however, resulted largely from advances in the area of diode lasers, in particular, of (GaAl)As diode lasers. This chapter reviews the physics and technology of the diode laser pump source.

The heart of a holosteric laser is the solid-state pumping source, and it is the diode laser pump which makes the holosteric laser so different from conventional flashlamp pumped solid-state lasers. The advantages of compactness, high efficiency and long life, of diode pumped lasers have been mentioned in the previous chapter. In this chapter, background and the fundamental properties of diode lasers are reviewed. Here, the diode lasers particularly refers to those injection semiconductor lasers where a p-n heterojunction is used to inject excess electrical carriers into the active region. Some other pumping mechanisms have also been demonstrated, such as optically pumped semiconductor lasers, where an external light source produces excess carriers, and electron-beam pumped diode lasers, which use high energy electrons to produce the excess carriers, but these

two types of diode laser pumping are not really practical. They are currently only being used for experimental purposes in the study of semiconductors.

For a pump source, the general interests of a diode laser are its output power, electrical-optical conversion efficiency, brightness, spectral width, temperature and current tunability, and output beam properties, such as transverse mode structure, beam divergence, asymmetry, and astigmatism. In the following sections, we are going to discuss these aspects of diode lasers to some extent, but detailed mathematical work will only be referenced.

2.2 Output Powers

Diode laser pumping has greatly inspired the development of high power diode lasers which in turn drive the development of holosteric lasers. The maximum output power, or rather the maximum optical intensity, is limited by facet and internal damage of the diode at high optical flux density. The lifetime of a diode laser is thus believed to be an inverse function of output power [1].

Facet damage can be subdivided into "catastrophic" degradation and facet "erosion", where the former refers to rapid mechanical damage occurring at the emitting facets, while the latter refers to their progressive degradation due to some form of photochemical reaction [2]. The commonly accepted optical intensity at the facets for the point where catastrophic degradation occurs is about 1 MW/cm^2 for pulse lengths more than 1μs. For pulses shorter than 1μs, catastrophic failure intensity is approximately

inversely proportional to the square root of the pulse length. In many solid-state laser pumping applications, however, such short pulse behaviour is not of great interest. The catastrophic failure optical intensity for quasi-cw operation (pulse length of 150 μs -- 200 μs) is thus the same as that for cw operation.

The formation of nonradiative recombination centres in the active region causes the internal laser damage, which is usually a gradual process. This degradation rate increases with temperature and current density. It is preferable to operate diode lasers at low temperature with good heat dissipation to lengthen the laser lifetime as well as to maintain the original optical beam properties.

With advances in the semiconductor growth technologies employed in the production of the III/V compounds, such as liquid phase epitaxy (LPE), chemical vapour deposition (CVD) and molecular beam epitaxy (MBE), the maximum optical power density of diode lasers has been shown now to be only limited by the intrinsic catastrophic degradation at facets which is of the order of some MW/cm^2 for GaAlAs material [3]. So in terms of the total peak output power, a "broad-area" diode laser is more favourable to a narrow "stripe" diode laser. The mean power or cw power capability is, however, determined by heat dissipation, and thus depends on the dimensions of the laser and the efficiency of the heat sink.

Instead of making a single "broad-area" diode laser, the formation of linear array diode laser integrating tens, hundreds or even thousands of narrow stripe diode lasers in one device has been shown to be very successful. The one we used in our experiment was a ten-stripe SDL-2400 series laser with partially coherent phase-coupling. Such diode laser

arrays are identical to the "broad-area" ones of similar aperture, but with versatility for scaling up to much high power devices when more laser stripes are incorporated. Fig. 2.2.1 shows the cw optical power versus current (L–I) characteristic of our SDL-2430-H1 diode laser. The linearity of the L-I curve above the threshold current provides an easy means for linear modulation required in some applications.

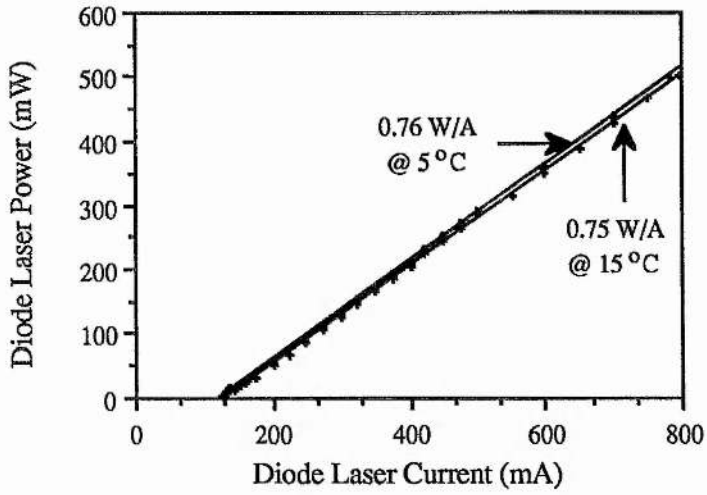

Figure 2.2.1 The laser output power from a SDL-2430-H1 diode laser as a function of current and heat sink temperature

Fig. 2.2.1 also indicates the operating temperature dependence of the output power. In fact, all diode lasers perform better at low temperature. The low working temperature not only gives longer lifetime, but also provides lower threshold and higher efficiency as shown in Fig. 2.2.1.

The temperature dependence of the threshold current is due to two major factors: first, an increased carrier population is needed to maintain the required population inversion in the bands with increased temperature; and second, more carriers leak out from the active regions in

heterojunction structures when the temperature is raised. There are also some other parameters that are dependent on temperature, such as internal absorption and internal quantum efficiency. Despite the complexity of all these parameters, a simple exponential relationship has been found useful to describe the threshold current dependence on temperature [4], that is

$$I_{th}(T_2) = I_{th}(T_1) \exp(\frac{T_2 - T_1}{\theta}) \quad , \qquad (2.2.1)$$

where $I_{th}(T_1)$ is the threshold current at the reference temperature (T_1), and θ is a characteristic parameter of the diode laser (it usually takes a larger value for more heavily doped material).

Further integration of stripe diode lasers leads to two-dimensional stacked diode laser arrays. Spectra Diode Labs is now selling the SDL-3230-Z series quasi-cw diode laser arrays, which can provide up to 1.5 kW peak power and 300 mJ per pulse. This power is achieved at up to 4% duty factor by stacking 25 linear arrays in 1 cm^2. Much higher duty cycle or cw versions have also been reported [5]. A 14-bar stack array can provide an average power of 300 W with a 20 % duty cycle, or a true cw power of 100 W. The achievement of the order of 1.5 kW/cm^2 optical density has been largely due to the newly developed integral liquid cooling systems (silicon micro-channel coolers) which are integrated directly into diode laser silicon substrate, so making the cooling efficiency of such systems very high.

2.3 Efficiencies

Since high electrical-to-optical efficiency has always been a major plus for diode lasers, it is appropriate to discuss some aspects of diode laser efficiency here. Different efficiencies are defined to describe particular combinations of loss mechanisms. The most common and useful definition for a final application user is the overall electrical-to-optical conversion efficiency, which, of course, is closely related to all other efficiencies, such as carrier injection efficiency, the radiative efficiency, and the external quantum efficiencies. Improvement of each of these efficiencies by proper material processing and structure design will increase the overall efficiency, namely the electrical-to-optical conversion efficiency.

The carrier injection efficiency is defined as the percentage of the injected carrier current in the total current, which can be expressed as

$$\eta_j = \frac{I_n}{I_n + I_p + I_c} \quad , \tag{2.3.1}$$

where I_n and I_p are the electron and hole diffusion currents in the neutral p and n regions respectively after injection, and I_c is the recombination current outside the depletion region due to the presence of some impurities. I_c is usually very small for good materials with careful processing. Also, I_p is usually small compared to I_n in direct bandgap semiconductors as a result of the large mobility ratio. For example, in GaAs, the mobility ratio μ_n/μ_p is about 30 [6]. So with proper material selection and careful processing, the value η_j can be very close to unity.

However, not all these injected carriers can produce photons. Some may

recombine nonradiatively. To describe this, another intermediate efficiency called the radiative efficiency is introduced. The radiative efficiency is defined as

$$\eta_r = \frac{1}{1 + \tau_r / \tau_{nr}} \quad , \tag{2.3.2}$$

where τ_r and τ_{nr} are the minority carrier lifetimes that participate in the radiative and nonradiative recombination process respectively. The internal quantum efficiency is defined by the product of the carrier injection efficiency and the radiative efficiency, i.e.,

$$\eta_i = \eta_j \eta_r \quad . \tag{2.3.3}$$

The power emitted by stimulated emission, thus, can be simply expressed by

$$P_e = \frac{(I - I_{th}) \eta_i}{e} h\upsilon \quad , \tag{2.3.4}$$

where I_{th} is the threshold current; e is the electron charge; and $h\upsilon$ is the emitted photon energy with frequency of υ. However, not all photons emitted can be extracted due to scattering and reabsorption losses inside a laser resonator and limited coupling at the output surface. To describe this extraction efficiency, another efficiency called the external quantum efficiency (η_e) is introduced, which can be generally expressed by

$$\eta_e = \frac{\ln(1/R)}{\alpha L + \ln(1/R)} \quad , \tag{2.3.5}$$

where α is the effective internal loss coefficient; L is the length of the cavity;

and R is the effective facet reflectivity which is related to the two end-surface reflectivities R_1, R_2 by

$$R = \sqrt{R_1 R_2} \quad . \tag{2.3.6}$$

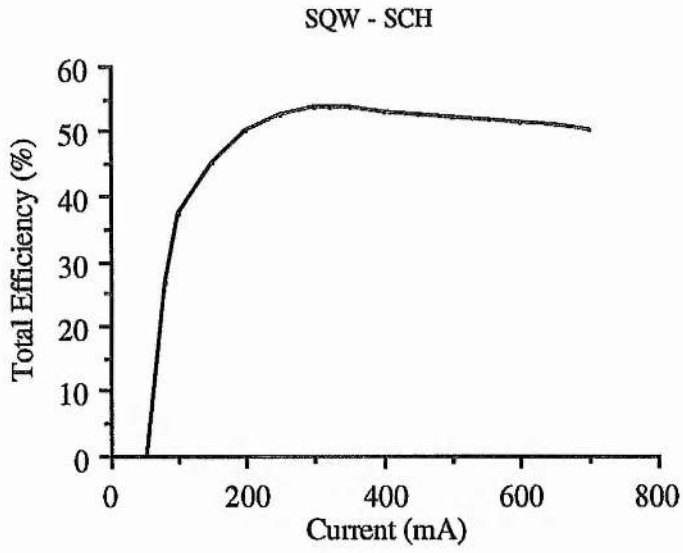

Figure 2.3.1 Efficiency-current curve of a 10-stripe, gain-guided 100 μm wide diode laser. SQW-SCH stands for single quantum well, separate confinement heterojunctions.

The total quantum efficiency is then the product of the internal and external quantum efficiencies, i.e.,

$$\eta_q = \eta_i \eta_e \quad . \tag{2.3.7}$$

In terms of power conversion efficiency, the electrical-to-optical conversion efficiency is then

$$\eta = \frac{P_e \eta_e}{V I} = \frac{(I - I_{th}) h\upsilon \eta_i \eta_e}{e V I} \quad . \tag{2.3.8}$$

where V is the applied voltage, and I is the diode laser current. Since the applied electric power, VI, involves not only the linear part $\eta_i E_g I$ (E_g is the bandgap voltage in the active layer) which contributes to the radiative recombination, but also the quadratic part due to the ohmic losses in the laser crystal. Fig. 2.3.1 shows the typical efficiency-current curve [1]. The declining plateau at the top of the curve illustrates that the ohmic losses gradually dominate the total input electrical power with increase in current.

2.4 Emitting Wavelengths

Semiconductor lasers of various types collectively can span the spectral region from 330 nm to beyond 15 μm, as shown in Fig. 2.4.1. Zinc and cadmium sulphides and selenides are used to span the uv and visible spectral region; diodes based on Ga, Al, As, P and Sb span the region from 630 to 1700 nm; indium based diodes cover the region from 0.9 to 5 μm; and diodes of the type $PbS_{1-x}Se_x$, $Cd_{1-x}Hg_xTe$, and PbSnTe work out into the middle-infrared spectral region (5 to 20 μm).

However, the most successful semiconductor lasers up to now have been those made of III-V semiconductor compounds, such as GaAlAs on GaAs substrate emitting in the range of 680-900 nm, (InGaAl)P on GaAs in 630-680 nm and InGaAsP on InP in 1100-1600 nm. Applications have been explored within each of these three successful diode laser bands. In the visible red region, the potential commercial market presently predominated by HeNe lasers (several hundred thousands each year) is the main stimulation for the development of red-emitting diode lasers. Another attraction of visible diode lasers is that they may replace present infrared

diode lasers in the printing field, since the recording paper is more sensitive at shorter wavelengths, which will then increase the writing speed. However, the power of visible diode lasers is still of the order of several mW at the moment, while infrared diode lasers have been enjoying their hundred mW levels. As writing speed is also power dependent, the advantages and disadvantages of infrared and visible diode lasers are matched.

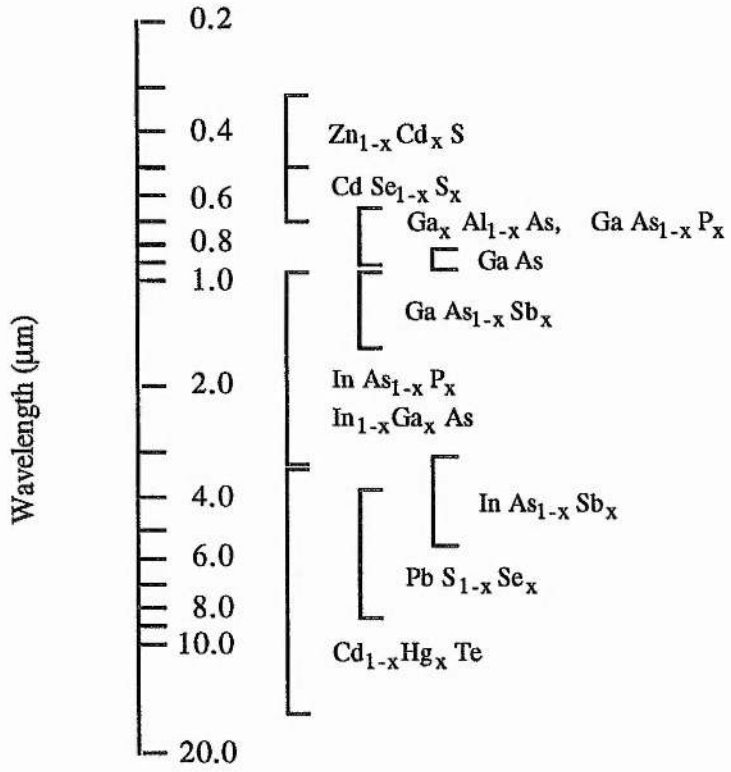

Figure 2.4.1 Spectral ranges of various types of semiconductor lasers

The interests in the 1.55-μm diode laser largely lie in the optical communication field. The earliest availability of AlGaAs/GaAs light-emitting diodes (LEDs) and diode lasers resulted in the first-generation commercial optical fibre system running in the range from 0.8 to 0.9 μm. Nowadays, most systems use wavelengths around 1.3 μm to take advantage of the lower fibre loss and zero dispersion at these

wavelengths, and such optical communication systems are regarded as second-generation systems. LEDs are commonly used in second-generation systems, as such systems operate in a wavelength region of minimum dispersion and give relaxed spectral requirements on light sources. Further improvement in the purity of silica fibre has shown that losses as low as 0.14 dB/km at a wavelength of 1.55 μm can be achieved. So to take full advantage of the ultra-low fibre losses, the trend in optical fibre communication systems is to use longer wavelengths around 1.55 μm, which are called third-generation systems.

Most present-day diode laser pumped solid-state lasers have been built with GaAlAs/GaAs lasers as pump sources (see chapter 1). The stringent requirement of spectral match between the pump light and the sharp absorption lines of solid-state materials demands that the diode laser wavelength control be considered from the very beginning of the material processing stages involved in fabrication of the diode laser. The correct choice of semiconductor laser material is of course a prerequisite. By varying the composition of a semiconductor compound it is possible to adjust the band gap of the material concerned. In the case of the $Ga_{1-x}Al_xAs$ semiconductor compound, the dependence of the band-gap energy on the Al mole fraction x can be approximated for $x<0.42$ by [7]

$$Eg = (1.424 + 1.266\,x) \quad eV \quad , \qquad (2.4.1)$$

so an increase in Al fraction results in a decrease in the emitting wavelength.

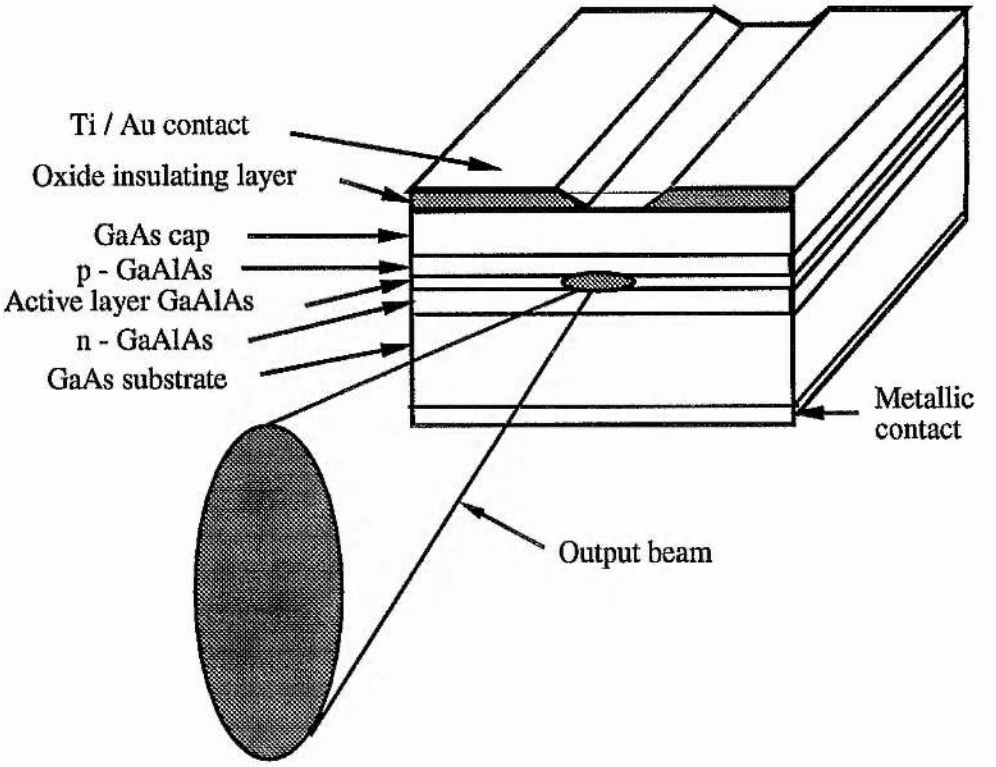

Figure 2.4.2 A typical double heterostructure. $Ga_{1-x}Al_xAs$ - $Ga_{1-y}Al_yAs$ diode laser, where x<y.

An inverse relation between band-gap and refractive index has been found to exist with very few exceptions over almost the whole range of III/V semiconductor compounds. For $Ga_{1-x}Al_xAs$, the refractive index change and the Al fraction x is related by

$$\Delta n \approx - 0.62\, x \quad . \qquad (2.4.2)$$

Such an inverse relation has been successfully made use of in double-heterojunction and multiple layer separate confinement heterostructure lasers. Fig. 2.4.2 shows a typical double-heterostructure gain guided device. The difference in Al content between the active and passive (or cladding) layers provides both the confinement for injected carriers and the confinement for light. Some devices with four or five layers

have also been demonstrated, these providing separate confinements for the injected carriers and light. Since the inner junctions or heterojunctions are used for carrier confinement and the outer heterojunctions are used for optical confinement in these devices, they can achieve simultaneously very low threshold currents and high output powers.

The use of a quantum well active layer structure is another way to achieve wavelength adjustment. When the active layer thickness of the previously described double heterostructure laser is reduced below 0.02 μm, the energy levels show obvious quantum confinement characteristics, and the photon energy of the radiative emission can now be written as

$$h\upsilon \approx E_g + E_{1c} + E_{1hh} = E_g + \left(\frac{h^2}{8L^2}\right)\left(\frac{1}{m_e^*} + \frac{1}{m_{hh}^*}\right) \quad , \qquad (2.4.3)$$

where E_g is the band-gap energy; E_{1c} is the lowest (1st) discrete energy level of electrons in conduction band; E_{1hh} is the highest (1st) discrete energy level of heavy holes in valence band; L is the well width; m_e^* is the effective electron mass; and m_{hh}^* is the effective heavy hole mass. Eq. (2.4.3) shows that the energy of the emitted photon may be varied by varying the well width L. In practice, quantum well structures have enabled the short end of the emission wavelength to be further extended.

In the opposite direction, strained-layer quantum structures can become a way of pushing up the long wavelength end of a material. Strained-layer heterostructures allow the use of lattice-mismatched materials without the generation of misfit dislocations. Such devices has been demonstrated with $In_xGa_{1-x}As$ - GaAs. By adjusting the indium fraction x, and hence the strain in the active layer, these $In_xGa_{1-x}As$ - GaAs strained-layer lasers

can be made to cover the wavelength range from 0.9 μm to 1.1 μm [8]. This freedom from the need for precise lattice matching greatly widens the choice of compatible materials.

The above coarse wavelength selection methods are implemented during manufacture of the diode laser. In addition, fine wavelength tuning must normally be employed during the application of a particular device. One of them is temperature tuning. It has been demonstrated that the emission wavelength generally increases with increasing temperature. Two major contributions to this wavelength increase are thermal expansion and phonon interactions. Thermal expansion reduces the band-gap energy significantly, at the same time enhanced phonon interactions broaden the electron and hole distributions. The combined effect of increased temperature is a much reduced band-gap energy . The wavelength tuning rate for GaAlAs diode lasers is typically 0.3 to 0.4 nanometers per degree centigrade. Fig. 2.4.3 shows the emitted wavelength of our 500-mW SDL-2430-H1 diode laser as a function of working temperature.

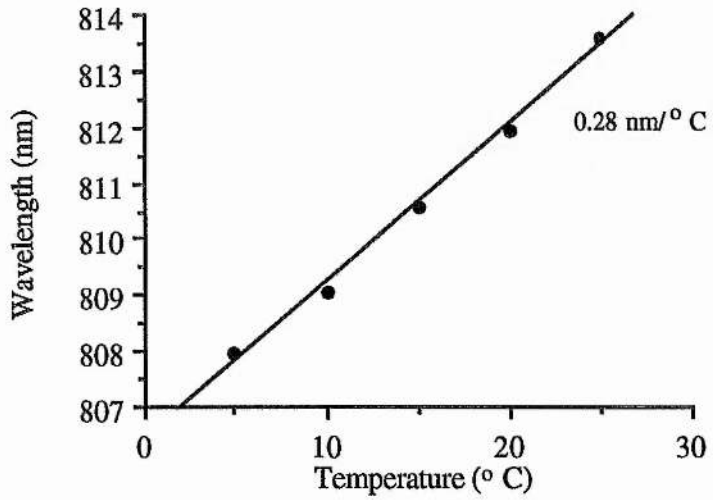

Figure 2.4.3 Temperature tuning curve of the SDL-2430-H1 diode laser

Temperature tuning has been very useful in obtaining optimum wavelength matching between pump light and absorption peaks of solid-state materials, especially those of rare-earth ion doped crystals, as they usually exhibit rather narrow absorption bands. Temperature control of a diode laser is usually achieved by using a small thermoelectric cooler unit, a thermocouple sensor and a feedback circuit - see Fig. 2.4.4 for the detailed structure of a SDL-2430 diode laser mount.

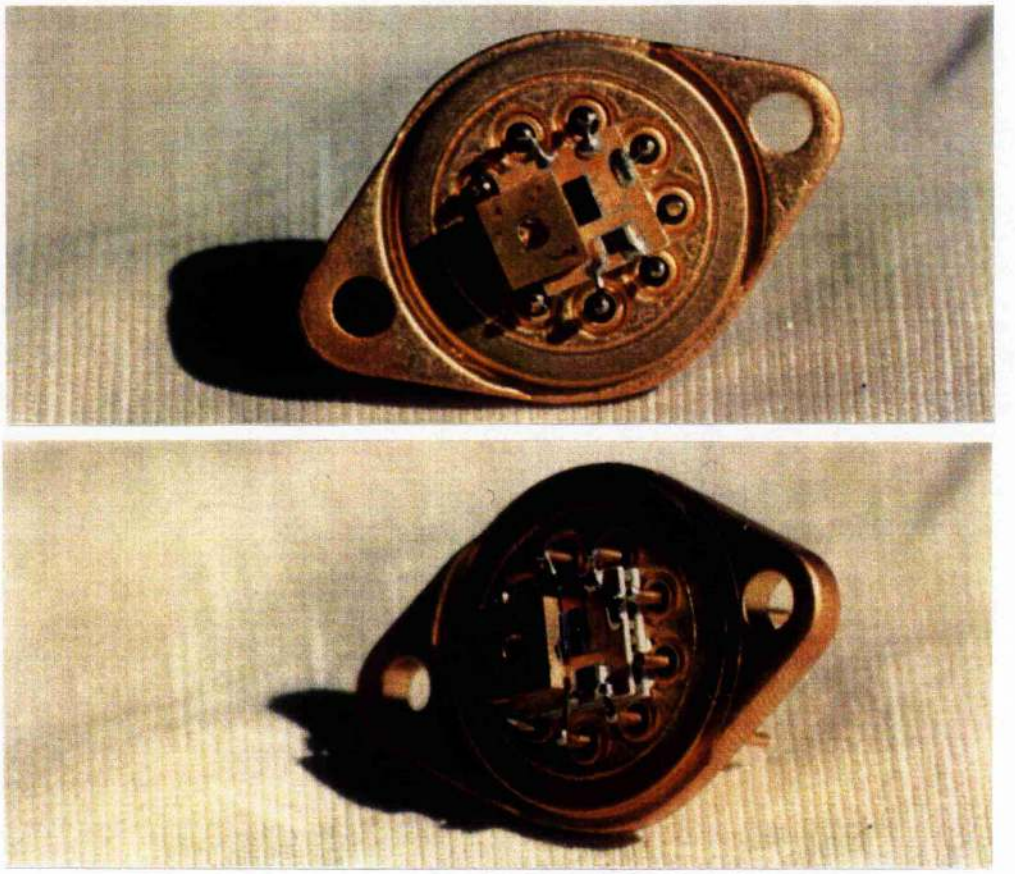

Figure 2.4.4 Photographs of a SDL-2430 diode laser mount

Another wavelength tuning technique commonly employed is the adjustment of the diode driving current. Though there are a few complex issues associated with the current change, the most relevant ones can be summarised as follows: change of dielectric constant, which includes both the imaginary and the real part of the dielectric constant, and change of quasi-Fermi levels due to the temperature change as discussed above.

Increasing gain in the active layer produces a corresponding increase in the imaginary part of the dielectric constant, while local heating related to the current distribution and power dissipation increases the real part of the dielectric constant. Though the exact current tuning characteristics differ from one device to another, the combined result, in general, is that the wavelength increases with increased current. For GaAlAs diode lasers, the change rate is typically 0.025 nm/mA. This wavelength and current relationship may be found useful in some applications such as direct electronic wavelength control. However it can also result in problems such as frequency chirping in pulsed diode lasers, which can lead to poor wavelength matching in the case of pulsed diode laser pumping. Fig. 2.4.5 shows the wavelength/ current relation of a 500-mW SDL-2430 diode laser.

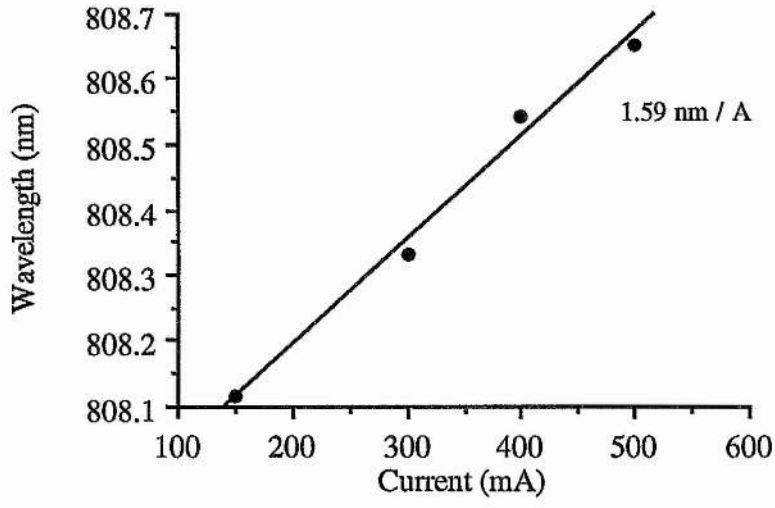

Figure 2.4.5 Current tuning of the SDL-2430-H1 diode laser

2.5 Output Beam Properties

There are some important properties typically associated with diode laser output beams. Some of these properties can be quite disadvantageous in certain applications. The qualities of diode laser output beams, generally speaking, are less satisfactory than most other lasers, both geometrically and spectrally. Every diode laser has its own output beam characteristics related to its waveguide structure.

In the plane perpendicular to the p-n junction, or the active layer, an effective dielectric slab waveguide geometry can be found for nearly every heterostructure diode laser. Such a waveguide is formed by the layers of the heterostructure with their different refractive indices. With properly chosen parameters, such waveguides can be used to confine the light entirely within the central layer, as well as to control transverse modes in the perpendicular plane. The simple waveguide treatment, based on the "zig-zag" ray model, applied to the perpendicular plane tells us that the angle of propagation, θ, defined as the angle between the zig-zag ray and the propagation axis, is [9]

$$\sin\theta = \frac{[\, m + (\phi_2 + \phi_3)/2\pi \,]\lambda_0}{2n_1 d}, \qquad (2.5.1)$$

where m is an integer (including zero), ϕ_2 and ϕ_3 are the phase advances at the two side interfaces respectively; n_1 is the refractive index of the centre layer; λ_0 is the free space laser wavelength; and d is the thickness of the centre layer. However, not every mode with transverse mode number m derived from Eq. (2.5.1) can propagate along the guide. The number of propagation modes is restricted by a parameter, called the critical angle θ_c,

which is determined by the total internal reflection condition. In the case of a symmetrical waveguide, i.e., the refractive indices on each side of the centre layer are equal ($n_2 = n_3 = n_{out}$), the critical angle is given by

$$\theta_c = \cos^{-1}\left(\frac{n_{out}}{n_1}\right) \quad . \qquad (2.5.2)$$

At a $Ga_{1-x}Al_xAs/Ga_{1-y}Al_yAs$ heterojunction with a typical AlAs composition step of 25 % the θ_c is about 15 °. When n_2 does not equal to n_3, the higher one of these two refractive indices should take the place of n_{out} in Eq. (2,.5.2).

The limitation set by θ_c on the propagation angle means that only those modes with values of m small enough for θ (from Eq. (2.5.1) to be less than the critical angle θ_c can be guided. As d is narrowed the higher order modes (m>1) successively cease to propagate or, as it is described, are "cut-off". The zero-order mode also ceases to propagate for d smaller than a certain value; except in the case where the guide is symmetrical so that both the phase advances ϕ_2 and ϕ_3 tend to zero at cut-off, i.e., $\phi_2 = \phi_3 = 0$, allowing the existence of zero order mode even for infinitesimally small d.

The thickness of the central layer of a typical double heterostructure waveguide is of the order of one-quarter of a free space wavelength. Though the light which it guides is confined to a width which is somewhat broader, it is normally not more than twice the thickness of the centre layer for a conventional double heterostructure waveguide. When light which has been confined to such dimensions radiates into free space natural diffraction causes the beam to spread into a total angle of about 45 ° (FWHM) in the plane perpendicular to the heterojunctions. Increasing the thickness

of the central layer does not necessarily reduce the beam divergence, since, as we discussed above, it can easily result in the generation of higher order transverse modes, thus producing widely divergent far-field patterns.

Similar considerations about the injected carrier confinement and optical confinement can also be applied to the junction plane. Diode lasers with such "lateral confinement" of both carriers and light are generally referred to as "stripe lasers". There have been various types of stripe lasers, but generally they can be classified as gain-guided or index-guided depending on whether it is the lateral variation of the optical gain or the refractive index that confines the mode. Index-guided lasers can further be subclassified as weakly or strongly index guided depending on the magnitude of the lateral index step. Fig. 2.5.1 shows schematically the three types of devices.

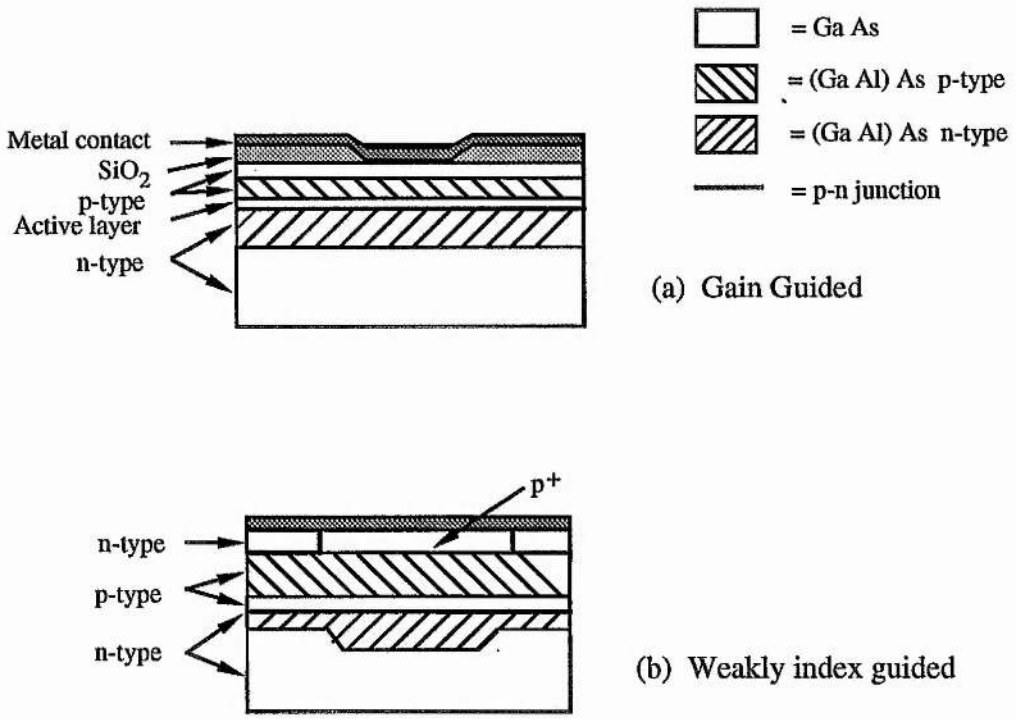

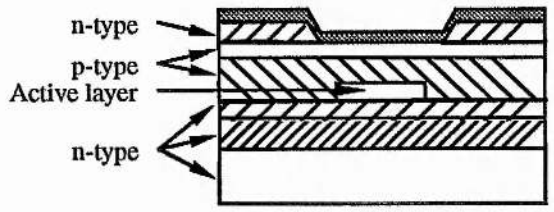

(c) Strongly index guided

Figure 2.5.1 Three types of lateral confinement shown schematically

In the case of strongly index guided lasers, the active region is buried in higher band-gap layers on all sides. For this reason, these lasers are often called buried-heterostructure lasers. The lateral index step along the junction plane plays the same role as the index step in the perpendicular plane, thus forming a rectangular waveguide that confines the lasing mode inside the buried active region. In addition to the light confinement, the potential barriers on all sides of the active region also help to confine the injected carriers, which results in a laser with very low threshold current. Strong index guided lasers have been proved to be able to give the most satisfactory performances, which include low threshold current, stable fundamental-mode operation at high powers, and good high-speed modulation characteristics.

In weakly index guided lasers, the active region is continuous and the effective index discontinuity is provided by a cladding layer of varying thickness. Depending on the specific design, these structures are known under various names, such as rib waveguide, ridge waveguide, plano-convex waveguide, and channeled-substrate planar waveguide [9,10]. Weakly index guided lasers are easier to fabricate than strongly index guided lasers, but generally they have higher threshold currents.

Further relaxation in the control of lateral confinement can be realised in so-called gain-guided lasers. Most injection lasers intended for

commercial applications have a built-in feature that restricts current injection to a small region along the junction plane. This restriction also serves the purpose of allowing fundamental-mode operation along the junction plane. The mechanism of gain-guiding is, however, rather different from that of index-guiding. The fundamental lateral mode is stabilized by introducing gain into the central region and loss into the wings of the mode so that higher order modes, which distribute more power to the wings, have higher thresholds.

The injected carriers reduce the refractive index, which may cause an anti-guiding effect. There are two physical mechanisms associated with this refractive index reduction phenomenon. One is the direct interaction between free-carriers and the optical wave, the so-called plasma effect, the magnitude of which is proportional to the concentration of injected carriers. The second one is the band-to-band interaction with the injected carriers which accompanies the gain process. As a first approximation the gain and the refractive index can be taken as varying linearly with each other in regions where the injected carrier concentration varies, [9] i.e.,

$$\Delta n = b\, i \quad , \tag{2.5.3}$$

where Δn is the refractive index change; i is the injected carrier density; and b is a negative parameter usually determined experimentally [10]. When the loss due to the anti-guiding effect introduced by Eq. (2.5.3) is compensated by sufficient gain along the axis, another interesting effect due to Eq. (2.5.3) will show. The refractive index profile with its lowest value in the centre gives the characteristic feature of gain guiding, that is the curved phase front, in contrast to index guiding that leads to a planar phase front.

With stripe width up to between 3 and 5 μm, fundamental lateral mode operation can be realised in GaAlAs/GaAs diode lasers, even at high powers. Because of the curved phase front, the fundamental mode beam diverges in the far field to a greater extent than would be the case if the wavefront in the laser were plane. To an external observer, the waist of the curved phase front beam appears to be originating from a virtual source in the junction plane within the laser, displaced some distance behind the emitting face. However, in the perpendicular plane the beam emerges with a plane wavefront from the heterostructure and the beam waist is coincident with the end-face of the laser. Hence, the overall beam is astigmatic and can not be perfectly focussed using any simple spherical lens systems. The astigmatism is commonly corrected by the use of a weak cylindrical lens.

Another significant feature of the output of a diode laser is its linear polarisation. In most cases, electric fields are found parallel to the diode laser junction, i.e., TE modes are the oscillating modes. The polarisation ratio (parallel component / perpendicular component) is generally greater than 100:1. However, this figure is smaller near lasing threshold where there is a significant intensity contribution from spontaneously emitted light. The origin of this difference between the TE and TM modes can be traced back to Maxwell's equations for a guided optical wave. The higher facet reflectivity for TE modes make the TE modes generally more favoured over the TM modes. Another minor factor that may further contribute in favour of the fundamental TE mode rather than the TM mode is the higher transverse confinement factor for the fundamental TE mode.

References

[1] W. Streifer, D. R. Scifres, G. L. Harnagel, D. F. Welch, J. Berger, and M. Sakamoto, "Advances in diode laser pumps", *IEEE J. Quantum Electron.*, Vol. QE-24, No. 6, (1988) 883;

[2] I. Ladany, M. Ettenberg, H. F. Lockwood and H. Kressel, "Al_2O_3 half-wave films for long life cw lasers", *Appl. Phys. Lett.*, Vol. 30, No. 2, (1977) 87;

[3] C. H. Henry, P. M. Petroff, R. A. Logan and F. R. Merritt, "Catastrophic damage of $Al_xGa_{1-x}As$ double-heterostructure laser material", *J. Appl. Phys.*, Vol. 50, No. 5, (1979) 3723;

[4] J. I. Pankove, "Temperature dependence of emission efficiency and lasing threshold in laser diodes", *IEEE J. Quantum Electron.*, Vol. QE-4, No. 4, (1968) 119;

[5] *Laser Focus World*, March (1991) 9;

[6] C. Yeh, *Handbook of Fiber Optics*, Academic Press, Inc., San Diego, (1990);

[7] A. Yariv, *Quantum Electronics* ; 3rd Ed., John Wiley and Sons, Singapore, (1988) 246;

[8] K. J. Beernink, P. K. York, J. J. Coleman, R. G. Waters, J. Kim and C. M. Wayman, "Characterization of InGaAs-GaAs strained-layer lasers with quantum wells near the critical thickness", *Appl. Phys. Lett.*, Vol. 55, No. 21, (1989) 2167;

[9] G. H. B. Thompson, *Physics of Semiconductor Laser Devices*, John Wiley and Sons, Chichester, (1980);

[10] G. P. Agrawal and N. K. Dutta, *Long-wavelength Semiconductor Lasers*, Van Nostrand Reinhold Company, New York, (1986).

Chapter 3

Modelling of Longitudinally Pumped 946-nm Nd:YAG Laser

3.1 Introduction

From chapter 1, we know there is one major difference between the 946-nm transition in Nd:YAG and the other common transitions such as those at 1.06 μm and 1.32 μm. These latter two have lower levels in the manifolds $^4I_{11/2}$ and $^4I_{13/2}$ respectively, which are so far above the ground state that the corresponding lower laser level thermal populations can always be neglected even at some elevated temperatures. The 946-nm transition, however, ends at the ground-state manifold, $^4I_{9/2}$, for which the energy level degeneracy is lifted by the crystal field splitting. As shown in the energy level diagram, Fig. 3.1.1, of Nd^{3+} in YAG, the lower laser level of the 946-nm transition is only about 4 kT above the ground level at room temperature. The lower laser level population in this case is then too significant to be neglected. The present laser system, with a thermal population in the lower laser level, lies between the two extremes usually considered in basic laser theories namely the three and four level schemes. Recently, a lot of interest has arisen in lasers with partially populated lower laser levels, and some systems have been explored both theoretically and experimentally [1-11]. These lasers have been given the names of quasi-three-level lasers [9] or quasi-four-level lasers [11], depending on which performance characteristic it is intended to emphasise.

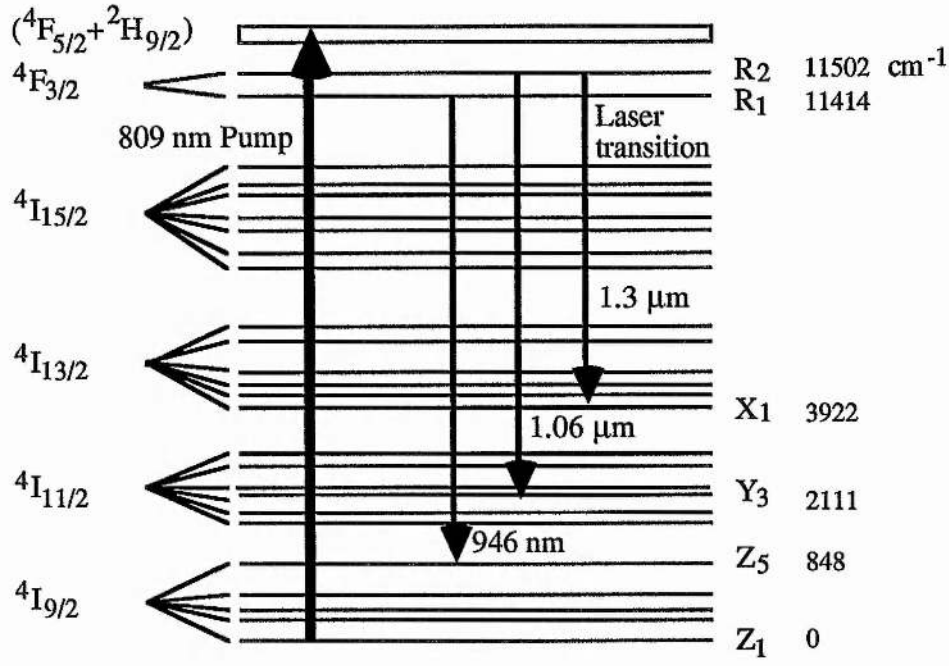

Figure 3.1.1 Energy-level diagram of neodymium ions in YAG crystal at T = 300°K

Quite a few solid-state lasers of current interest have been found to exhibit the temperature-dependent reabsorption losses due to the low lying lower laser levels. Examples include lasers operating on the $^5I_7$-$^5I_8$ transition (about 2.0-2.1 μm) of Ho^{3+} [6-8], the $^4I_{13/2}$-$^4I_{15/2}$ (about 1.5-1.7 μm) [12, 13] and $^4S_{3/2}$-$^4I_{15/2}$ (about 0.55 μm) [14] transitions of Er^{3+}, the $^3F_4$-$^3H_6$ (about 2.0 μm) transition of Tm^{3+} [15] and our main subject of this chapter, the $^4F_{3/2}$-$^4I_{9/2}$ transition of Nd^{3+} (about 0.9-0.95 μm) [1-5]. The general results derived for the 946-nm Nd:YAG laser in this chapter, however, can be applied to any of the transitions listed above.

Two major difficulties previously prevented the $^4F_{3/2}$-$^4I_{9/2}$ transition at 946 nm becoming one of the commonly used lines. One difficulty was the lower laser level thermal population as discussed above. Another difficulty was its relatively low gain [16, 17] leading to parasitic oscillation on the higher gain transition, $^4F_{3/2}$-$^4I_{11/2}$, especially when operating in a pulsed

mode. When employing conventional flashlamp pumped Nd:YAG laser systems, the straightforward solutions to these problems were to cool the crystal to reduce the lower state population and to use dichroic coatings and intracavity wavelength selective elements, such as prisms and wavelength selective transmission materials, to suppress parasitic oscillation [18-23].

The latest developments in laser diodes have made them ideal pump sources for Nd:YAG lasers [24, 25]. The perfect spectral match between the GaAlAs laser diode emission and the narrow absorption band of Nd^{3+} in YAG around 810 nm means that laser diode pumped Nd:YAG lasers have a very high efficiency, with consequently low heating of the YAG crystal and this means the 946-nm line can be made to lase even without forced cooling. The purpose of this chapter is to model the 946-nm Nd:YAG laser when longitudinally pumped by a spectrally clean light source, and to see how the performance is affected by relevant parameters, such as the working temperature , the Nd ion concentration, the pump light absorption coefficient, the laser light reabsorption cross section, and the other optimizable design parameters. We try to provide a general comprehensive understanding of the behaviour of longitudinally pumped solid-state lasers exhibiting reabsorption loss by comparing them occasionally with a well understood four-level counterpart, the 1.064 μm laser.

3.2 Quasi-Three-Level Laser

In a sense, nearly every laser system can be described as a quasi-three-level system, that is one where the lower laser level is more or less thermally populated. In most cases, however, the lower laser level lies so high above the ground state that its thermal population can be neglected,

thus the term four-laser-level laser is more often encountered.

In the state of thermal equilibrium , the Boltzmann distribution can be used to describe the relative populations of levels,i.e.,

$$f_j = \frac{g_j \exp(-h\upsilon_j/kT)}{\sum_i g_i \exp(-h\upsilon_i/kT)} \quad , \tag{3.2.1}$$

where k is the Boltzmann constant, T is the temperature, g_i and g_j are the degeneracy of states i and j, and $h\upsilon_i$ and $h\upsilon_j$ are the energies of states i and j. The sum is over all states. In Nd:YAG, each level has a degeneracy of 2, so the degeneracy factor actually cancels in Eq. (3.2.1).

In steady-state pumping, the whole system tends to have two sub-Boltzmann distributions due to the existence of the metastable manifold $^4F_{3/2}$ with a flourescence lifetime of 2.3×10^{-4} s [17, 26]. Experimental results have shown that the phonon spectrum of the YAG crystal lattice has many frequencies, the upper limit of which corresponds to a phonon energy of 850-860 cm^{-1} [27-29]. The energy-level diagram of Nd^{3+} in YAG (see Fig. 3.1.1) shows that the energy spacings between the Stark levels in the ground state manifold $^4I_{9/2}$ are less than or comparable to the upper limit of the phonon energy (850-860 cm^{-1}). So the transitions between them are basically nonradiative with lifetimes in the order of 10^{-8} s [27]. For an easy description, we adopt the nomenclature for energy manifolds/levels which is usually employed in the literature [30], ie., R, Y, and Z for the $^4F_{3/2}$, $^4I_{11/2}$, and $^4I_{9/2}$ manifolds respectively, and 1,2,3,.... for the Stark levels within a manifold, counting from the lowest level upwards. The energy of the upmost level, Z_5, in the $^4I_{9/2}$ manifold is so close to the highest phonon energy that resonance occurs [16], and thus the transition probability from

this level to the lowest level is extremely high with a transition time as short as 10^{-10}-10^{-12} s expected [27]. So we can always assume that the Z_5 will remain in thermal equilibrium with the lattice on the time scales involved in the present analysis, either cw or Q-switched. Similarly, the probabilities of nonradiative transitions both between the pump manifold and the upper laser manifold and within the upper laser manifold are also high, ($> 10^8\ s^{-1}$ [27, 29, 31], as the energy spacings are small compared with the phonon energy. In this case thermal equlibrium is established under cw conditions, but needs further closer consideration under conditions of Q-switching [see chapter 4].

In the distribution profile of the ^4I manifolds, the relative population of level Z_5, the lower laser level of the 946-nm line, is calculated to be 0.0079 at room temperature and 1.85×10^{-5} for Y_3, the lower laser level of the 1.064-μm transition which is hence about 430 times less densely populated than Z_5. So the temperature of the Nd:YAG crystal needs to drop down to about 120 K to keep the lower laser level population of the 946-nm line as low as that of the 1.064-μm line. Correspondingly, at room temperature, the upper laser level of the 946-nm transition, R_1, has a relative population which is 0.612 of the total population which builds up within the metastable manifold $^4F_{3/2}$.

From the discussion above, it can be seen that cooling of the Nd:YAG crystal is an effective way to encourage oscillation on the 946-nm laser line when under steady-state pumping. The cooling of the laser material not only reduces the lower laser level population but also increases the population of the upper laser level. The population inversion will then increase due to both effects; decreasing the threshold and increasing the efficiency.

3.3 Threshold

We start with the rate equations describing the population inversion and the photon density in the laser cavity in the steady-state case. From the discussion in the last section, the relative populations of the levels in both the upper and lower manifolds can be described by a Boltzmann distribution when the system is under steady-state pumping. If the total Nd ion concentration is denoted as N_o, the population density of the $^4F_{3/2}$ manifold as N_2 and the population density of the $^4I_{9/2}$ manifold as N_1, we have relations for the total population density

$$N_0=N_1+N_2 \quad , \tag{3.3.1}$$

the lower laser level population density,

$$N_a=f_a N_1 \quad , \tag{3.3.2}$$

and the upper laser level population density,

$$N_b=f_b N_2 \quad , \tag{3.3.3}$$

where f_a and f_b are the relative populations derived from the Boltzmann distribution, Eq. (3.2.1).

In the steady-state case, the upper laser manifold population at or below threshold is given by the rate equation

$$\frac{dN_2(r,z)}{dt} = -\frac{N_2(r,z)}{\tau} + R\, r_p(r,z) = 0 \quad , \tag{3.3.4}$$

where τ is the fluorescence lifetime of the upper laser manifold, R is the total pump rate and r_p is the normalised pump intensity spatial distribution, i.e.,

$$\iiint r_p(r,z)\, dV = 1 \quad ,$$

where V is the pump volume in the laser material. Combining Eq. (3.3.3) and Eq. (3.3.4), we get the upper laser level population,

$$N_b = f_b\, N_2 = f_b\, R\, r_p(r,z)\, \tau \quad . \tag{3.3.5}$$

It is obvious here that the upper laser level population has the same spatial distribution as the pump beam.

The optical gain can now be described by

$$G = \iiint 2\, L\, s_0(r,z)\, [\, N_b(r,z)\, \sigma_e - N_a(r,z)\, \sigma_a \,]\, dV \quad , \tag{3.3.6}$$

where L is the length of the solid-state laser medium, σ_e the stimulated emission cross section, σ_a is the absorption cross section, and $s_0(r,z)$ is the normalised cavity mode intensity distribution, which, in the case of the fundamental TEM_{00} mode, is expressed by a Gaussian distribution,

$$s_0(r,z) = \frac{2}{\pi\, \omega_0^2\, L} \exp\left(-\frac{2\, r^2}{\omega_0^2}\right) \quad , \tag{3.3.7}$$

where ω_0 is the Gaussian beam waist. At this stage in the analysis we have allowed for the absorption cross-section and stimulated emission cross-section being different in magnitude. Aull and Jenssen [16] have shown

that as a result of vibronic interaction in Nd:YAG there is a nonreciprocity in the absorption and emission cross-sections associated with, inter alia, the 946-nm transition. Their measurements indicate that the stimulated emission cross-section ($\sigma_e = 5.3 \times 10^{-20}$ cm^2) is some 25 % greater than the absorption cross-section ($\sigma_a = 4.0 \times 10^{-20}$ cm^2).

To determine the threshold condition, the round-trip gain (G) averaged over the cavity mode is put equal to the round-trip loss (δ), i.e.,

$$\iiint 2\,L\,s_0(r,z)\,[\,N_b(r,z)\,\sigma_e - N_a(r,z)\,\sigma_a\,]\,dV = \delta \quad . \tag{3.3.8}$$

Rearranging Eq. (3.3.8) and substituting from Eqs. (3.3.1), (3.3.2) and (3.3.5), we get

$$\iiint 2\,L\,s_0(r,z)\,r_p(r,z)\,R_{th}\,\tau\,(f_b\,\sigma_e + f_a\,\sigma_a)\,dV$$

$$= \delta + \iiint 2\,L\,s_0(r,z)\,f_a\,N_0\,\sigma_a\,dV \quad . \tag{3.3.9}$$

Here the threshold pump rate is denoted by R_{th} and is related to the absorbed threshold pump power by

$$P_{ab,th} = R_{th}\,h\upsilon_p/\eta \quad ,$$

where $h\upsilon_p$ is the pump photon energy, and η is the fraction of the pump photons deposited in the gain medium. Since

$$\iiint s_0(r,z)\,dV = 1 \quad ,$$

Eq. (3.3.9) becomes

$$R_{th} \iiint s_0(r,z)\, r_p(r,z)\, dV = \frac{\delta + 2\,L\, f_a\, N_0\, \sigma_a}{2\,L\,(f_b\,\sigma_e + f_a\,\sigma_a)\,\tau} \quad . \qquad (3.3.10)$$

Comparing this expression with that for a 4-level laser system, we can see that the thermal population of the lower laser level plays a double role here. It acts as an additional loss to the original total cavity loss and at the same time modifies the effective stimulated emission cross section. We can also see that the overlap integral between the cavity mode (s_0) and the pump beam (r_p) is reciprocal to the pump threshold, so a large overlap integral is required for a low threshold. To see the effects of different pumping geometries, while keeping the laser cavity mode distribution the same as described by Eq. (3.3.7), we will solve Eq. (3.3.10) for three typical pumping geometries, i.e, on-axis pumping, uniform pumping and Gaussian pumping.

In the case of on-axis pumping, the normalised pump intensity can be described by

$$r_p(x,y,z) = \frac{\alpha}{1 - \exp(-\alpha L)}\,\delta(x)\,\delta(y)\,\exp(-\alpha z) \quad , \qquad (3.3.11)$$

where α is the pump light absorption coefficient, and $\delta(x)$ and $\delta(y)$ are the Dirac delta functions. Substituting Eq. (3.3.11) into Eq. (3.3.10) and performing the integration, we obtain the threshold pump rate as

$$R_{th} = \frac{\pi\,\omega_0^2\,(\delta + 2\,L\,f_a\,N_0\,\sigma_a)}{4\,\tau\,(f_b\,\sigma_e + f_a\,\sigma_a)} \quad . \qquad (3.3.12)$$

In terms of the absorbed pump power at threshold, Eq. (3.3.12) becomes

$$P_{ab.th} = R_{th}\ h\upsilon_p\ /\eta = \frac{\pi\ \omega_0^2\ h\upsilon_p\ (\delta + 2\ L\ f_a\ N_0\ \sigma_a)}{4\ \tau\ \eta\ (f_b\ \sigma_e + f_a\ \sigma_a)} \quad , \qquad (3.3.13)$$

or, in terms of the total input optical pump power at threshold,

$$P_{th} = \frac{P_{ab.th}}{1\ -\ \exp(-\alpha L)}$$

$$= \frac{\pi\ \omega_0^2\ h\upsilon_p\ (\delta + 2\ L\ f_a\ N_0\ \sigma_a)}{4\ \tau\ \eta\ (f_b\ \sigma_e + f_a\ \sigma_a)\cdot[\ 1\ -\ \exp(-\alpha L)\ ]} \quad . \qquad (3.3.14)$$

Since the fractions f_a and f_b are temperature dependent values, Eq. (3.3.14) also describes how the pump threshold is related to the working temperature.

To find the the crystal length which gives the lowest threshold, we differentiate both sides of Eq. (3.3.14) and equate them to zero, when we get the minimum threshold condition

$$2\ f_a\ N_0\ \sigma_a = \frac{\alpha\ \exp(-\alpha L_{th})}{1-\ \exp(-\alpha L_{th})} \cdot (\delta + 2\ L_{th} f_a\ N_0\ \sigma_a) \quad . \qquad (3.3.15)$$

From Eq. (3.3.15) it is difficult to see explicitly the relation between the crystal length giving minimum threshold, L_{th}, and the round-trip loss. However, numerical solutions to Eq. (3.3.15) have been obtained and the results are displayed graphically. In Figs. 3.3.1 (a) and (b), the crystal length, L_{th}, and the associated minimum threshold pump power respectively are plotted as functions of cavity round-trip loss, with absorption coefficient, α as the parameter. In Fig. 3.3.1(c), the minimum threshold pump power is plotted as a function of the crystal length L_{th}.

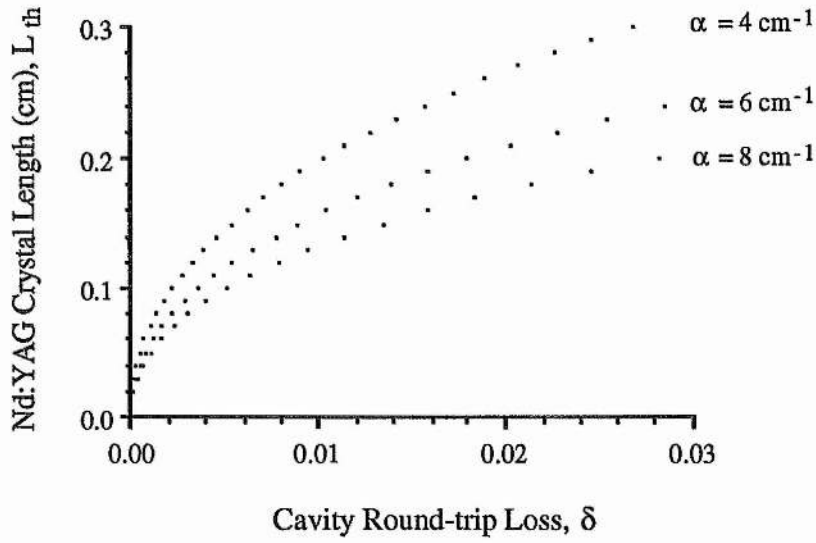
Nd:YAG Crystal Length (cm), L_{th}
0.3
0.2
0.1
0.0
0.00
0.01
0.02
0.03
$\alpha = 4\ cm^{-1}$
$\alpha = 6\ cm^{-1}$
$\alpha = 8\ cm^{-1}$
Cavity Round-trip Loss, δ

(a)

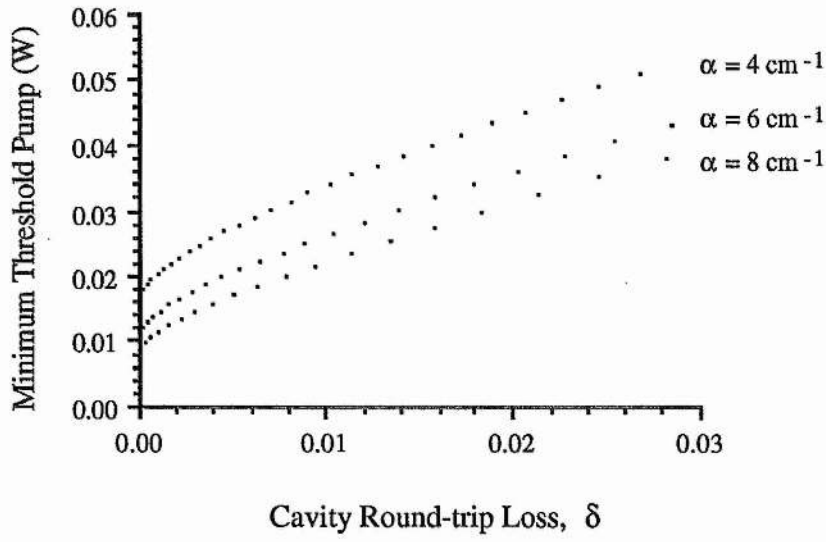
Minimum Threshold Pump (W)
0.06
0.05
0.04
0.03
0.02
0.01
0.00
0.00
0.01
0.02
0.03
$\alpha = 4\ cm^{-1}$
$\alpha = 6\ cm^{-1}$
$\alpha = 8\ cm^{-1}$
Cavity Round-trip Loss, δ

(b)

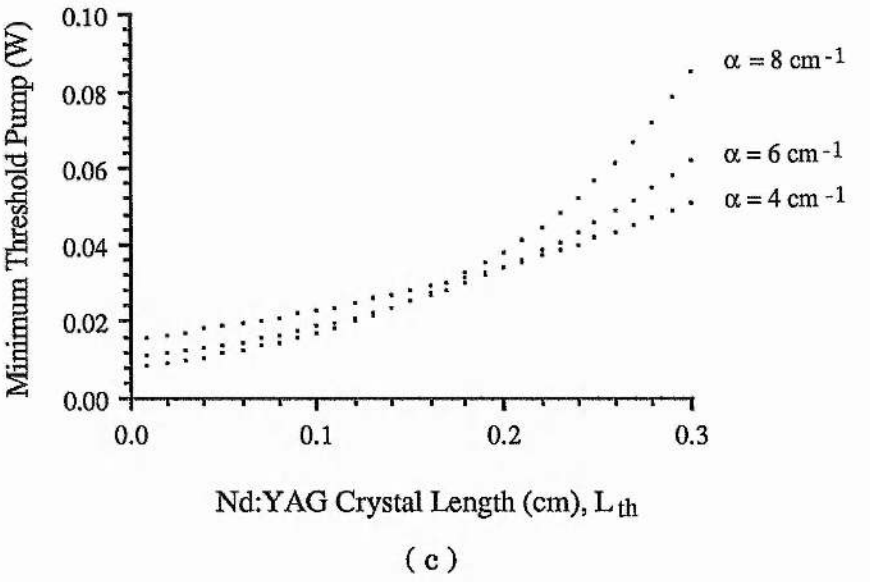

(c)

Figure 3.3.1 On-axis pumping case: (a) the crystal length L_{th} for minimum threshold as a function of cavity loss; (b) and (c) the minimum pump power at threshold as a function of cavity round-trip loss and the crystal length respectively, in (b) and (c) the cavity mode waist ω_0=50 μm.

The data used in Fig.3.3.1 are listed below for reference:

the fluorescent lifetime $\tau = 2.3\times10^{-4}$ sec. [26];

the upper laser level population fraction $f_b = 0.612$;

the lower laser level population fracton $f_a = 0.0079$;

the pump efficiency $\eta = 1$;

the photon energy at 808 nm $h\upsilon_p = 2.457\times10^{-19}$ J;

the Nd ion concentration for 1.1% atomic doped YAG

$N_0 = 1.518\times10^{20}$ cm^{-3};

the cavity mode waist $\omega_0 = 50$ μm;

the stimulated emission cross section $\sigma_e = 5.3\times10^{-20}$ cm^{-2} [16];

the absorption cross section $\sigma_a = 4.0\times10^{-20}$ cm^{-2} [16];

the effective stimulated cross section $f_b\sigma_e+f_a\sigma_a = 3.275\times10^{-20}$ cm^{-2}.

However, the crystal length which satisfies the condition for the minimum threshold is not necessarily the optimum length at higher pump powers, and we will discuss this more fully in the next section.

The second pumping geometry, which we are going to discuss, is the uniform pumping, i.e., a flat intensity distribution within the beam and zero intensity outside the beam. The normalised pump intensity of this uniform pumping geometry can be described as

$$r_p(r,z) = \frac{\alpha}{\pi \omega_p^2 [1 - \exp(-\alpha L)]} \theta(r - \omega_p) \exp(-\alpha z) \quad , \qquad (3.3.16)$$

where ω_p is the radius of pump beam, and $\theta(r-\omega_p)$ is the step function which equals unity for $r \leq \omega_p$, and zero for $r > \omega_p$. Repeating the same procedure as before, we get the input optical pump power at threshold as

$$P_{th} = \frac{2\,\omega_p^2/\omega_0^2}{1 - \exp(-2\omega_p^2/\omega_0^2)} P_{th.\ on\text{-}axis} \quad , \qquad (3.3.17)$$

where $P_{th.on\text{-}axis}$ is given by Eq. (3.3.14). When the pump beam waist approaches zero, Eq. (3.3.17) reduces to the on-axis pumping case as expected, i.e., $P_{th}=P_{th.on\text{-}axis}$. Fig. 3.3.2 shows, for the uniform pumping case, the effect of pump beam size on the pump threshold. In Fig. 3.3.2 , the crystal lengths in both cases are assumed to be the same, they, however, may not necessarily be the length for the minimum threshold.

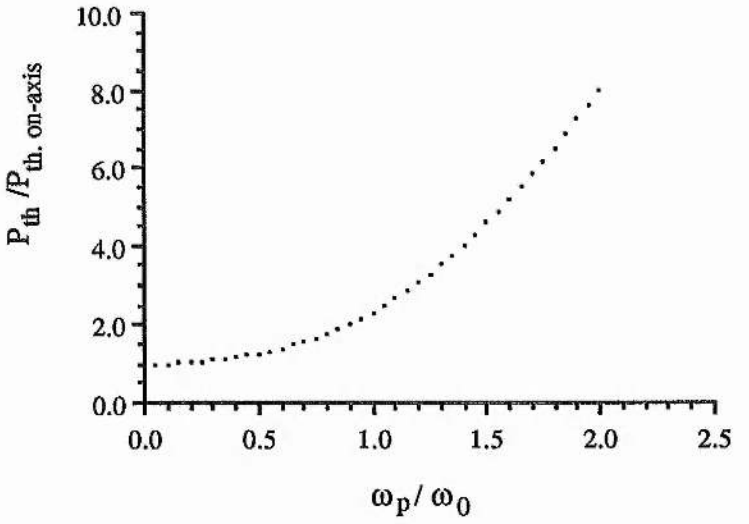

Figure 3.3.2 The input pump power at threshold for the case of uniform pumping as a function of the ratio of the pump beam radius to the cavity mode radius

The last pumping geometry which we intended to discuss is that of a pump beam with a Gaussian distribution, which gives the normalised pump intensity as

$$r_p(r,z) = \frac{2\,\alpha}{\pi\,\omega_p^2\,[1 - \exp(-\alpha L)]}\,\exp(-2r^2/\omega_p^2)\,\exp(-\alpha z)\ . \quad (3.3.18)$$

Substituting Eq. (3.3.18) into Eq. (3.3.10) and pursuing the same procedure as before, we obtain the input pump power at threshold in the form

$$P_{th} = (1 + \omega_p^2/\omega_0^2)\ P_{th.on\text{-}axis}\ , \quad (3.3.19)$$

which also reduces to the special case of on-axis pumping, when ω_p approaches zero. Fig. 3.3.3 shows the relation between the input pump power at threshold and the relative pump beam size (ω_p/ω_0).

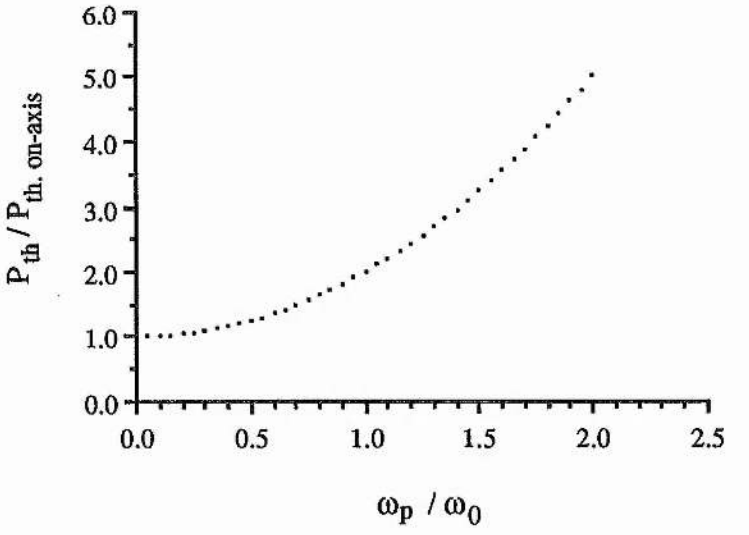

Figure 3.3.3 The Gaussian pumping threshold as a function of the relative pump beam size (ω_p/ω_0)

To conclude, we have shown that there exists a particular value of crystal length L_{th} for minimum threshold. However, it may not be the optimum length from the point of view of maximum output power at high pump powers, and this will be discussed further in the next section. Further, we have shown that no matter what pumping geometry is used, the on-axis pumping always gives the lowest pump power at threshold.

3.4 Laser Output Power

When the pump power is increased above the threshold pump power, the laser system will now start lasing. At this time, the populations of both upper laser level and lower laser level are directly coupled with the cavity photon number. For simplicity, in the analysis below we assume that the Nd:YAG medium fully fills the laser cavity, or, in other words, that the

laser cavity is formed by mirrors directly coated on the crystal ends. In the steady state, the rate equations for the populations of the upper and lower laser levels and the cavity photon number are thus

$$\frac{dN_b(r,z)}{dt} = f_b R\, r_p(r,z) - f_b \frac{N_2(r,z) - N_2^0}{\tau}$$

$$- \frac{f_b c\, \sigma\, [N_b(r,z) - N_a(r,z)]}{n} S\, s_0(r,z) = 0 \quad , \qquad (3.4.1a)$$

$$\frac{dN_a(r,z)}{dt} = - f_a R\, r_p(r,z) + f_a \frac{N_2(r,z) - N_2^0}{\tau}$$

$$+ \frac{f_a c\, \sigma\, [N_b(r,z) - N_a(r,z)]}{n} S\, s_0(r,z) = 0 \quad , \qquad (3.4.1b)$$

and

$$\frac{dS}{dt} = \frac{c\,\sigma}{n} \iiint [N_b(r,z) - N_a(r,z)]\, S\, s_0(r,z)\, dV - \frac{c\,\delta}{2\,n\,L} S$$

$$= 0 \quad , \qquad (3.4.1c)$$

where c is the speed of light; n is the refractive index of Nd:YAG at 946 nm; S is the total photon number in the cavity; N_1^0 and N_2^0 are the populations of the lower laser level manifold and upper laser level manifold respectively at thermal equilibrium; σ is the gain cross section corresponding to the 946-nm transition; and δ is the cavity loss including output coupling. We have assumed in Eqs. (3.4.1) above that the absorption and stimulated emission cross-sections are of equal magnitude and may be replaced by a single cross- section σ. This allows Eq. (3.4.1b) to be written in terms of the population inversion, which, as will be seen shortly, considerably simplifies

the subsequent analysis. However, the comments regarding the relative magnitudes of the absorption and emission cross-sections made following Eq. (3.3.6) still, of course, apply here.

Since $N_1+N_2=N_0$, Eq. (3.4.1b) can now be rewritten in the form of

$$\frac{dN_a(r,z)}{dt} = - f_a R\, r_p(r,z) - f_a \frac{N_1(r,z) - N_1^0}{\tau}$$

$$+ \frac{f_a c \sigma [N_b(r,z) - N_a(r,z)]}{n} S\, s_0(r,z) = 0 \quad , \qquad (3.4.1b')$$

This is now a convenient form for obtaining the population inversion from Eqs. (3.4.1), and this we now do. Substracting Eq. (3.4.1b') from Eq. (3.4.1a), we get

$$\frac{d\,\Delta N(r,z)}{dt} = (f_a + f_b)\, R\, r_p(r,z) - \frac{\Delta N(r,z) - \Delta N^0}{\tau}$$

$$- \frac{(f_a + f_b)\, c \sigma \Delta N(r,z)}{n} S\, s_0(r,z) = 0 \quad , \qquad (3.4.2)$$

where $\Delta N=N_b-N_a=f_bN_2-f_aN_1$, and ΔN^0 is the population inversion at thermal equilibrium in the absence of pumping. Expressed in terms of the population inversion ΔN, Eq. (3.4.1c) becomes

$$\frac{dS}{dt} = \frac{c \sigma}{n} \iiint \Delta N(r,z)\, S\, s_0(r,z)\, dV - \frac{c \delta}{2\, n L} S = 0 \quad . \qquad (3.4.3)$$

Solving Eq. (3.4.2) for ΔN and substituting into Eq. (3.4.3), we obtain

$$\frac{\delta}{2\sigma L} = (f_a + f_b)\, R\, \tau \iiint \frac{r_p(r,z)\, s_0(r,z)}{1 + \dfrac{(f_a + f_b)\, c\, \sigma\, \tau}{n} S\, s_0(r,z)}\, dV$$

$$+ \Delta N^0 \iiint \frac{s_0(r,z)}{1 + \dfrac{(f_a + f_b)\, c\, \sigma\, \tau}{n} S\, s_0(r,z)}\, dV \quad . \qquad (3.4.4)$$

When the laser system is below or at threshold, i.e., S=0, Eq. (3.4.4) should reduce to Eq. (3.3.10). For this to be the case, the effective gain cross section is seen to be

$$\sigma = \frac{f_b\, \sigma_e + f_a\, \sigma_a}{f_a + f_b} \quad . \qquad (3.4.5)$$

Since $f_b(=0.612) >> f_a(=0.0079)$, we have that $\sigma \approx \sigma_e$. A further point in relation to Eq. (3.4.4) is that ΔN^0, the population inversion at thermal equilibrium in the absence of pumping, is essentially $(-f_a N_0)$, the thermal equilibrium population of the lower laser level, since the thermal equilibrium population of the upper laser level is negligible. This was the approximation made in deriving Eq. (3.3.10) and hence in our threshold analysis.

Eq. (3.4.4) reduces to the four-level laser case when ΔN^0 approaches zero. For a quasi-three-level laser system, as described by Eq. (3.4.4), the second integral on the left-hand side of Eq. (3.4.4) describes departures from the four-level case. The integral is dependent on the cavity mode distribution with the cavity photon number S as parameter. We denote this integral as B. For the fundamental Gaussian mode defined by Eq. (3.3.7), the integral B can be solved analytically to be

$$B = \frac{\Delta N^0 S'}{2 S} \ln(1 + \frac{2 S}{S'}) \quad , \tag{3.4.6}$$

where S' is equivalent to a saturation photon number, which is defined as

$$S' = \frac{n \pi \omega_0^2 L}{(f_a + f_b) c \sigma \tau} \quad . \tag{3.4.7}$$

Since the equilibrium population inversion ΔN^0 is always a negative value in any circumstances, Eq. (3.4.6) is simply a loss term, which can be interpreted as a saturable loss.

The first integral in Eq. (3.4.4), which describes the coupling effect of the pump beam and the cavity mode, can also be solved analytically for some special pumping geometries while keeping the cavity mode as a fundamental Gaussian mode. We start with the on-axis pumping geometry, which has the normalized pump intensity described by Eq. (3.3.11). Substituting Eq. (3.3.11) into Eq. (3.4.4), and performing the integration, we have

$$\begin{aligned} \frac{\delta}{2 \sigma L} &= \frac{2 (f_a + f_b) R \tau}{\pi \omega_0^2 L (1 + 2 S/S')} + B \\ &= \frac{2 (f_a + f_b) R \tau}{\pi \omega_0^2 L (1 + 2 S/S')} + \frac{\Delta N^0 S'}{2 S} \ln(1 + 2S/S') \quad . \end{aligned} \tag{3.4.8}$$

In order to explicitly relate the laser output to the input pump power, we require the relation between the pump rate, R, and the pump power, P_{in}; and the relation between the cavity photon number, S, and the laser output power, P_{out}. They are

$$P_{in} = \frac{R\, h\upsilon_p/\eta}{1 - \exp(-\alpha L)} \quad , \tag{3.4.9}$$

and

$$P_{out} = \frac{S\, T\, c\, h\upsilon_L}{2\, l_{cav.}} \quad , \tag{3.4.10}$$

where $l_{cav.}$ is the optical length of the cavity, and $2\, l_{cav.}/c$ is the cavity round-trip time (for simplicity the cavity length has been assumed from the start to be the same as the Nd:YAG crystal length, i.e., $l_{cav.} = nL$); T is the output coupler transmission; and $h\upsilon_L$ is the laser photon energy.

When Eq. (3.4.8) is expressed in terms of P_{in} and P_{out} with the crystal length L and the output coupling T as optimizable parameters, we can numerically obtain the maximum output power and find the optimum values for the crystal length and the output coupler transmission for a given cavity mode waist. In the case of on-axis pumping, the calculated 946-nm laser output powers versus L and T are shown in Fig. 3.4.1 for ω_0=20 μm, ω_0=30 μm, ω_0=50 μm and ω_0=70 μm.

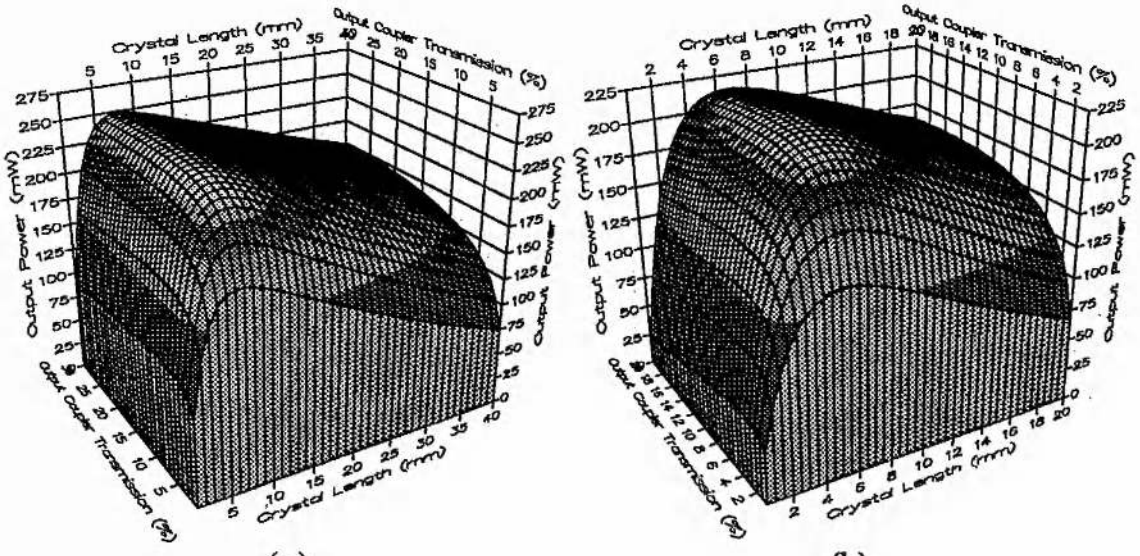

(a) (b)

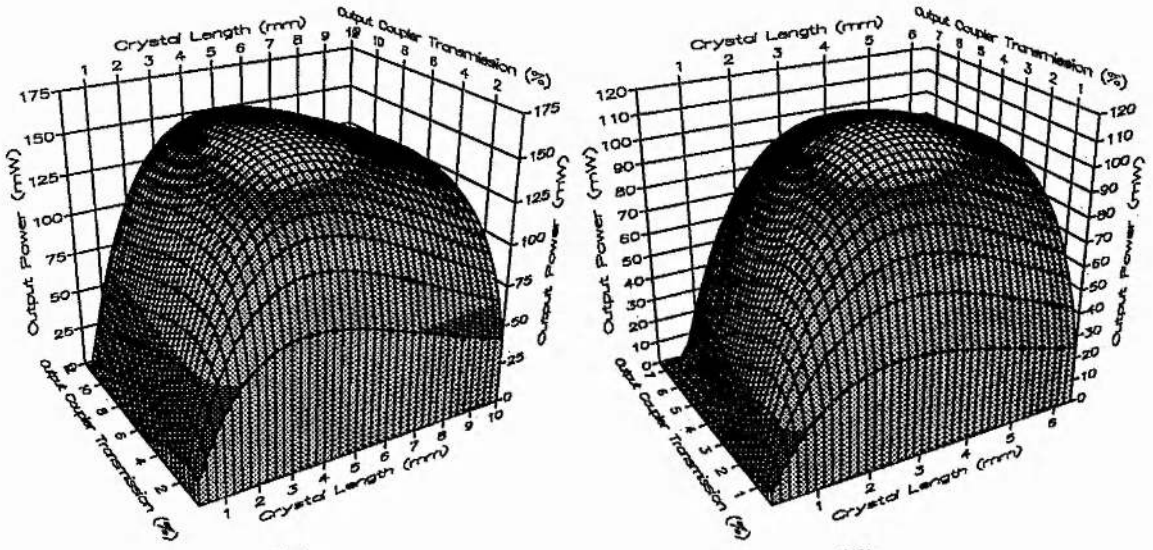

Figure 3.4.1 Calculated 946 nm laser output powers versus the crystal length, L, and the output coupler transmission, T, for the cases of on-axis pumping at pump power of 360 mW. a) ω_0=20 μm, b) ω_0=30 μm, c) ω_0=50 μm, and d) ω_0=70 μm.

To see the effects of pump beam size, we now consider some more general pumping geometries. In the case of uniform pumping with a beam radius of ω_p, Eq. (3.4.4) turns out to be

$$\frac{\delta}{2\sigma L} = \frac{(f_a + f_b)\, R\, \tau}{\pi \omega_p^2 L} \cdot \frac{S'}{2S} \ln\left[\frac{1 + \frac{2S}{S'}}{1 + \frac{2S}{S'} \exp(-2\omega_p^2/\omega_0^2)}\right]$$

$$+ \frac{\Delta N^0 S'}{2S} \ln(1 + 2S/S') \quad . \qquad (3.4.11)$$

In the case of single transverse mode laser pumping, where the pump beam has a fundamental Gaussian mode distribution, Eq. (3.4.4) then becomes

$$\frac{\delta}{2\,\sigma\,L} = \frac{2\,(f_a + f_b)\,R\,\tau}{\pi\,\omega_p^2\,L} \int_0^{\infty} \frac{\exp[-(1 + \omega_0^2/\omega_p^2)\,x]}{1 + \frac{2\,S}{S'}\exp(-x)}\,dx$$

$$+ \frac{\Delta N^0\,S'}{2\,S}\,\ln(1 + 2S/S') \quad , \qquad (3.4.12)$$

where x is defined as

$$x = 2\,r^2/\omega_0^2 \quad .$$

In Figs. 3.4.2 and 3.4.3, the output power has been plotted against the crystal length and the output coupler transmission for the case of uniform pumping and the case of Gaussian beam pumping respectively. From these figures, it is obvious that the optimum crystal length and output coupling are different in the two cases. In the case of longitudinally diode laser array pumped Nd:YAG lasers, the uniform pumping model is expected to be more appropriate. On the other hand, for Ti:sapphire laser or dye laser pumping, when the beam has a well-defined single transverse mode characteristic, the fundamental Gaussian mode pumping model is expected to be more suitable. The theoretical results from our model will be reviewed in chapter 5, where the experimental results are presented and discussed.

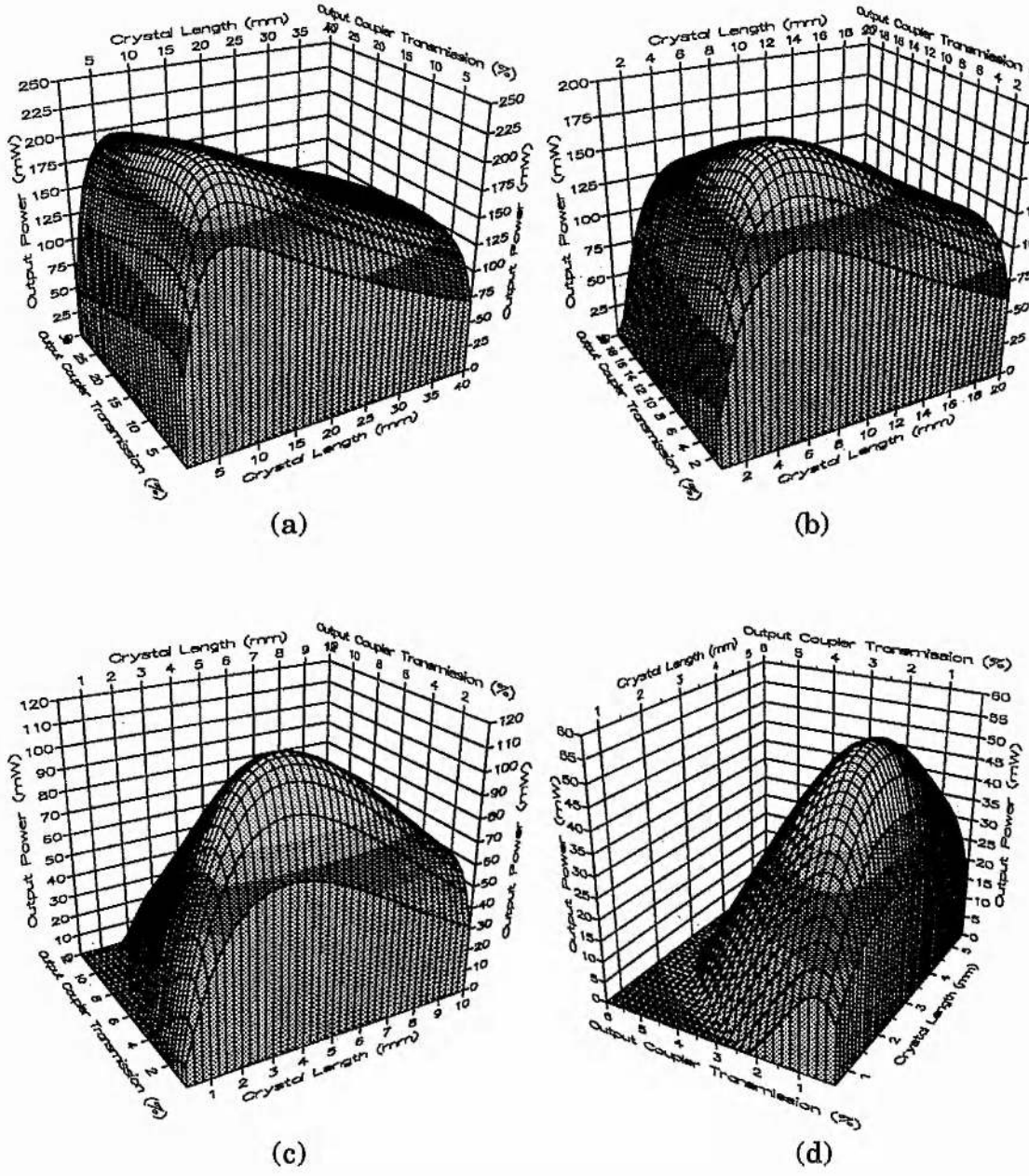

Figure 3.4.2 Calculated 946 nm laser output powers versus the crystal length, L, and the output coupler transmission, T, for the cases of uniform pumping at pump power of 360 mW. $\omega_p/\omega_0 = 1$ is assumed. a) ω_0=20 μm, b) ω_0=30 μm, c) ω_0=50 μm, and d) ω_0=70 μm.

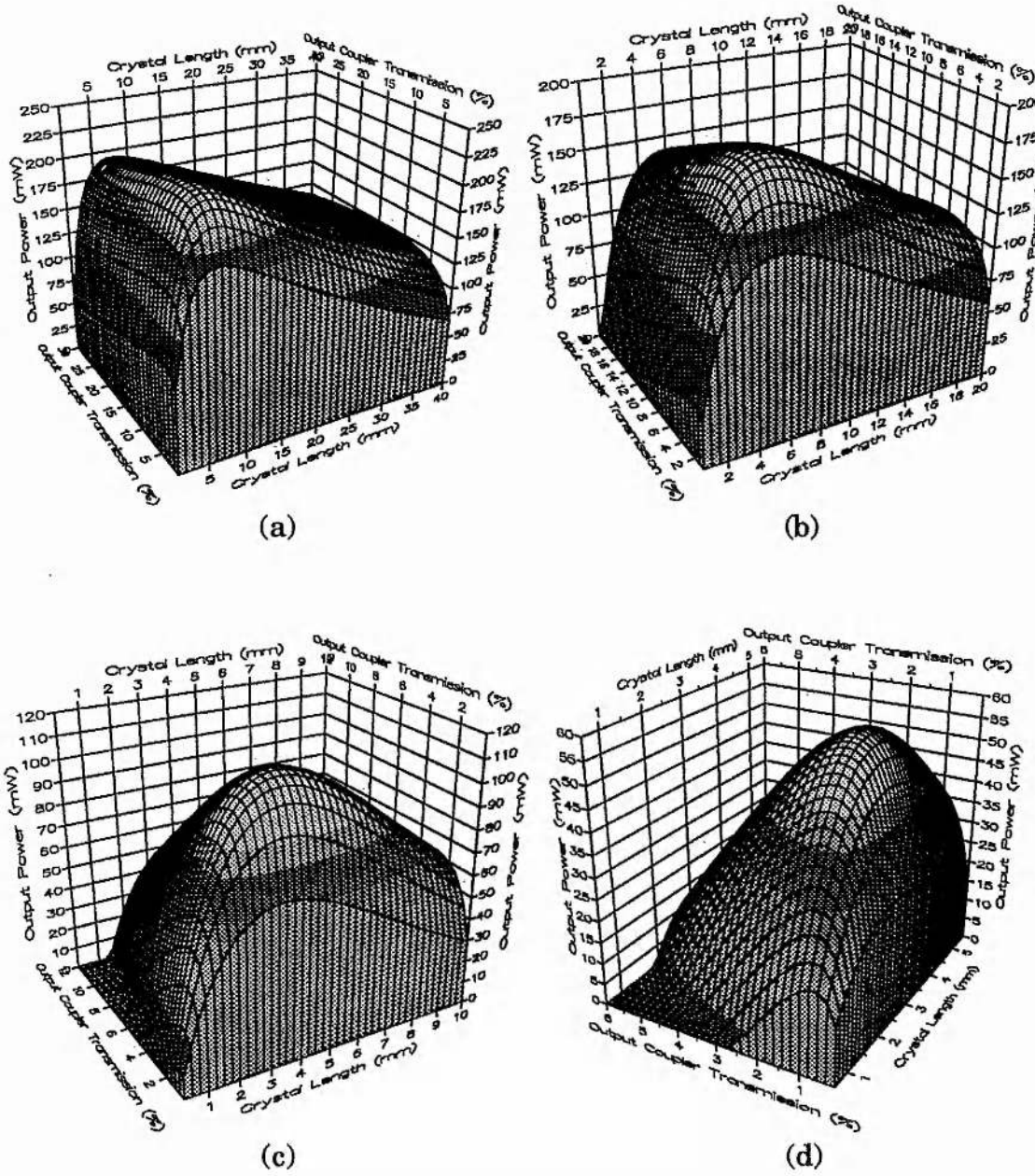

Figure 3.4.3 Calculated 946 nm laser output powers versus the crystal length, L, and the output coupler transmission, T, for the cases of Gaussian beam pumping at pump power of 360 mW. $\omega_p/\omega_0 = 1$ is assumed. a) ω_0=20 μm, b) ω_0=30 μm, c) ω_0=50 μm, and d) ω_0=70 μm.

Reference

[1] I. P. Alcock, A. I. Ferguson, D. C. Hanna and A. C. Tropper, "Continuous-wave oscillation of a monomode neodymium-doped fibre laser at 0.9 μm on the $^4F_{3/2}$-$^4I_{9/2}$ transition", *Opt. Comm.*, Vol. 58, No. 6, (1986) 405;

[2] T. Y. Fan and R. L. Byer, "Continuous-wave opertion of a room-temperature, diode-laser-pumped, 946-nm Nd:YAG laser", *Opt. Lett.*, Vol. 12, No. 10, (1987) 809;

[3] W. P. Risk and W. Lenth, "Room-temperature, continuous-wave, 946-nm Nd:YAG laser pumped by laser-diode arrays and intracavity frequency doubling to 473 nm", *Opt. Lett.*, Vol. 12, No. 12, (1987) 993;

[4] G. J. Dixon, Z. M. Zhang, R. S. F. Chang, and N. Djeu, "Efficient blue emission from an intracavity-doubled 946-nm Nd:YAG laser", *Opt. Lett.*, Vol.13, No.2, (1988) 137;

[5] W. P. Risk, R. Pon, and W. Lenth, "Diode laser pumped blue-light source at 473 nm using intracavity frequency doubling of a 946 nm Nd:YAG laser", *Appl. Phys. Lett.*, Vol. 54, No. 17, (1989) 1625;

[6] R. Allen, L. Esterowitz, L. Goldberg and J. F. Weller, "Diode-pumped 2 μm holmium laser", *Electron. Lett.*, Vol. 22, No. 18, (1986) 947;

[7] G. J. Kintz, L. Esterowitz and R. Allen, "CW diode-pumped Tm^{3+}, Ho^{3+}:YAG 2.1 μm room-temperature laser", *Electron. Lett.*, Vol. 23, No. 12, (1987) 616;

[8] H. Hemmati, "Efficient holmium:yttrium lithium fluoride laser longitudinally pumped by a semiconductor laser array", *Appl. Phys. Lett.*, Vol. 51, No. 8, (1987) 564;

[9] T. T. Fan and R. L. Byer, "Modeling and cw operation of a quasi-three-level 946 nm Nd:YAG laser", *IEEE J. Quantum Electron.*, Vol. QE-23, No. 5, (1987) 605;

[10] W. P. Risk, "Modeling of longitudinally pumped solid-state lasers exhibiting reabsorption losses", *J. Opt. Soc. Am. B*, Vol. 5, No. 7, (1988) 1412;

[11] R. Beach, *et al.*, "Q-switched laser at 912 nm using ground-state-depleted

neodymium in yttrium orthosilicate", *Opt. Lett.*, Vol. 15, No. 18, (1990) 1020;

[12] L. F. Johnson, J. E. Geusic, and L. G. VanUitert, "Coherent oscillations from Tm^{3+}, Ho^{3+}, Yb^{3+} and Er^{3+} ions in yttrium aluminum garnet", *Appl. Phys. Lett.*, Vol. 7, No. 5, (1965) 127;

[13] A. A. Kaminskii, *Laser Crystals*, springer-Verlag, Germany, 2nd Ed., (1990) 392;

[14] F. Tong, W. P. Risk, R. M. Macfarlane and W. Lenth, "551 nm diode-laser-pumped upconversion laser", *Electron. Lett.*, Vol. 25, No. 20, (1989) 1389;

[15] R, C. Stoneman and L. Esterowitz, "Efficient, broadly tunable, laser-pumped Tm:YAG and Tm:YSGG cw lasers", *Opt. Lett.*, Vol. 15, No. 9, (1990) 486;

[16] B. F. Aull and H. P. Jenssen, "Vibronic interactions in Nd:YAG resulting in nonreciprocity of absorption and stimulated emission cross section", *IEEE J. Quantum Electron.*, Vol. QE-18, No. 5, (1982) 925;

[17] H. G. Danielmeyer, "Progress in Nd:YAG lasers", Chap. 1, *Lasers*, A. Levine and A. J. DeMaurer, Eds., Vol. 4, USA, (1976);

[18] R. D. Maurer, "Operation of a Nd^{3+} glass optical maser at 9180 Å", *Appl. Opt.*, Vol. 2, No. 1, (1963) 87;

[19] L. F. Johnson and R. A. Thomas, "Maser oscillations at 0.9 and 1.35 microns in $CaWO_4$:Nd^{3+}", *Phys. Rev.*, Vol. 131, No. 5, (1963) 2038;

[20] R. W. Wallace and S. E. Harris, "Oscillation and doubling of the 0.946-μ line in Nd:YAG", *Appl. Phys. Lett.*, Vol. 15, No. 4, (1969) 111;

[21] M. Birnbaum, A. W. Tucker and P. J. Pomphrey, "New Nd:YAG laser transitions $^4F_{3/2}$-$^4I_{9/2}$", *IEEE J. Quantum Electron.*, Vol. QE-8, No. 6, (1972) 501;

[22] M. Birnbaum and A. W.Tucker, "Nd:YALO oscillation at 0.930 μm at 300 K", *IEEE J. Quantum Electron.*, Vol. QE-9, No. 1, (1973) 46;

[23] M. Birnbaum, A. W. Tucker and C. L. Fincher, "CW room-temperature laser operation of Nd:CAMGAR at 0.941 and 1.059 μ", *J. Appl. Phys.*, Vol. 49, No. 5,

(1978) 2984;

[24] T. M. Baer, "Diode laser pumping of solid-state lasers", *LF / EO* , June, (1986) 82;

[25] R. L. Byer, "Diode laser pumped solid-state lasers", *Science* , Vol. 239, Feb., (1988) 742;

[26] W. Koechner, *Solid-State Laser Enginering* , Springer-Verlag, Germany, 2nd Ed., (1988);

[27] G. M. Zverev, Yu. D. Golyaev, E. A. Shalaev and A. A. Shokin, "Neodymium activated yttrium-aluminum-garnet (YAG:Nd) lasers", *J. Sov. Laser Research* , Vol. 8, No. 3, English Transl., (1987) 189;

[28] J. P. Hurrell *et al.* , "Optical phonons of yttrium aluminum garnet", *Phys. Rev.*, Vol. 173, No. 3, (1968) 851;

[29] P. F. Liao and H. P. Webber, "Fluorescence quenching of the $^4F_{3/2}$ state in Nd-doped yttrium aluminum garnet (YAG) by multiphonon relaxation", *J. Appl. Phys.*, Vol. 45, No. 7, (1974) 2931;

[30] E. H. Carlson and G. H. Dieke, "The state of the Nd^{3+} ion as derived from the absorption and fluorescence spectra of $NdCl_3$ and their Zeeman effects", *J. Chem. Phys.*, Vol. 34, No. 5, (1961) 1602;

[31] T. Kushida, S. Kinoshita, T. Ohtsuki and T. Yamada, "Multiphonon relaxation rate pumped level to upper laser level in YAG:Nd", *Solid State Comm.*, Vol. 44, No. 9, (1982) 1363.

Chapter 4

Q-Switching of Continuously Pumped Quasi-Three-Level Lasers

4.1 Introduction

Following the discussion in the previous chapter about the cw performance of lasers exhibiting reabsorption losses, we now embark on the analysis of pulsed quasi-three-level lasers in this chapter.

As we know, Q-switching is a widely used laser technique to obtain intense and short bursts of laser oscillation. A simple picture of Q-switching is that the cavity feedback or the cavity losses, or in other words, the quality factor Q of the optical resonator, is switched by some means from an initial high loss (low Q) state to a low loss (high Q) state. In the low Q state the gain or population inversion ΔN can build up to a very high value without oscillation. In the high Q state the threshold drops down to a low value and the intracavity photons thus experience an extremely high net gain, which results in a very short, intense burst of laser output (a giant pulse [1-3]). The second process dumps most of the energy stored in the pumped atoms, ions or molecules into the optical field. The final effect of Q-switching is just like a cw laser output being compressed tightly in the time domain but with the same amount of output energy. The typical Q-switched pulse duration is few tens of nanoseconds and depends on the pump power.

Since the laser output energy in the Q-switched case is hardly changed

from its cw counterpart, the peak power can be increased to a very high value, which, as we will discuss in chapter 6, is very important for nonlinear optical processes. In the case of second harmonic generation, the induced second harmonic power depends much more on fundamental peak laser power than on average power.

Because of the existence of a lower laser level population in the so-called quasi-three-level laser, the common Q-switching theories, for example in Ref. [2] and [4], need to be modified. A picture of the physical processes involved in lasers exhibiting reabsorption losses will be given in this chapter. In our analysis, Nd:YAG will be chosen as our laser material and the theory will accordingly be developed for the 946-nm line. But, of course, the results derived will be applicable to other Q-switched lasers, either three- or four-level. The notation used here will largely be the same as in the previous chapter.

4.2 Rate-equations

In order to write out the rate-equations for the 946-nm transition of the Nd^{3+} ion in a YAG crystal, we first briefly review some of the characteristics associated with this particular line.

For the 946-nm transition, as discussed in chapter 3, each individual level of the upper manifold ($^4F_{3/2}$) or the ground manifold ($^4I_{9/2}$) can be assumed in a state of thermal equilibrium with the other levels within the same manifold under steady-state pumping. But in the case of Q-switching, the dynamic equilibrium state associated with the cw case will no longer apply because of the perturbation caused in each period by the Q-switching

action. So the issue of the rethermalisation rate is once again important. In the case of the cw Nd:YAG laser, the rethermalisation rates are not too critical as long as they are faster than the pump rate. The thermalisation rates (nonradiative) within the manifolds of both the upper laser level (R_1) and lower laser level (Z_5) for the 946-nm transition are believed to be higher than 10^8 s^{-1} [5], so thermalisation can be assumed in cw operation. But in the Q-switching case, where the pulse width is in the range 10-100 nanoseconds, the thermalisation rates must be more closely examined and this we now do.

The rethermalisation speed of the $^4I_{9/2}$ level in our case is also the lifetime of the lower laser level (Z_5), since the termination of the 946-nm transition is the upmost level of the ground manifold. The effect of lower laser level lifetime has been discussed in Ref. [6] for the 1.064-μm laser line. The lifetime of the lower laser level of the 946-nm transition is believed to be in the range of 10^{-11} - 10^{-12} s due to phonon resonance [5,7], which is at least a couple of orders shorter than the time parameters involved in the Q-switching operation. The population of the lower laser level can hence be assumed to rethermalise throughout the Q-switched pulse.

For the upper laser level, the rate of rethermalisation within the manifold is more difficult to assess. The upper laser level (R_1) is the lower of two levels (R_1 and R_2) in the $^4F_{3/2}$ manifold. Because the transitions between R_1 and R_2 are dominated by non-resonant phonon processes, the transition probabilities are normally quoted to be of the order or less than 10^8 s-1 [5,7]. In conventional (flashlamp pumped) Q-switched Nd:YAG lasers, where pulse durations of the order of 10 ns are involved [8,9], the usual procedure in analysis is to assume complete thermalisation within the upper state manifold. In the present system, the Q-switched pulse

durations are generally significantly longer (40-80 ns) because of the lower gains and longer cavity decay times in this case. The assumption of complete thermalisation will therefore be even more valid in our case, and this is the viewpoint we now adopt in the subsequent theoretical treatment. However, in view of the uncertainties regarding upper level thermalisation rates, we believe that this issue could well do with further scrutiny in the future.

To start with, let us write down the elementary rate equations for the cavity photon number S(t), the upper laser level population $n_b(t)$, and the lower laser level population $n_a(t)$ within the cavity mode. They are

$$\frac{dS(t)}{dt} = K\,[n_b(t) - n_a(t)] - \frac{S(t)}{\tau_c} \quad , \tag{4.2.1a}$$

$$\frac{dn_b(t)}{dt} = f_b\,R - f_b\,\frac{n_2(t)}{\tau} - f_b\,K\,[n_b(t) - n_a(t)]\,S(t) \quad , \tag{4.2.1b}$$

$$\frac{dn_a(t)}{dt} = -f_a\,R + f_a\,\frac{n_2(t)}{\tau} + f_a\,K\,[n_b(t) - n_a(t)]\,S(t) \quad , \tag{4.2.1c}$$

where τ_c is the cavity decay time; R is the total effective pumping rate; τ is the upper laser manifold life time; $n_2(t)$ is the population of the $^4F_{3/2}$ manifold; and K is the stimulating coupling coefficient between photons and atoms, which value is also dependent on the pump beam geometry and the optical intensity profile of the cavity mode. Here, instead of writing in terms of population and photon densities, as we did in section 3.4, Eqs. (4.2.1) are written in the integral forms of Eqs. (3.4.1).

Similarly to Eqs. (3.4.1), Eq. (4.2.1b) and (4.2.1c) can be combined into one single equation in terms of the total population inversion n(t) in the cavity

mode volume, i.e.,

$$\frac{dn(t)}{dt} = (f_a + f_b)\, R - \frac{n(t) - n^0}{\tau} - (f_a + f_b)\, K\, n(t)\, S(t) \quad , \qquad ((4.2.2)$$

where n^0 is the equilibrium population inversion in the mode volume. Unlike the situation in the cw case, the intra-cavity photon number S(t) and the population inversion n(t) are now time dependent. To analyse these time dependent values, we divide each Q-switching period into 3 intervals, they are the pumping interval, the pulse build-up interval, and the pulse output interval. In the next few sections, we will discuss each interval separately and then combine them together to draw a complete picture of a continuously pumped, repetitively Q-switched, quasi-three-level laser.

4.3 Pumping Interval

The main features during the pumping interval are that the cavity feedback is completely blocked, i.e., the quality factor Q stays at a low value, and the internal optical oscillation is completely stopped, that is S(t)=0, while the pump rate remains at R. Rewriting Eq. (4.2.2) in this situation, we obtain

$$\frac{dn(t)}{dt} = (f_a + f_b)\, R - \frac{n(t) - n^0}{\tau} \quad . \qquad (4.3.1)$$

For the pulsed pumping case, the population inversion or the energy storage increase only after each pump pulse is turned on at t=0, and the energy storage can always be taken to be zero before or at t=0 due to the relatively shorter lifetime of the upper state manifold compared to the pump

period. The solution for Eq. (4.3.1) thus can be written as

$$n(t) = [(f_a + f_b)\, R\, \tau + n^o] \times [1 - \exp(-t/\tau)] \quad , \qquad (4.3.2)$$

which gives the maximum population inversion as $(f_a + f_b)\, R\tau + n^o$ obtained by increasing the pumping time to ∞. Since the equilibrium population inversion n^o is negative in any circumstances for quasi-three level laser systems and its magnitude is very close to the lower laser level thermal population at the state of thermal equilibrium, the requirement of the same population inversion as in a four-level laser system will then need a more powerful pump source to give an extra pump rate to overcome the existing population in the lower laser level. The message from Eq. (4.3.2) is also that whenever a Q-switched, quasi-three level laser system is concerned as soon as the upper laser level population equals the lower laser level population, the performance of a Q-switched, quasi-three level laser system will be similar to a Q-switched, four-level laser system.

For a continuously pumped Q-switched laser with a high pulse repetition rate, a large amount of the residual population inversion will still remain undecayed and contribute to the next pulse. So the calculation of population inversion during one pump interval should also take the residual population inversion left by the previous pulse into account. The solution for Eq. (4.3.1) then becomes

$$n(t) = n_f \exp(-t/\tau) + [(f_a + f_b)\, R\, \tau + n^o] \times [1 - \exp(-t/\tau)] \quad , \qquad (4.3.3)$$

where n_f is the residual inversion of the previous pulse; and t starts from the end of the previous pulse.

4.4 Pulse Build-up Time

The pulse build-up time is generally defined as the interval during which the cavity losses are low, starting from the opening of the Q-switch and extending to some point close to the leading edge of the Q-switched pulse. In practice, however, it is impossible to precisely define the pulse build-up time, since the Q-switch itself may have a finite opening time, and the resulting pulse has a finite risetime. However, it would still be useful to estimate the pulse build-up time of a laser system under the assumption that the losses in the laser cavity are switched instantaneously at t=0 to some much lower value, and the end of the pulse build-up interval is defined as that point on the leading edge of the Q-switched pulse where the photon number S(t) just becomes equal to the steady-state photon numbers S_{ss}. The steady-state photon number is the total photon number which is present in the laser cavity when the laser runs in cw mode with the same continuous pumping source. Different definitions of the end of the pulse may result in a slightly different values for the pulse build-up time, these differences are usually negligible.

During the pulse build-up interval, the photon number in the cavity is so small that the depletion of the population inversion by the coherent field can be neglected. Also, because this period is short compared to the upper-level lifetime (τ) and the pumping rate is moderate when cw diode lasers are used, we can further neglect relaxation and pumping effects during this interval and assume that the population inversion n(t) stays approximately equal to its initial value n_i all through the pulse build-up time. The photon rate equation (Eq. 4.2.1a) can then be written to a good approximation as

$$\frac{dS(t)}{dt} \approx K n_i S(t) - \frac{S(t)}{\tau_c} \quad . \tag{4.4.1}$$

We now introduce an important parameter, the initial population inversion ratio. If the threshold population inversion is denoted by n_{th}, then the initial population inversion ratio r is defined by

$$r = \frac{n_i}{n_{th}} \quad , \tag{4.4.2}$$

which, as we will see in our later discussion, is one of the primary factors controlling the performance of a Q-switched laser.

At steady state, as in the case of a cw laser, the total population inversion is clamped at the threshold value. From Eq.(4.4.1) we then have

$$\frac{dS((t)}{dt} \approx K n_{th} S(t) - \frac{S(t)}{\tau_c} \approx 0 \quad , \tag{4.4.3}$$

which gives the threshold inversion in terms of the coupling coefficient K and the cavity lifetime τ_c to be

$$n_{th} \approx \frac{1}{K \tau_c} \quad . \tag{4.4.4}$$

Replacing the coupling constant K in Eq. (4.4.1) by Eq. (4.4.4), we have

$$\frac{dS(t)}{dt} = \frac{(n_i/n_{th} - 1)}{\tau_c} S(t) = \frac{(r - 1)}{\tau_c} S(t) \quad , \tag{4.4.5}$$

with the solution

$$S(t) = S_i \exp[(r-1)\, t/\tau_c] \qquad (4.4.6)$$

where S_i is the initial number of photons present in the cavity at t=0. Unless some artificially injected external signal (e.g., in the case of injection locking) or pre-oscillation in the case of special Q-switching techniques (e.g., in Ref [10]) is present in the laser cavity, the initial noise value in the cavity will be equivalent to $S_i \approx 1$ or a few photons. If we accept that the pulse build-up interval ends when the photon number reaches S_{ss}, the pulse build- up time T_b is then given by

$$T_b \approx \frac{\tau_c}{r-1} \times \ln\left(\frac{S_{ss}}{S_i}\right) \quad . \qquad (4.4.7)$$

In the previous chapter, we have discussed parameters determining the cw output power, and from this the internal steady-state photon number S_{ss} can be derived for substitution in Eq. (4.4.7).

Measurement of the pulse build-up time permits us to roughly estimate important parameters relevant to the Q-switched laser performance. The gradient from the plot of T_b against (r-1) immediately gives the cavity decay time, once the value of S_{ss} is known from cw operation. It is important to bear in mind, however, that the derivation of Eq. (4.4.7) assumes ideal, step-function Q-switching. In a real situation, especially in the case of high pump powers, the pulse build-up time could be of the same order as the Q-switching time, when a slow Q-switching analysis would be necessary [11].

4.5 Pulse Output Interval

Obviously, most of the practical interest is concerned with the pulse output period, when parameters such as pulse energy, pulse width, peak pulse power and pulse shape etc. are required. To analyse the optical pulse features of a Q-switched laser, we go back to the basic rate equations Eq. (4.2.1) and Eq. (4.2.2). We neglected the pumping and relaxation effects during the pulse build-up interval in the last section. It is natural then to leave out the pumping and relaxation terms as well during the pulse output interval, since the pulse output interval is usually much shorter than, or at least comparable to, the length of the pulse build-up interval. The rate equations Eq. (4.2.1a) and Eq. (4.2.2) thus can be written to a good approximation in this pulse-output interval as

$$\frac{dS(t)}{dt} = K\,[n(t) - n_{th}]\,S(t) \quad , \tag{4.5.1}$$

and

$$\frac{dn(t)}{dt} \approx -\,(f_a + f_b)\,K\,n(t)\,S(t) \quad , \tag{4.5.2}$$

where we have used the relation Eq. (4.4.4) in Eq. (4.5.1). Dividing Eq. (4.5.1) by Eq. (4.5.2), we get the differential equation

$$\frac{dS(t)}{dn(t)} = \frac{n_{th} - n(t)}{(f_a + f_b)\,n(t)} \quad . \tag{4.5.3}$$

Although this last equation has been derived to describe the pulse output interval in particular, it is applicable to the pulse build-up time as well due to the common assumptions used. With the initial conditions that $n(t_i) = n_i$

$=r \cdot n_{th}$ and $S(t_i) = S_i \approx 1$, Eq. (4.5.3) may be integrated to describe both the pulse build-up interval and the pulse output interval when the following expression is obtained

$$(f_a + f_b)\, S(t) = n_i - n(t) - \frac{n_i}{r} \ln\left(\frac{n_i}{n(t)}\right) \quad , \tag{4.5.4}$$

where we have neglected the initial photon number S_i. The only parameters in this expression are the initial inversion n_i, and the ratio $r = n_i/n_{th}$ by which this initial inversion exceeds threshold. Apart from the constant (f_a+f_b), Eq. (4.5.4) is exactly the same as that derived for a Q-switched four-level laser. The reason is that the rate equation Eq. (4.5.4) has been normalised to the threshold inversion n_{th} in the case of the quasi-three level laser. This threshold inversion is greater than in the case of a true four level laser, and hence implies the need for increased pump power. So, the expressions for Q-switched pulses in quasi-three level lasers and four-level lasers are the same, as long as they are expressed in terms of the ratio r as in Eq. (4.5.4). The difference between the two cases resides solely in the different threshold inversions.

We can now manipulate Eq. (4.5.4) to yield some important parameters of the Q-switched pulses. Let us start with the derivation of the pulse energy. It is the final population inversion at the end of a pulse that decides the extracted energy, and thus the pulse energy. At the end of the pulse the cavity photon number S(t) approaches zero, and n(t) approaches this final population inversion n_f. Eq. (4.5.4) then provides an implicit expression for n_f, namely

$$1 - \frac{n_f}{n_i} - \frac{1}{r} \ln\left(\frac{n_i}{n_f}\right) = 0 \quad . \tag{4.5.5}$$

In the case of 946-nm Nd: YAG laser, the initial stored energy in the upper laser manifold is

$$n_{2i}\, h\upsilon = \frac{n_{bi}\, h\upsilon}{f_b} \qquad (4.5.6)$$

at the beginning of Q-switching and the final stored energy is

$$n_{2f}\, h\upsilon = \frac{n_{bf}\, h\upsilon}{f_b} \quad , \qquad (4.5.7)$$

after the pulse is extracted. The total energy extracted will thus be the difference between the initial and final stored energies in the upper laser manifold, i.e.,

$$U = (n_{2i} - n_{2f})\, h\upsilon \quad .$$

Since the total ion number, n_0, is primarily the sum of the population of the manifold including the upper laser level and the population of the ground state manifold, i.e.

$$\frac{n_b}{f_b} + \frac{n_a}{f_a} = n_0 \quad ,$$

and the population inversion is expressed as

$$n = n_b - n_a \quad ,$$

the total extracted energy can then be expressed in terms of the initial population inversion, n_i, and the final population inversion, n_f, as

$$U = (n_{2i} - n_{2f})\, h\upsilon = \frac{(n_i - n_f)\, h\upsilon}{f_a + f_b} \quad . \tag{4.5.8}$$

Taking the cavity losses into account, the final pulse energy coupled out is then given by

$$U_{out} = U \times \frac{T}{\delta} = \frac{(n_i - n_f)\, h\upsilon\, T}{(f_a + f_b)\, \delta} \quad , \tag{4.5.9}$$

where T is the transmission of the output coupler; and δ is the total cavity loss which does not include the reabsorption losses.

To assess a Q-switched laser system, we can define an extraction efficiency η for the conversion of initial stored energy into Q-switched pulse energy correspondingly for a quasi-three-level laser, i.e.,

$$\eta = \frac{n_{2i} - n_{2f}}{n_{2i}} = \frac{n_i - n_f}{f_a\, n_o + n_i} \quad , \tag{4.5.10}$$

where $n_0 = n_1 + n_2$ is the total ion doping number within the cavity mode volume, of course, Eq.(4.5.10) can also be expressed in terms of the ion concentrations by dividing both the denominator and the numerator by the cavity mode volume. In the case when the lower laser level population $n_a = f_a n_0$ is negligible, Eq. (4.5.10) then reduces to the extraction efficiency derived for a four-level laser system [4].

By combining Eq. (4.5.5) and Eq. (4.5.10), we obtain a single equation which relates the extraction efficiency to the parameter r, that is

$$\eta\left(1+\frac{f_a n_o}{n_i}\right)+\frac{1}{r}\ln\left[1-\left(1+\frac{f_a n_o}{n_i}\right)\eta\right]=0 \quad ,$$

or

$$1-\left(1+\frac{f_a n_o}{n_i}\right)\eta=\exp\left[-\left(1+\frac{f_a n_o}{n_i}\right)r\eta\right] \quad . \tag{4.5.11}$$

If $f_a n_o/n_i \approx 0$, Eq. (4.5.11) again reduces to the case of a four-level laser system. So in order to get maximum extraction efficiency, i.e., the same efficiency in a quasi-three-level laser system as in a four-level laser system, the initial population inversion must be increased to the point where the lower laser level population is only a very small portion of the initial inversion. Fig. (4.5.1) shows the curve of $(1+ f_a n_o/n_i)\eta$ against the initial inversion ratio r.

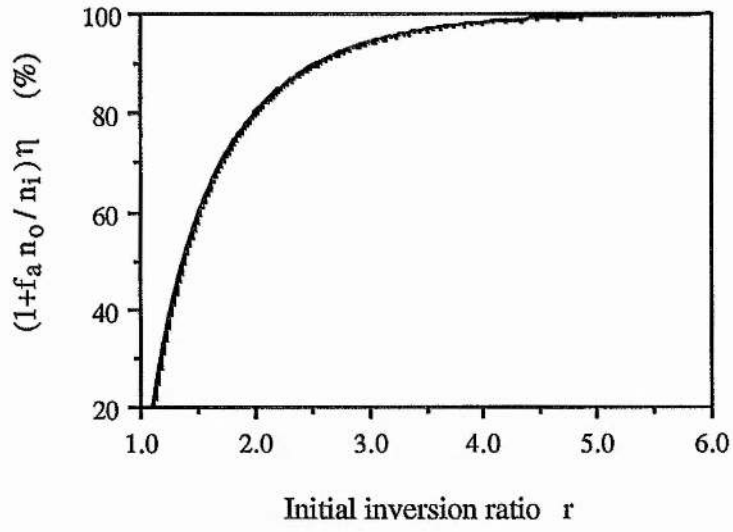

Figure 4.5.1 Energy extraction efficiency η in a Q-switched quasi-three-level laser as a function of the initial inversion ratio r with the lower laser level thermal population as a parameter

The second parameter of practical interest for a Q-switched laser is the peak pulse power. To derive its expression, let us first look at what happens during the pulse output duration. The cavity photon number S(t) reaches its peak value S_p at the instant when the instantaneous inversion n(t) passes through the threshold value n_{th} during extraction. Rewriting Eq. (4.5.4) with these values, we have

$$(f_a + f_b) S_p = n_i - n_{th} - \frac{n_i}{r} \ln(\frac{n_i}{n_{th}}) \quad . \tag{4.5.12}$$

So the peak intracavity photon number is

$$S_p = \frac{n_{th} (r - 1 - \ln r)}{f_a + f_b} \quad , \tag{4.5.13}$$

and the peak output power, which is coupled out from the Q-switched laser, is

$$P_p = \frac{S_p h\upsilon T}{\tau_c \delta} = \frac{n_{th} h\upsilon c T}{2 L (f_a + f_b)} (r - 1 - \ln r) \quad , \tag{4.5.14}$$

where τ_c is the cavity decay time; L is the optical cavity length; and c is the light speed in vacuum.

From the pulse parameters determined above, the pulse duration τ_p can then be derived, which for the approximation of a squre pulse is

$$\tau_p \approx \frac{U_{out}}{P_p} = \frac{(n_i - n_f) \tau_c}{(r - 1 - \ln r) n_{th}} \quad ,$$

or

$$\tau_p \approx \frac{(1 + \frac{f_a n_o}{n_i}) r \eta \tau_c}{r - 1 - \ln r} \quad . \tag{4.5.15}$$

Though the pulse duration given by Eq. (4.5.15) is about 20% smaller than the duration (FWHM) derived iteratively from Eq. (4.5.2) as discussed below, Eq.(4.5.15) does reveal the dependence of the pulse duration on the parameters r, τ_c and the lower laser level thermal population $f_a n_o$. An exact solution for the pulse duration or for the pulseshape in more general can be obtained numerically, however, by substituting Eq. (4.5.4) into the rate equation Eq. (4.5.2). The resultant single differential equation is

$$\frac{dn(t)}{dt} = - K n(t) [n_i - n(t) - \frac{n_i}{r} \ln(\frac{n_i}{n(t)})] \quad , \tag{4.5.16}$$

which can then be integrated, starting with $n(o)=n_i$ at the Q-switching time t=0, in the form

$$\frac{1}{\tau_c} \int_0^t dt = - n_{th} \int_{n_i}^{n} \frac{dn(t)}{n(t) [n_i - n(t) - \frac{n_i}{r} \ln(\frac{n_i}{n(t)})]} \quad . \tag{4.5.17}$$

This equation can be solved numerically. The values of n(t) versus time t so deduced can then be substituted into Eq. (4.5.4) to give an exact solution for the cavity photon number S(t) versus the time t. Fig. (4.5.2) illustrates some typical Q-switched pulse shapes for different degrees of initial population inversion plotted versus t / τ_c.

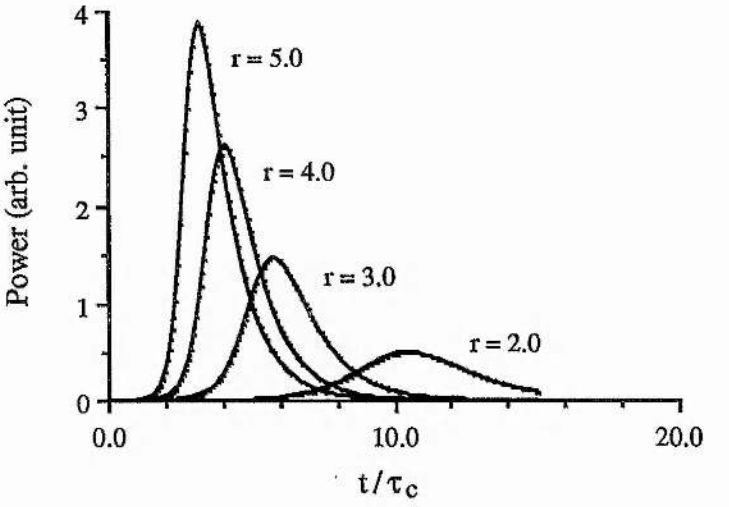

Figure 4.5.2 Numerically calculated Q-switched pulses for different initial population inversions.

From Eq. (4.5.14) and Fig. (4.5.2), it is obvious that the peak power of Q-switched pulses is closely related to the initial inversion ratio r. The requirement of high peak power for efficient second harmonic generation means that high pump power and low threshold laser system are preferred in order to increase the value r. In practice, however, the optical power of a pump source is usually limited, as in the case of a low power diode laser pumped system, which implies that only a laser system with low threshold can meet the requirement of high energy extraction efficiency and high pulse peak power. The development of a Q-switched 946-nm Nd:YAG laser pumped by a diode laser array is described in the next chapter.

References

[1] F. J. McClung and R. W. Hellwarth, "Giant optical pulsations from ruby", *J. Appl. Phys.*, Vol. 33, No. 3, (1962) 828;

[2] W. G. Wagner and B. A. Lengyel, "Evolution of the giant pulse in a laser", *J. Appl. Phys.*, Vol. 34, No. 7, (1963) 2040;

[3] C. C. Wang, "Optical giant pulses from a Q-switched laser", *Proc. IEEE* , Vol. 51, (1963) 1767;

[4] A. E. Siegman, *Lasers*, Univ. Science Books, California, (1986);

[5] G. M. Zverev, Yu. D. Golyaev, E. A. Shalaev and A. A. Shokin, "Neodymium activated yttrium-aluminum-garnet (YAG:Nd) lasers", *J. Sov. Laser Research* , Vol. 8, No. 3, English Transl., (1987) 189;

[6] T. Y. Fan, "Effect of finite lower level lifetime on Q-switched lasers", *IEEE J. Quantum Electron.*, Vol. 24, No. 12, (1988) 2345;

[7] T. Kushida, S. Kinoshita, T. Ohtsuki and T. Yamada, "Multiphonon relaxation rate from pumped level to upper laser level in YAG:Nd", *Solid State Comm.*, Vol. 44, No. 9, (1982) 1363;

[8] V. A. Zaporozhchenko, A. V. Kachinskii, V. V. Rakush, A. A. Stavrov and N. A. Tylets, "Generation of short light pulses by laser with fast Q-switching", *Instrum. & Exp. Tech.*, Vol. 29, No. 3, (1986) 700;

[9] J. M. Heritier, D. K. Aubuchon and R. Aubert, "Thermal effects in high power Q-switched lasers", *Proc. SPIE-Int. Soc. Opt. Eng.*, Vol. 895, (1985) 20;

[10] D. C. Hanna, B. Luther-Davies, H. N. Rutt and R. C. Smith, "A two-step Q-switching technique for producing high power in a single longitudinal mode", *Opto-Electron.*, Vol. 3, (1971) 163;

[11] J. E. Midwinter, "The theory of Q-switching applied to slow switching and pulse shaping for solid state lasers", *Brit. J. Appl. Phys.*, Vol. 16, (1965) 1125.

Chapter 5

CW and Q-switched 946-nm Nd:YAG Laser Systems

Following the modelling of CW and Q-switched quasi-three level laser systems in the last two chapters, we now, in this chapter, describe and discuss the experimental set-ups and results for our 946-nm Nd:YAG lasers. Experience of the quasi-three level laser line in Nd:YAG was first gained by setting up a CW version of a 500-mw diode laser array pumped 946-nm Nd:YAG laser (section 5.2). This Nd:YAG laser was also pumped by a Ti:Sapphire laser, since this demonstrated the ultimate performance of which the 946-nm Nd:YAG laser was capable when pumped with a diffraction-limited laser beam that had a better beam quality and a narrower spectral width than that obtainable from diode lasers. Before we discuss the Nd:YAG lasers, we will firstly consider coupling optics for diode lasers in section 5.1. The requirement of high peak power for second harmonic generation led to the development of a Q-switched version of the Nd:YAG laser. In section 5.3, the experimental set-up and performances of the first diode laser pumped 946-nm Nd:YAG laser to be Q-switched will be discussed.

5.1 Coupling Optics for Diode Laser Pumping

Diode laser pumped solid-state lasers have shown great success in most aspects, such as efficiency, compactness, and reliability etc. However, the unique beam properties of diode lasers (including diode laser arrays)

require special care in the design of coupling optics for efficient optical collection and pumping. Diode-pumped solid-state lasers typically fall into either end-pumped or side-pumped categories (chapter 1). Each pumping geometry has its own advantage. With end-pumping geometries, a higher efficiency, almost the quantum limit, can be reached due to the excellent spatial overlap between pump beam and laser cavity mode (see for example [1]). Side-pumping geometries are comparatively less efficient, but can be more easily scaled to high pump power levels by simply integrating more diode lasers or diode laser arrays in the diode laser pumping head [2]. Intermediate between these two geometries, there have also been hybrid schemes, such as the TFR (tightly folded resonator) geometry [3,4] and the multi-facet-pumping geometry [5]. In this section, we restrict discussion to some common end-pumping geometries.

The output beam properties of diode lasers discussed in chapter 2 show that special considerations are involved in designing coupling optics. The large divergence of the diode laser beam requires the collection optics to have a large numerical aperture (NA) in order to collect most of the optical power. The different divergences in the planes parallel and perpendicular to the diode laser junction produce an elliptical beam. A beam with a full-angle divergence of 40 ° (FWHM), typical of most diode lasers in the perpendicular plane, would need a collimator with numerical aperture of 0.34 to collect 75% of the total output power. Obviously, further increase in the optical collecting power can be achieved by reducing the beam divergence or using lenses with even larger numerical apertures. The first option is not realistic since, as we have discussed before in chapter 2, optimisation of other important performance parameters, such as current threshold, fundamental transverse mode etc., has already decided the thicknesses of the diode laser active layers and hence the beam divergence.

The most common solution to the power collecting problem is the use of simple, short focal length (large numerical aperture) lenses manufactured for the purpose. Single lenses with short focal lengths, however, would introduce substantial aberrations into the beam. These aberrations appear as distortions and nonuniformity of the wavefront. In certain low-level applications requiring only moderate wavefront quality, commercial Gradient Index (GRIN) lenses, moulded aspheric glass lenses and ball lenses may be sufficient. However, in most cases, the requirements of minimum spot size / maximum collimation mean that the transformation of a beam must be limited only by its natural divergence, without additional aberrations arising from the coupling optics, that is, a diffraction limited transformation is required.

To minimise lens aberrations, compound lenses combining several elements are most commonly employed for collimating and focusing diode laser beams. The elements in a compound lens are manufactured from glasses of different refractive index, and with radii of curvature such that the sum of their aberrations cancel out. Large numerical aperture compound lenses must be of short focal length to keep the working aperture of the lens within reasonable dimensions. Optimum alignment of such lenses thus requires tight tolerances in all dimensions of adjustment.

A compound lens with diffraction-limited transformation, however, will not correct astigmatism of diode laser output beams unless it is specially designed. The amount of astigmatism of diode lasers may appear negligible, being about 2 to 8 μm for index-guided diode lasers [6], but it must be remembered that this occurs at a point where the total area of the beam is only a few square microns. So the astigmatism must be considered when a diffraction-limited focusing spot is required. The simplest way to

correct astigmatism is to use a weak cylindrical lens. Either a positive or negative lens can be used. The object is to add refracting power to one axis or subtract it from the other. In this way the apparent light source origin is the same in both planes. If the amount of astigmatism of a diode laser is known, the correcting cylindrical lens can then be incorporated in the collimator. If the cylindrical lens is placed before the collimating lens, the cylindrical radius is given approximately by [7]

$$R = \frac{\phi^2}{8 n D (1 - \cos \theta)} , \qquad (5.1.1)$$

where ϕ is the clear aperture of the lens, n is the refractive index of the lens, D is the astigmatic distance, and θ is the smaller of the half acceptance angle of the collimator or the divergence of the laser. If the cylindrical lens is placed after the collimating lens, the thin lens assumption can be made and the astigmatism can be treated as a defocus. The combined astigmatism corrected collimator should have unchanged focal length, f, in one plane, and corrected focal length, f + D, in the orthogonal plane, where D is the amount of astigmatism which takes a positive value when the focal point of the collimating lens is located at the front facet of the diode laser and negative when it is at the virtual waist inside the diode laser. The focal length of the correcting cylindrical lens thus derived is

$$f' = -\frac{f(f+D)}{D} . \qquad (5.1.2)$$

A specially designed anamorphic gradient-index lens, which has different index profiles in the two orthogonal planes, can also serve to correct astigmatism as well as to collimate the beam [8]. Unfortunately, diode lasers vary in their amount of astigmatism from manufacturer to

manufacturer, from type to type, and from diode to diode, and also, astigmatism in an individual diode laser is dependent upon its output power. Hence, in most cases, a cylindrical lens is used separately rather than in a combined version in the collimator.

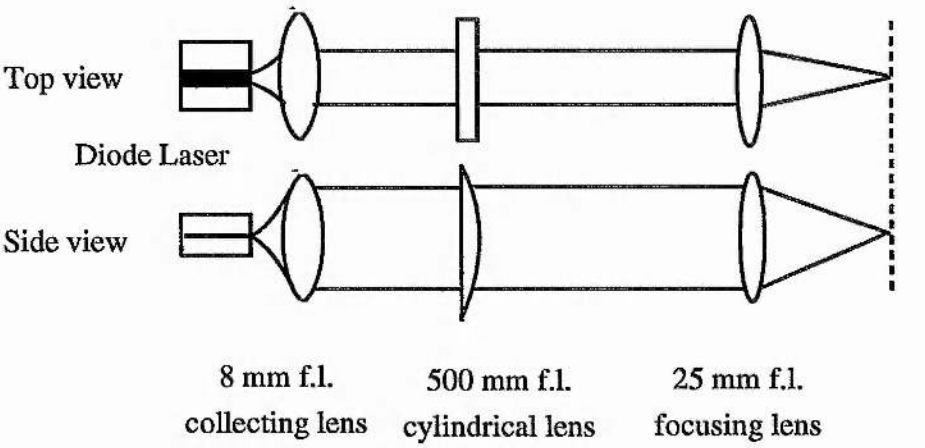

(a)

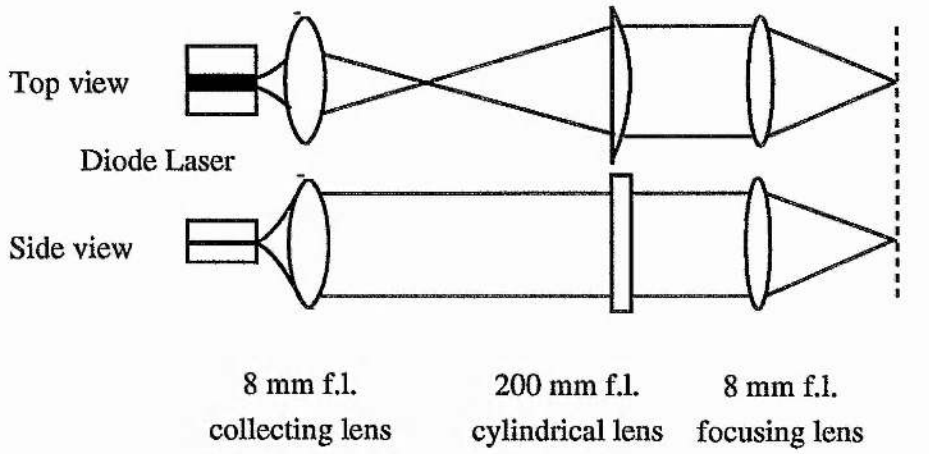

(b)

Figure 5.1.1 Two optical coupling systems employing cylindrical lens as the compensating element. (a) The conventional use of a weak cylindrical lens [9]; (b) the cylindrical lens was used to reduce both the astigmatism and ellipticity of the diode laser beam [10].

Figs. 5.1.1 (a) and (b) show two types of set-up for longitudinal pumping [9,10]. One advantage of the second set-up in Figs. 5.1.1 is that it reduces not only the astigmatism but also the ellipticity of the beam. Some similar set-ups have also been designed to collect and focus linear diode laser arrays [11,12]. In recent developments, the above approach has been extended to multiple arrays hence extending the scalability of longitudinal pumping [13,14].

Another common scheme for diode laser output coupling is the use of prisms. The original idea of using prisms was to expand one side of a collimated beam and thus make it nearly circular. In principle, any large magnification can be obtained by just adding more and more prisms. The total beam expanding magnification M can be given by

$$M = m^n \quad , \tag{5.1.3}$$

where n is the number of prisms and m is the magnification of the equivalent prisms. In practice, however, a pair of prisms is good enough to cope with most situations. The commercial anamorphic prism pair is such a system. It consists of two identical prisms mounted at an incident angle, which is close to Brewster's angle, to the incoming beam, see Fig. 5.1.2. Since the output of the diode laser is strongly linearly polarised in the plane of the active layer of a diode laser, this arrangement minimises the reflection losses. Beam expansion by prisms reduces the effective aperture, and thus can also be used to remove any sidelobes or highly divergent radiations so attaining a degree of spatial filtering. Hence, a more circular and uniform beam can be obtained.

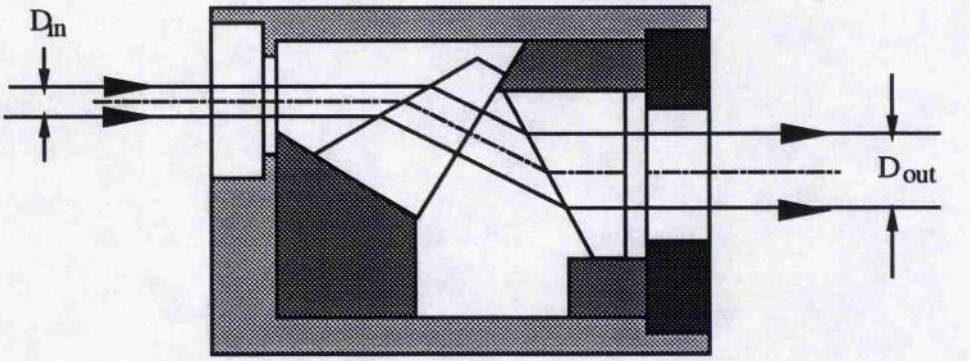

Figure 5.1.2 Anamorphic prism pair

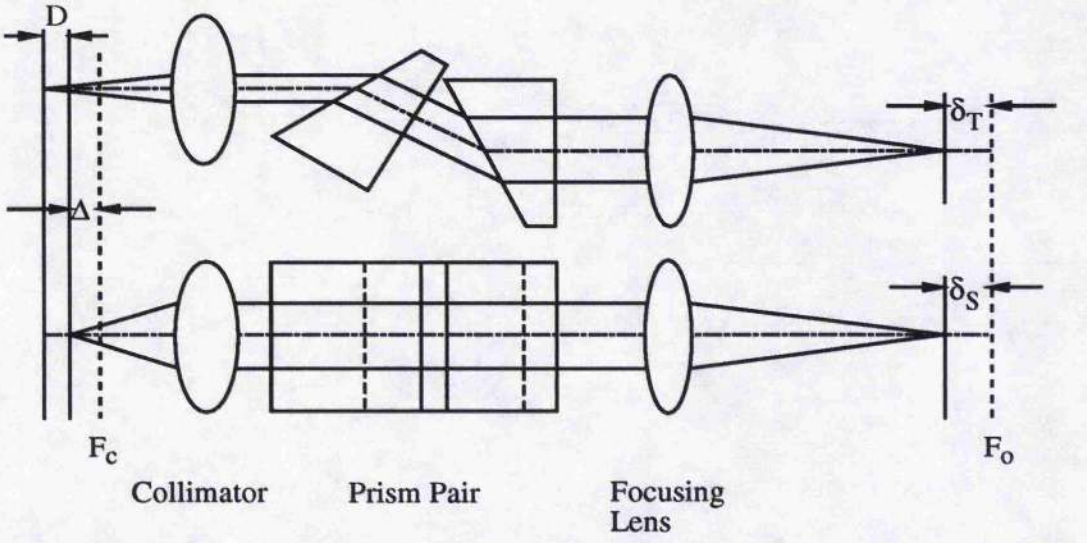

Figure 5.1.3 Anamorphic beam focusing optics working as beam shaping, spatial filtering, and astigmatism correction

Another useful contribution from anamorphic prisms is its astigmatism correction capability, which may not be so obvious. It is known, however, that astigmatism can be generated when a nonparallel plane wave passes through a prism. When this effect is applied inversely, a certain amount of astigmatism already present can be corrected. Fig. 5.1.3 shows a schematic of typical coupling optics including an anamorphic prism pair. The collimated beam in the plane parallel to the active layer (top view) is expanded to have the same size as the beam diameter in the

plane perpendicular to the active layer (side view). In the paraxial approximation, two separate equations, one for each plane, can be written accordingly [15], i.e.,

$$D + \Delta = M_T^2 \ \delta_T \quad , \tag{5.1.4}$$

for the top view, and

$$\Delta = M_S^2 \ \delta_S \quad , \tag{5.1.5}$$

for the side view, where D is the astigmatic distance of the diode laser; Δ is the distance from the laser facet to the front focal point, F_c, of the collimator; δ_T and δ_S are the distances from the rear focal point, F_o, of the focusing lens to the image point in the top and side view planes respectively; M_T and M_S are the magnifications of the top and side views respectively. To correct the astigmatism,

$$\delta_T = \delta_S = \delta \tag{5.1.6}$$

must be satisfied which gives

$$D = (M^2 - 1) \Delta \quad , \tag{5.1.7}$$

where $M=M_T / M_S$, is the magnification of the anamorphic prism pair.

In our experiment, we adopted a coupling scheme consisting of an anamorphic prism pair. The set-up was the same as that shown in Fig. 5.1.3. A 10-stripe array (SDL-2432-H1) with an emitting area of 100 μm x 1 μm and beam divergence of 10 ° x 40 ° full width at half maximum was used

as our optical source. The collimator used was a Melles Griot 4-element 6.5-mm focal length lens, the focusing lens was a 2-element 25.6-mm focal length lens. An anamorphic prism pair with magnification of 4 times was firstly chosen as the beam from the diode laser array had an aspect ratio of 1:4. In the case of multi-stripe diode-laser arrays, a little confusion may arise in the optical analysis, i.e., whether it should be treated with Gaussian optics or geometric optics.

Our 10-stripe diode-laser array can be pictured as ten coherent emitters, incoherently related, and spread over an area of 100 μm x 1 μm. A general approach to the problem would treat the output from a single stripe as a coherent Gaussian beams and the output from the whole array would then be given by the incoherent (intensity) addition of the individual Gaussian beams. Here we content ourselves by treating each source as a point source emitting a cone of rays. The ray traces produce a picture, as shown in Fig. 5.1.4, in which only the rays from the two outmost stripes are depicted. Light from a single stripe was collimated by the collimator, but no longer propagated parallel to the optical axis. The collimated beams cross the optical axis at the rear focal plane of the collimator. The small inclination angle of a single beam was further reduced by the anamorphic prism pair. For a prism pair with magnification of M, the inclination angle reduces to

$$\theta_{out} = \frac{\theta_{in}}{M} \quad , \tag{5.1.8}$$

where θ_{in}, θ_{out} are the inclination angles before and after the prism pair respectively. If the dimension of each diode stripe is negligible compared with the whole width of diode laser array, the image of the array formed at the focal plane of the focusing lens will have the width of

$$l' = \frac{m}{M} l \quad , \tag{5.1.9}$$

where m is the magnification of the lens system, i.e., the ratio of the focal length of the focusing lens to the focal length of the collimator in our case, and l is the diode laser array length. Taking M=4, m≈4 (25.6 mm / 6.5 mm), and l=100 μm, the coupling system in Fig. 5.1.4 would then give the image width of ~100 μm, while the height would be magnified by m=4.

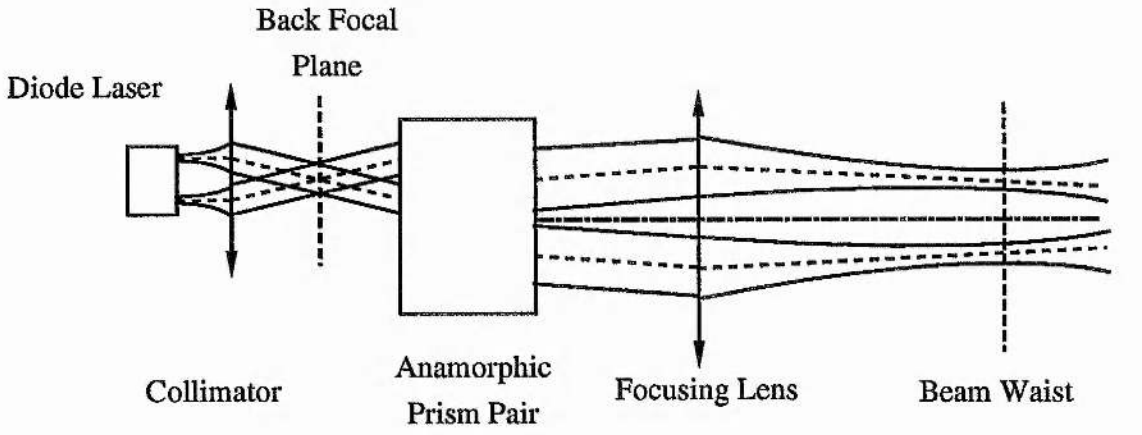

Figure 5.1.4 Propagation of a beam bundle from a multistripe diode laser through coupling optics consisting of a collimator, an anamorphic prism pair and a focusing lens.

For the diode laser array we used, the inclination angles of even the outmost beams were small compared to the diffraction angles involved. The divergence of the whole beam could thus be determined by the divergence of the single stripes. The transformation of the 40° x 10° (FWHM) beam through the coupling optics shown in Fig. 5.1.4 would give a beam with divergence of 10° x 10° (FWHM). Thus excellent overlap between this reshaped circular diode laser beam and pumped laser cavity mode can be achieved. Bear in mind, however, that the generated beam waist was still strongly elliptical due to the linear diode laser array emitting area. Only in

the far field, a more uniform and circular beam could be obtained.

5.2 CW Laser

Fig. 5.2.1 shows our experimental set-up of a diode laser array pumped cw 946-nm Nd:YAG laser. The output from a 500-mW 10-stripe diode laser array (SDL-2432-H1) was collected, beam shaped and focused into a 2-mm long Nd:YAG rod (1.1.% doping) with the coupling system shown in Fig. 5.1.3. The whole pumping unit, including the diode laser array and the coupling optics, was mounted on a three-dimension translation stage. The laser cavity was formed by the input plane surface of the Nd:YAG crystal and a spherical mirror with a radius of curvature of 50 mm.

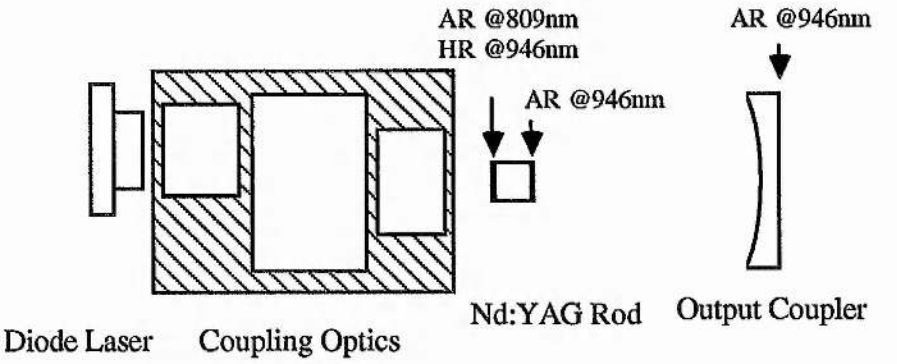

Figure 5.2.1 End-pumped cw 946-nm Nd:YAG laser

The diode laser array was driven by a SDL-800 Laser Diode Driver, which could provide drive current up to 1000 mA in both current and optical power control modes. An adjustable current limit control was built in to protect the diode laser from accidental overdrive. The SDL-800 also included a thermoelectric cooler driver, which allowed the diode laser temperature to be set between -10°C and 30°C with resolution of 0.1°C. Such a

temperature range resulted in a diode laser wavelength coverage of ~11nm for this particular laser (see Fig. 2.4.3). At the specified 500-mW output power level, the optimum temperature for pumping the Nd:YAG crystal was found to be 1.7°C, corresponding to a wavelength of 809 nm.

The primary difficulties with the 946-nm transition in Nd:YAG laser, as we have discussed in chapter 3, are the low gain cross section (about an order of magnitude less than that of the 1.064-μm transition [16]) and the thermal reabsorption loss due to the lower laser level population. In order to prevent parasitic oscillation at 1.064 μm, dichroic coatings [17] and intracavity prisms [18,19] have been used in earlier flash lamp or pulsed xenon ion laser pumped Nd:YAG lasers. Because of the improved availability of extremely low loss coatings able to withstand high mean powers, the dichroic coating approach was often adopted in more recent works [20-22]. The selectivity is provided in the present configuration through the choice of dichroic coatings optimised for 946 nm.

The Nd:YAG rod used in our experiment had a length of 2 mm and a diameter of 3 mm. The input surface of the rod had a reflectance of 99.7% at 946 nm and greater than 85% transmission at the pump wavelength, 809 nm. The intracavity surface of the rod was antireflection coated at 946 nm (reflectiviy < 0.35%). The output coupler was chosen between one of two mirrors with reflectance of 98.9% and 98% at 946 nm. Both mirrors had a radius of curvature of 50 mm. The suppression of 1.064-μm parasitic oscillation was achieved by using dichroic coatings on the output couplers with low residual reflection of less than 30% at 1.064 μm. The temperature dependencies of threshold and output slope efficiency were investigated by mounting the Nd:YAG rod in a temperature controlled copper block. By adjusting the drive current to a Peltier cooler on which the copper block was

mounted, the Nd:YAG rod could be set at any temperature between room temperature and -5°C. The laser output power is shown as a function of incident pump power in Fig. 5.2.2 for different rod temperatures. At temperature far below room temperature, condensation formed very quickly on the rod surfaces, so dry nitrogen was blown on the surfaces to keep away moisture present in the air. From Fig. (3.4.2 d), we can see that the length of the crystal used in the experiment was slightly shorter than the optimum crystal length for a pump beam with beam waist around 70 μm. Because of the divergence of the focused pump beam, the effective pump beam radius was actually larger than the pump beam waist measured, so the experimental results we got agreed well with the prediction from the theoretical model of uniform pumping geometry developed in chapter 3.

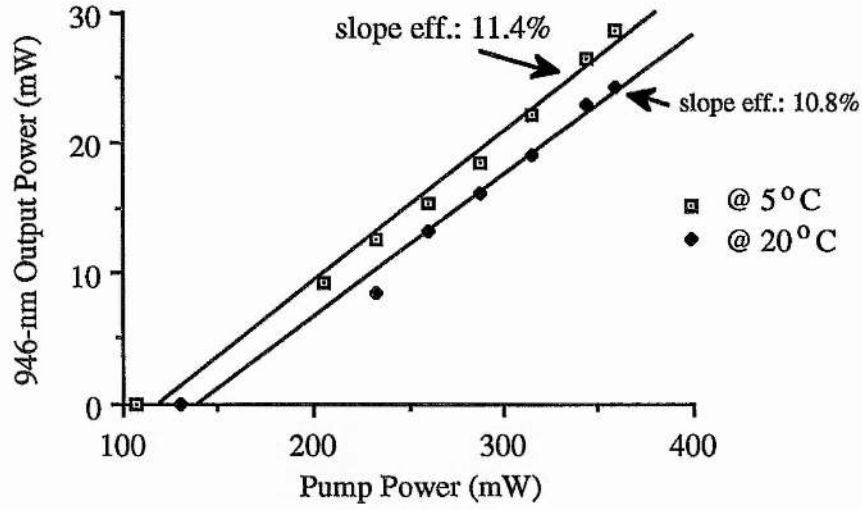

Figure 5.2.2 CW 946-nm output power versus incident diode laser power at 5°C and 20°C.

The temperature dependence of the threshold pump power shown in Fig. 5.2.2 indicated that the thermal reabsorption loss due to the lower laser level population is very significant. According to our modelling in chapter

3, both small pump beam size and laser cavity mode size are prefered in order to get low threashold and high slope efficiency. The pump beam from the 500-mW diode laser array, however, can only be focused down to the order of 100 μm with the coupling optics discussed in the last section, which consequently restricts any further reduction of laser cavity mode size, as higher order modes might start to oscillate. In the experiment, the optimum cavity mode waist was found by adjusting the output coupler position. The resonator thus found was very close to the hemispheric resonator with the mode waist at the input end of the Nd:YAG rod. Further increase in the cavity length, higher order modes started appear and the resonator became unstable.

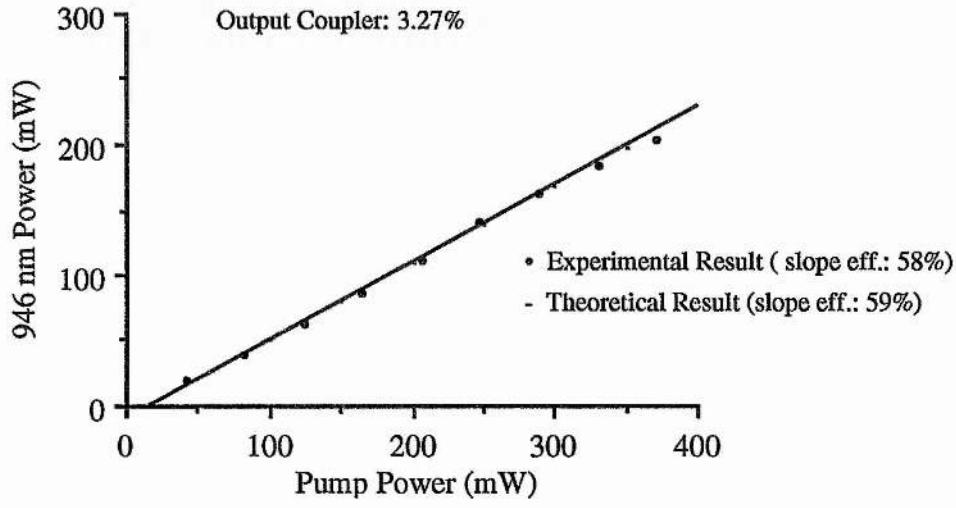

Figure 5.2.3 Theoretical and experimental CW 946-nm output power versus incident pump power. In calculation, absorption coefficient α=8cm^{-1}, and w_p(pump beam waist) = w_o (cavity mode waist) = 15μm.

The experiment was further carried out by using an Argon ion laser pumped Ti:Sapphire laser as the pumping source. The narrow spectral width and fundamental transverse mode operation of Ti:Sapphire laser

provided not only the high pumping efficiency (with absorption coefficient of 8 cm^{-1} compared to the effective absorption coefficient 5 cm^{-1} for the case of diode laser pumping) but also the diffraction limited pumping spot size in Nd:YAG crystal. The Ti:Sapphire laser beam was focused by a lens with a 25.6-mm focal length. Fig. 5.2.3 shows the experimental result and theoretical calculation of 946-nm output power as a function of the incident pump power. It is obvious from Fig. (3.4.3 a) that the length of the Nd:YAG crystal used here was not optimised in the case of Ti:Sapphire laser pumping, otherwise the optical pumping efficiency can be even higher.

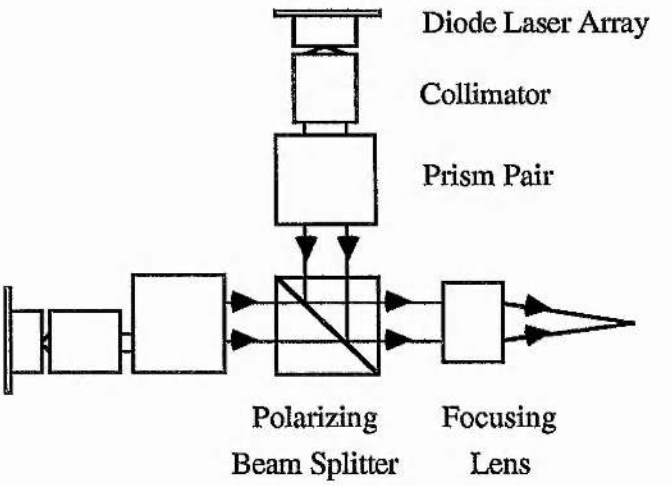

Figure 5.2.4 Combination of two beams from diode lasers by using a polarising beam splitter.

The results from Ti:Sapphire laser pumping demonstrated that the quality of pumping beam is a key factor in the 946-nm Nd:YAG laser. The problem left for diode laser pumping is then how to increase the pump power intensity. The most common method of beam combination is the reverse use of polarising beam splitter for the end pumping geometry. As shown in Fig. 5.2.4, the output beams of two diode laser arrays were combined by using a polarising beam splitter. Further scaling-up of diode

laser pump power is possible by geometric multiplexing approaches. But no matter what the exact geometric multiplexing method used, the rule is that the lower beam quality direction determines the pump spot size, and the ratio of the beam quality in the two directions determines how many sources can be combined without increasing the pump volume. Different geometric multiplexing set-ups for end pumping have been reported by other researchers [13,14].

No attempt, however, was made in our experiment to combine beams from different diode lasers. With more and more diode lasers available, these beam combination methods will be very useful in future diode laser pumping research and applications.

5.3 Q-switched Laser

The development of a Q-switched diode laser pumped 946-nm Nd:YAG laser was our next interest. The high peak power provided by a Q-switched laser is advantageous for frequency doubling the laser output to the blue - a prime objective of this work.

Based on the development of the diode laser pumped cw Nd:YAG laser discussed in the last section, we built our Q-switched version by adding an acousto-optic Q-switch inside the laser cavity. To minimise the insertion loss, the Q-switch was cut at the Brewster angle on both ends. It thus also acts as a linear polariser defining the laser output polarisation. The Q-switch was made of lead molybdate with an optical path length of 14 mm. Fig. 5.3.1. shows the Q-switched laser cavity.

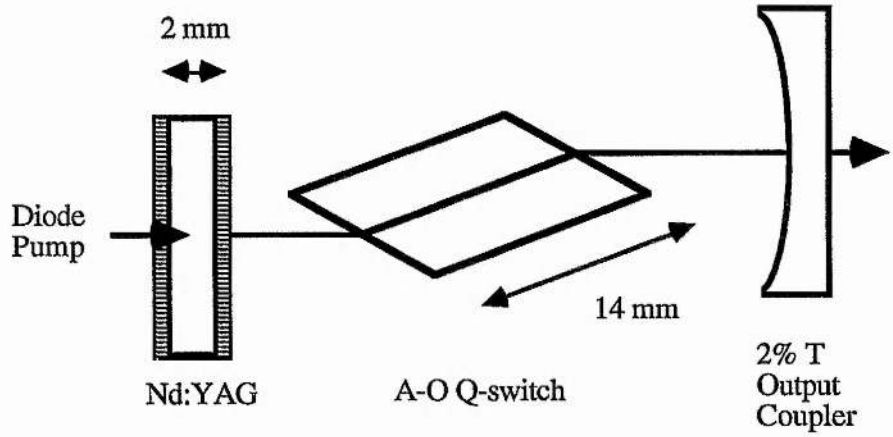

Figure 5.3.1 The Q-switched 946-nm Nd:YAG laser cavity layout

As the laser was operating close to its stability limit, the introduction of a Brewster angled element led to significant differences in the laser beam in the two planes (tangential and sagittal defined by the Brewster angled surfaces). The effective path lengths of the equivalent empty resonator differed by 4.9 mm in the two planes [23], which resulted in an elliptical output beam and an elliptical waist at the input end of the Nd:YAG rod. To improve the spatial overlap between the laser cavity-mode and the pumped crystal volume around the focal region, a x3 anamorphic prism pair was used instead of the x4 one which was incorporated in pumping the cw laser. The pump beam was thus focused into a more elliptical image at the focal point of the focusing lens, the minimum spot being 20 x 80 μm radius to half maximum intensities, hence better matching the cavity mode. The optimum location of this minimum spot was found to be inside the Nd:YAG rod and close to the input surface. The reduced aperturing of the x3 anamorphic prism pair also increased the total coupling efficiency from the 60 % of the original x4 anamorphic prism pair to 72 %. Optimum performance was found with effective cavity lengths of 49.4 mm and 44.5 mm in the tangential and sagittal plane respectively, for which the

corresponding cavity mode waists were 40 μm and 69 μm respectively at the input surface of the Nd:YAG rod.

With 360 mW of pump power incident on the Nd:YAG crystal, which was maintained at room temperature, 29 mW of cw 946 nm output was obtained without the intracavity Q-switch. This reduced slightly to 24.3 mW of cw TEM_{00} output when the Q-switch was inserted into the cavity in its low loss state. The former system, however, tended to lase in a TEM_{10} mode due to the mismatch between the pump beam and the fundamental transverse laser cavity mode. This was not the case in the latter system where a TEM_{00} output beam was reliably produced. The threshold pump powers were 102 mW and 109 mW respectively, which indicated that the insertion loss of the Q-switch was effectively compensated by the better matching between the pump mode and the cavity mode due to the astigmatism introduced by the Q-switch. In both systems a 1.1% transmitting output coupler was used. When Q-switched at a repetition rate of 1.5kHz, the pulses had peak powers of 51 W and a duration of 76 ns, which corresponded to an average output power of 7 mW.

By changing to a 2% output coupler, 60-W peak power pulses of 68.5-ns duration were obtained with an average power of 7.4 mW. When the crystal was cooled down to 5°C, the average output power increased to 8.4 mW, in the form of pulses of 76 W peak power, 62 ns duration, and 5.6 mJ energy.

The Q-switched pulses produced at different pump levels are shown in Fig. 5.3.2. In this study the Nd:YAG crystal was maintained at 5°C and the 2% transmission output coupler was used. As expected, the pulse build-up time decreased with increasing pumping, while the pulse energy increased.

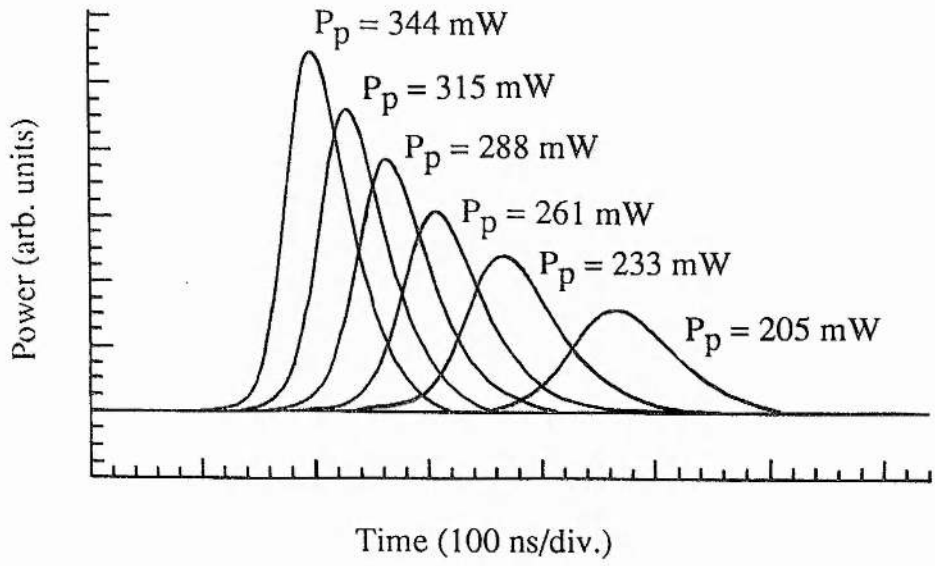

Figure 5.3.2 Q-switched 946-nm pulses at different diode pump levels (P_p)

To analyse the Q-switched laser performance, we rewrite Eq. 4.4.7, 4.5.14, and 4.5.15 here in the forms of

$$T_b = \frac{A\,\tau_c}{r-1} \quad , \tag{5.3.1}$$

$$P_p = \frac{n_{th}\,h\upsilon\,c\,T}{2L\,(f_a + f_b)}\,(r - 1 - \ln r) \quad , \tag{5.3.2}$$

$$\tau_p = \frac{r\,\eta'(r)\,\tau_c}{r-1\ln r} \quad , \tag{5.3.3}$$

where A is a dimensionless number determined by the definition of the starting point for each pulse (if this is taken as that point in the pulse when

the photon flux equals the steady state flux then A≈26 in our case); f_a and f_b are the population fractions of the lower laser level in the ground-state manifold and of the upper laser level in the $^4F_{3/2}$ manifold respectively; c is the speed of light; τ_c is the cavity decay time as determined by parasitic and transmission loss, but not including reabsorption; n_{th} is the threshold population inversion in the laser mode volume; T is the output transmission; L is the optical cavity length; $h\upsilon$ is the laser photon energy; and $\eta'(r)$ is the energy extraction efficiency for a standard four level system where lower level effects are negligible (see Eq. 4.5.11), and which has been widely tabulated and graphed as a function of r, the ratio of pump power to the threshold pump power, see for example [24].

The experimental results are plotted against their appropriate functions in Fig. 5.3.3. The cavity decay time can be determined from the gradients of the graphs of pulse build-up time and pulse duration to be 10.8 ns and 11.6 ns respectively, which shows a slightly higher cavity loss than we expected. It is believed that this was due to the fact that the laser was operating on several longitudinal modes. The pulse parameters derived above will hold more accurately for a single-longitudinal-mode laser since each mode will have a slightly different effective gain and therefore different pulse build-up time and pulse width.

The experimental results showed good agreement with the quasi-three level Q-switched laser theory. It demonstrated that the dynamic behaviour of the Q-switched laser as described by Eq. (5.3.1) to (5.3.3) is essentially unaltered compared with the standard 4-level laser treatment [24]. The sole effect of the lower laser level population is to increase the pump power requirement to reach the threshold as given by Eq. (3.3.14), and hence to reduce the value of r attained at a given level of pump power. However,

provided the data is displayed as a function of r, the dynamic behaviour of the 946 nm system is similar to that of systems where lower level effects are negligible.

(a)

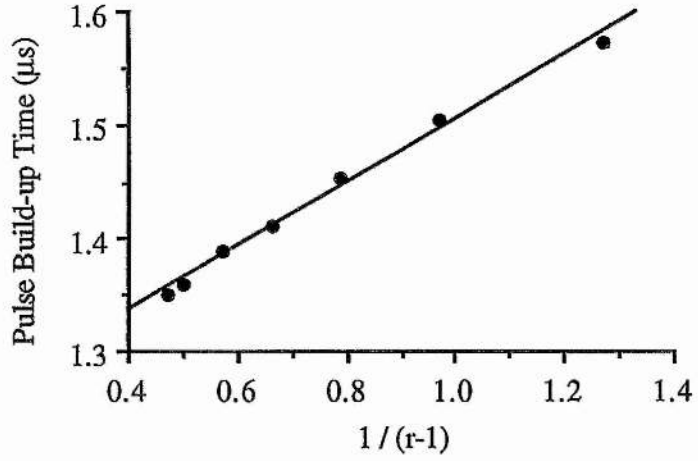

(b)

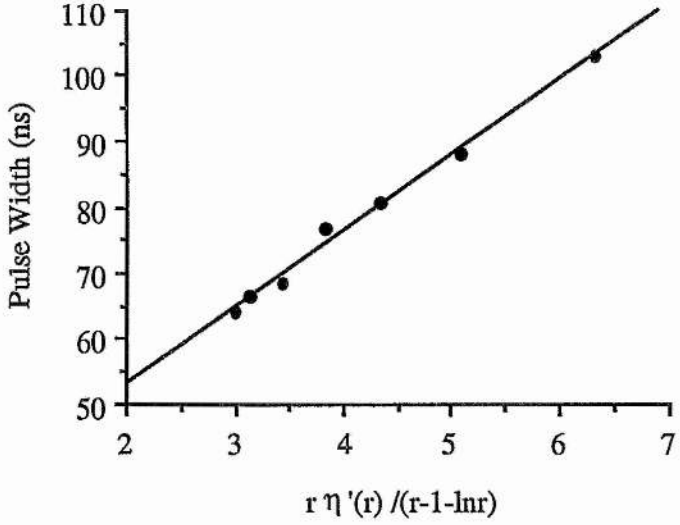

(c)

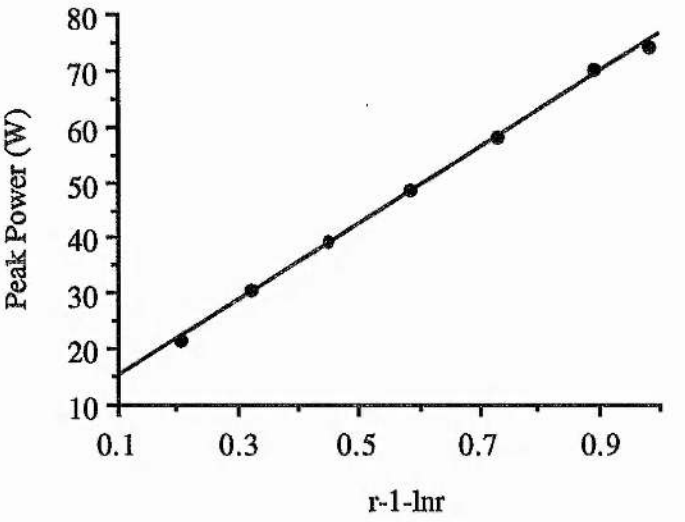

Figure 5.3.3 Q-switched pulse parameters as functions of the pump rate relative to threshold. (a) pulse build-up time, (b) pulse width, and (c) peak power. The Nd:YAG rod was kept at 5°C.

References

[1] E. A. P. Cheng and T. J. Kane, "High-power single-mode diode-pumped Nd:YAG laser using a monolithic nonplanar ring resonator", *Opt. Lett.*, Vol.16, No.7, (1991) 478;

[2] R. L. Burnham, "High-power transverse diode-pumped solid-state lasers", *Optics & Photonics News*, August (1990) 4;

[3] T. M. Baer, D. F. Head and P. Gooding, "High peak power Q-switched Nd:YAG laser using a tightly folded resonator", CLEO'90, (Anaheim, California, 1990) paper CMF2;

[4] M. S. Keistead and T. M. Baer, "10 W, TEM_{00} output from a diode-pumped, solid-state laser", CLEO'91, (Baltimore, Maryland, 1991) paper CFC3;

[5] P. Albers, C. Pfistner and H. P. Weber, "Highly efficient diode laser multiple end pumped Nd:YAG slab", CLEO'90, (Anaheim, California, 1990), paper CMF4;

[6] M. Long, "correcting astigmatism in diode lasers", Lasers & Optronics, Sept. (1989) 51;

[7] P. Kuttner, "Laser beam scanning", *Optical Engineering*, Vol.8, Marcel Dekker, New York, (1985) 352;

[8] E. Acosta, R. M. Gonzalez and C. Gomez-Reino, "Design of an anamorphic gradient-index lens to correct astigmatism of Gaussian laser beams", *Opt. Lett.*, Vol.16, No.9, (1991) 627;

[9] G. J. Kintz, R. Allen and L. Esterowitz, "CW and pulsed 2.8 μm laser emission from diode-pumped Er^{3+}:$LiYF_4$ at room temperature", *Appl. Phys. Lett.*, Vol.50, No.22, (1987) 1553;

[10] W. P. Risk, R. Pon and W. Lenth, "Diode laser pumped blue-light source at 473 nm using intracavity frequency doubling of a 946 nm Nd:YAG laser", *Appl. Phys. Lett.*, Vol.54, No.17, (1989) 1625;

[11] T. Brabec, F. Krausz, E. Wintner and A. J. Schmidt, "Longitudinal pumping of

lasers with multistripe laser diodes", *Appl. Opt.*, Vol.30, No.12, (1991) 1450;

[12] D. C. Shannon and R. W. Wallace, "High-power Nd:YAG laser end pumped by a CW, 10mm x 1μm aperture, 10-W laser-diode bar", *Opt. Lett.*, Vol.16, No.5, (1991) 318;

[13] T. Y. Fan, A. Sanchez and W. E. DeFeo, "Scalable, end-pumped, diode-laser-pumped laser", *Opt. Lett.*, Vol.14, No.19, (1989) 1057;

[14] S. C. Tidwell, J. F. Seamans, C. E. Hamilton, C. H. Muller and D. D. Lowenthal, "Efficient, 15-W output power, diode-end-pumped Nd:YAG laser", *Opt. Lett.*, Vol.16, No.8, (1991) 584;

[15] K. Tatsuno, R. Drenten, Carel ven der Poel, J. Opschoor and G. Acket, "Diffraction-limited circular single spot from phased array lasers", *Appl. Opt.*, Vol.28, No.21, (1989) 4560;

[16] B. F. Aull and H. P. Jenssen, "Vibronic interactions in Nd:YAG resulting in nonreciprocity of absorption and stimulated emission cross sections", *IEEE J. Quantum Electron.*, Vol. QE-18, No.5, (1982) 925;

[17] L. F. Johnson and R. A. Thomas, "Maser oscillations at 0.9 and 1.35 microns in $CaWO_4$:Nd^{3+}", *Phys. Rev.*, Vol.131, No.5, (1963) 2038;

[18] R. W. Wallace and S. E. Harris, "Oscillation and doubling of the 0.946 μ line in Nd^{3+}:YAG", *Appl. Phys. Lett.*, Vol.15, No.5, (1969)111;

[19] M. Birnbaum, A. W. Tucker and P. J. Pomphrey, "New Nd:YAG laser transitions $^4F_{3/2}$--$^4I_{9/2}$", *IEEE J. Quantum Electron.*, Vol. QE-8, No.6, (1972) 501;

[20] T. Y. Fan and R. L. Byer, "Modeling and cw operation of a quasi-three-level 946 nm Nd:YAG laser", *IEEE J. Quantum Electron.*, Vol. QE-23, No.5, (1987) 605;

[21] W. P. Risk and W. Length, "Room-temperature, continuous-wave, 946-nm Nd:YAG laser pumped by laser-diode arrays and intracavity frequency doubling to 473 nm", *Opt. Lett.*, Vol.12, No.12, (1987) 993;

[22] G. J. Dixon, Z. M. Zhang, R. S. F. Chang and N. Djeu, "Efficient blue emission

from an intracavity-doubled 946-nm Nd:YAG laser", *Opt. Lett.*, Vol.13, No.2, (1988) 137;

[23] H. W. Kogelnik, E. P. Ippen, A. Dienes and C. V. Shank, "Astigmatically compensated cavities for CW dye lasers", *IEEE J. Quantum Electron.*, Vol. QE-8, No.3, (1972) 373;

[24] A. E. Siegman, *Lasers*, Univ. Science Books, California, (1986).

Chapter 6

Second Harmonic Generation

Over the last three decades the field of nonlinear optics has become well established, as an inevitable consequence of the invention of the laser. Nonlinear optics now plays a very important role in the development of lasers. Recently the discoveries of new nonlinear materials and developments in nonlinear-crystal growth technology have provided this field with even more vitality. The purpose of this chapter is to outline some principles of nonlinear optics, and to derive some practical and useful formulae and equations, especially those for second harmonic generation (SHG), and at the same time, to clarify some confusions caused by differences in definition of nonlinear coefficient, the formalism used to describe the optical field, and the type of units used. In this chapter, MKS units will be adopted throughout the analysis.

6.1 Introduction to Nonlinear Optics

In classical linear optics, the induced dielectric polarisation of a medium is linearly related to the applied electric field, that is

$$\mathbf{P} = \varepsilon_0 \chi^{(1)} \mathbf{E} \quad , \tag{6.1.1}$$

where $\chi^{(1)}$ is the dielectric susceptibility, the superscripts (1) indicates that it is the first order susceptibility, which is usually called the linear susceptibility. When the high electric fields of laser beams are involved, the

above linear relation is no longer a good approximation. The induced polarisation should then be described by a power series in **E**, i.e.

$$\mathbf{P}(\mathbf{r},t) = \varepsilon_0 \left(\chi^{(1)} \mathbf{E} + \chi^{(2)} : \mathbf{E}^2(\mathbf{r},t) + \chi^{(3)} : \mathbf{E}^3(\mathbf{r},t) + \cdots \right) . \quad (6.1.2)$$

We now briefly discuss this nonlinear relation. The basic physical origin of Eq. (6.1.2) is the nonlinearities of the electronic motion induced by high electric fields, which is analogous to a breakdown of Hooke's law when a spring is subject to a strong pulling force. The quadratic term in Eq. (6.1.2) is responsible for phenomena such as second harmonic generation, sum frequency generation, optical rectification, difference frequency generation and optical parametric conversion. On the other hand the cubic term in Eq. (6.1.2) is the cause of effects such as third harmonic generation, stimulated Raman scattering, quadratic electro-optic (Kerr) effect, optical bistability, phase conjugation, self-focusing and two-photon absorption. As second harmonic generation is the main issue of this chapter, only the nonlinearity due to the quadratic term of Eq. (6.1.2) will be considered further here. Writing out the lowest order nonlinear polarisation separately, we have

$$\mathbf{P}^{(2)} = \varepsilon_0 \chi^{(2)} : \mathbf{E}^2(\mathbf{r},t) . \quad (6.1.3)$$

We will see later , this term is only finite in anisotropic media, and in order to describe anisotropic media the second order susceptibility $\chi^{(2)}$ in the last two equations will be a tensor by nature. The units of $\chi^{(2)}$ as defined above are metres volt^{-1}, or more commonly pm/v. However, there is an alternative convention which includes the free space permittivity within the second order susceptibility, namely

$$\mathbf{P}^{(2)} = \chi^{(2)} : \mathbf{E}^{2}(\mathbf{r},t) \ ,$$

and in this case the units of $\chi^{(2)}$ are Coulombs volt^{-2}. The former convention as defined by Eq. (6.1.3) will be adopted here.

As the general nonlinear process of Eq. (6.1.3) involves three-wave mixing in which two fields are combined to produce a third, a simple situation would then be where the field $\mathbf{E}$ has only two frequency components and is written as

$$\mathbf{E}(\mathbf{r},t) = \frac{1}{2}[\, \mathbf{E}_1(\mathbf{k}_1,\omega_1)\, e^{i(\mathbf{k}_1 \cdot \mathbf{r} - \omega_1 t)} + \mathbf{E}_2(\mathbf{k}_2,\omega_2)\, e^{i(\mathbf{k}_2 \cdot \mathbf{r} - \omega_2 t)} + \text{c.c.}\,] \ , \tag{6.1.4}$$

where c.c. refers to the complex conjugates of the other terms.

Now, the dyad product $\mathbf{E}^2$ in Eq. (6.1.3) becomes

$$\begin{aligned} \mathbf{EE} = \frac{1}{4}[\, & \mathbf{E}_1\mathbf{E}_1 e^{i(2\mathbf{k}_1 \cdot \mathbf{r} - 2\omega_1 t)} + \mathbf{E}_2\mathbf{E}_2 e^{i(2\mathbf{k}_2 \cdot \mathbf{r} - 2\omega_2 t)} \\ & + 2\mathbf{E}_1\mathbf{E}_2 e^{i[(\mathbf{k}_1+\mathbf{k}_2)\cdot\mathbf{r} - (\omega_1+\omega_2)t]} + 2\mathbf{E}_1\mathbf{E}_2 e^{i[(\mathbf{k}_1-\mathbf{k}_2)\cdot\mathbf{r} - (\omega_1-\omega_2)t]} \\ & + \mathbf{E}_1\mathbf{E}_1^* + \mathbf{E}_2\mathbf{E}_2^* + \text{c.c.}\,] \ . \end{aligned} \tag{6.1.5}$$

From the above it is apparent that the nonlinear polarisation will have two second harmonic components at frequencies $2\omega_1$ and $2\omega_2$, a sum frequency component at frequency $(\omega_1+\omega_2)$, a difference frequency component at frequency $(\omega_1-\omega_2)$, and a rectification signal (which leads to the

development of a dc voltage across the crystal). Now, if we limit our consideration only to the polarisation at the sum frequency ($\omega_1+\omega_2$) (second harmonic generation will then be the degenerate case $\omega_1 = \omega_2$), we have from Eq. (6.1.3) and Eq. (6.1.5)

$$\mathbf{P}^{NL}=\frac{1}{2}\varepsilon_o \chi^{(2)}(\omega_1+\omega_2) : [\, \mathbf{E}_1\mathbf{E}_2 e^{i(\mathbf{k}_1+\mathbf{k}_2)\cdot\mathbf{r}-i(\omega_1+\omega_2)t} + \text{c.c.}\,] \ . \quad (6.1.6)$$

If the nonlinear polarisation is also expressed in its complex form, the right side of the Eq. (6.1.6) becomes

$$\mathbf{P}^{NL}=\frac{1}{2}[\,\mathbf{P}+\mathbf{P}^*\,] \ . \quad (6.1.7)$$

Therefore, the complex nonlinear polarisation is

$$\mathbf{P} = \varepsilon_o \chi^{(2)} : \mathbf{E}_1\mathbf{E}_2 \ e^{i[(\mathbf{k}_1+\mathbf{k}_2)\cdot\mathbf{r}-(\omega_1+\omega_2)t]} \ . \quad (6.1.8)$$

As we can see, the nonlinear polarisation is now expressed in terms of the two component fields (at ω_1 and ω_2) making up the total field. At this stage, we introduce the standard notation for the quadratic nonlinearity, the nonlinear coefficient **d**, which is widely used by experimentalists and is defined through

$$\mathbf{P} = 2\varepsilon_o \mathbf{d}:\mathbf{E}_1\mathbf{E}_2 e^{i[(\mathbf{k}_1+\mathbf{k}_2)\cdot\mathbf{r}-(\omega_1+\omega_2)t]} \ . \quad (6.1.9)$$

Hence the relation between the nonlinear coefficient **d** and the nonlinear susceptibility $\chi^{(2)}$ is

$$\mathbf{d} = \frac{1}{2}\chi^{(2)} \quad . \tag{6.1.10}$$

Here, the factor of 2 introduced into the relationship between the polarisation and the field amplitudes results in the nonlinear polarisation at the sum frequency when written in component form being

$$\mathbf{P}_i = 2\varepsilon_o \, d_{ijk} \mathbf{E}_{1j} \, \mathbf{E}_{2k} \, e^{i[(k_1+k_2)\cdot r-(\omega_1+\omega_2)t]} \quad , \tag{6.1.11}$$

where i,j,k = x,y,z. And thus, in the case of SHG, because of the degeneracy of the fields, Eq. (6.1.11) becomes

$$\mathbf{P}_i(2\omega) = \varepsilon_o \, d_{ijk} \, \mathbf{E}_j \, \mathbf{E}_k \, e^{i(2k\cdot r-2\omega t)} \quad . \tag{6.1.12}$$

The Einstein summation convention is used in the last two equations.

When the second order nonlinear d-coefficient is expressed in component form, certain general symmetry relations can be applied in most practical situations to simplify Eq. (6.1.11) and Eq. (6.1.12). In the case of optically lossless and negligibly dispersive media, one symmetry relation, called Kleinman symmetry, is found to be extremely useful. Kleinman symmetry can be simply summarised as the independence of the ordering for all the subscripts of d_{ijk}, i.e.,

$$d_{ijk} = d_{jki} \quad , \tag{6.1.13}$$

and

$$d_{ijk} = d_{jik} \quad . \tag{6.1.14}$$

Because of the independent interchangeability of indices in Kleinman symmetry, then, by analogy with piezoelectric contraction, a similar contraction can be made over last two indices. The contraction rule is

jk	xx	yy	zz	yz, zy	xz, zx	xy, yx
l	1	2	3	4	5	6

The resulting d_{il} tensor forms a 3x6 matrix that operates on the $\mathbf{E}_1\mathbf{E}_2$ column vector to yield $\mathbf{P}$ according to

$$\begin{vmatrix} P_x \\ P_y \\ P_z \end{vmatrix} = \begin{vmatrix} d_{11} & d_{12} & d_{13} & d_{14} & d_{15} & d_{16} \\ d_{21} & d_{22} & d_{23} & d_{24} & d_{25} & d_{26} \\ d_{31} & d_{32} & d_{33} & d_{34} & d_{35} & d_{36} \end{vmatrix} \begin{vmatrix} 2E_{1x}E_{2x} \\ 2E_{1y}E_{2y} \\ 2E_{1z}E_{2z} \\ 2(E_{1y}E_{2z}+E_{1z}E_{2y}) \\ 2(E_{1z}E_{2x}+E_{1x}E_{2z}) \\ 2(E_{1x}E_{2y}+E_{1y}E_{2x}) \end{vmatrix} \tag{6.1.15}$$

When we restrict ourselves to the case of second harmonic generation, certain other symmetry properties occur due to the degeneracy between the two fields at ω_1 and ω_2, which are now the same field. In this case, from Eq. (6.1.12), we can write out the equation in matrix form as

$$\begin{vmatrix} P_x \\ P_y \\ P_z \end{vmatrix} = \begin{vmatrix} d_{11} & d_{12} & d_{13} & d_{14} & d_{15} & d_{16} \\ d_{21} & d_{22} & d_{23} & d_{24} & d_{25} & d_{26} \\ d_{31} & d_{32} & d_{33} & d_{34} & d_{35} & d_{36} \end{vmatrix} \begin{vmatrix} E_x^2 \\ E_y^2 \\ E_z^2 \\ 2E_yE_z \\ 2E_zE_x \\ 2E_xE_y \end{vmatrix} \quad . \quad (6.1.16)$$

This equation can be applied even in the absence of Kleinman symmetry because of the degeneracy between the fields at ω_1 and ω_2.

The number of nonzero components can be reduced further, however, by crystal symmetry considerations, and one can find a table of the d_{il} matrix forms for the different crystal classes in most of the nonlinear optics textbooks and reviews, see Ref. [1] and [3] for example. In the case of potassium niobate (single domain), which is a biaxial crystal and has a mm2 point-group symmetry [8], the d_{il} tensor is found to be of the form

$$d_{il} = \begin{vmatrix} 0 & 0 & 0 & 0 & d_{15} & 0 \\ 0 & 0 & 0 & d_{24} & 0 & 0 \\ d_{31} & d_{32} & d_{33} & 0 & 0 & 0 \end{vmatrix} \quad . \quad (6.1.17)$$

and this is true regardless of whether Kleinman symmetry applies or not. In the case when Kleinman symmetry does apply, Eq. (6.1.17) can be further reduced to:

$$d_{il} = \begin{vmatrix} 0 & 0 & 0 & 0 & d_{31} & 0 \\ 0 & 0 & 0 & d_{32} & 0 & 0 \\ d_{31} & d_{32} & d_{33} & 0 & 0 & 0 \end{vmatrix} \quad . \qquad (6.1.18)$$

The number of nonzero components reduces to 5 and the number of independent components is only 3.

6.2 Effective Nonlinear Coefficient

Once the crystal class, and hence the non-zero nonlinear coefficients, and the directions of polarisation of the interacting electro-magnetic waves are known, Eq. (6.1.11) and Eq. (6.1.12) can be further simplified by introducing a single scalar coefficient, d_{eff}, i.e.,

$$P(\omega_1+\omega_2) = 2\varepsilon_o \; d_{eff} \left|E_1(\omega_1)\right| \left|E_2(\omega_2)\right| \qquad (6.2.1a)$$

for sum frequency generation in general, and

$$P(2\omega) = \varepsilon_o \, d_{eff} \left|E(\omega)\right|^2 \qquad (6.2.1b)$$

for SHG in particular.

The coefficient, d_{eff}, is called the effective nonlinear coefficient. As we can see, there is a factor of 2 difference between these two equations as well. Although the factor 2 can be included in d_{eff} in the case of sum frequency generation as well as in the case of SHG, i.e. in Eq. (6.2.1b), we keep it separate here for the sake of consistency.

The advantage of Eq. (6.2.1) is that it reduces the quadratic nonlinear optical problem to one dimension in a mathematical sense, while maintaining the full three-dimensional aspect of the problem. A table of equations for d_{eff} for all the uniaxial crystal classes (all together there are 13 of them) is given in Ref. [1]. For biaxial crystal classes, however, it is too complicated to list d_{eff} under every situation. To demonstrate the evaluation of d_{eff} appropriate to SHG in a biaxial crystal, we choose the case of potassium niobate ($KNbO_3$) as an example, since this is the nonlinear material of relevance in this thesis.

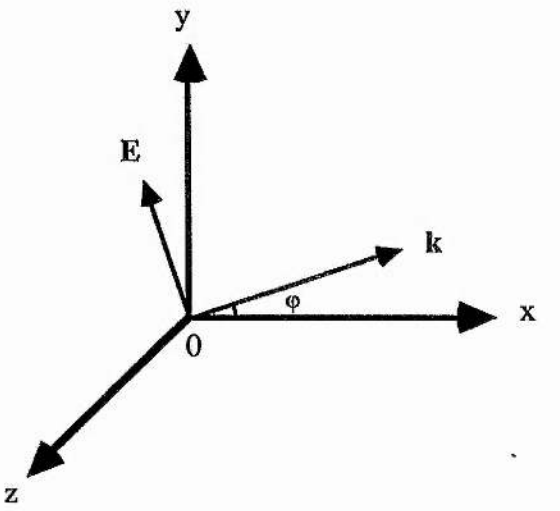

Figure 6.2.1 One of the Type-I phase matching situations for a fundamental wavelength of 946 nm in $KNbO_3$

A potassium niobate crystal has the orthorhombic structure (mm2 point-group symmetry) in the temperature range from -50 °c to 223 °c [8]. In one of the phase matching situations for SHG of 946-nm radiation, the beam propagates in the x-y plane with electric vector also in this plane as shown in Fig. 6.2.1. Thus the fundamental wave has components

$$E_x = E_0 \sin\varphi \quad ,$$

$$E_y = E_0 \cos\varphi \quad ,$$

$$E_z = 0 \quad , \qquad (6.2.2)$$

where φ is the azimuthal angle decided by phase matching condition.

The induced second harmonic polarisation along z-axis, according to Eq. (6.1.16) and Eq. (6.1.17), is

$$P(2\omega) = \varepsilon_o (d_{31} E_x^2 + d_{32} E_y^2) \ .$$

Substituting Eq. (6.2.2) into the last equation, we have

$$P(2\omega) = \varepsilon_o (d_{31} \sin^2\varphi + d_{32} \cos^2\varphi) E_o^2 \quad , \qquad (6.2.3)$$

hence the effective nonlinear coefficient is

$$d_{eff} = d_{31} \sin^2\varphi + d_{32} \cos^2\varphi \quad . \qquad (6.2.4)$$

The calculation of d_{eff} demonstrated so far has been very straight forward, and simple to understand. But when more terms are involved in d_{eff}, another standard way of calculating d_{eff} is preferable. In this case the **d** tensor coordinate axes are rotated so that one of the axes is coincident with the electric vector of the fundamental field and another axis is coincident with the second harmonic polarisation direction in which we are interested. This procedure is now described for the same case as illustrated in Fig. 6.2.1. We can see that the only rotation needed is about the z-axis counterclockwise by an angle of φ. The new coordinates will be denoted as x'y'z', see Fig. 6.2.2.

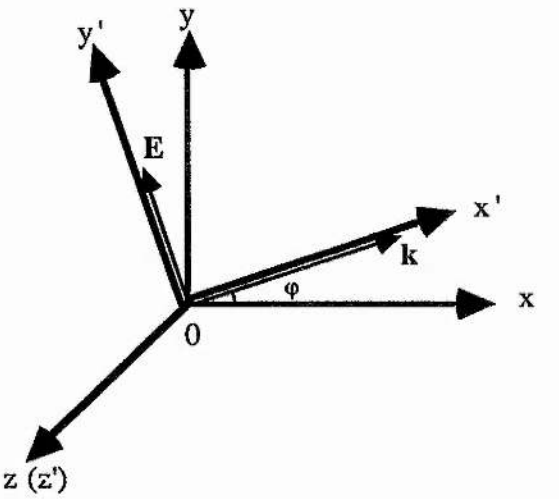

Figure 6.2.2 The polarisation vector and k-vector in the new coordinates

As shown in Fig. 6.2.2, the polarisation of the fundamental wave is along the y'-axis and the induced second harmonic polarisation component of interest is along the z(z')-axis. The effective nonlinear coefficient is then the d_{32}' component, i.e.,

$$d_{eff} = d'_{322} = a_{3i}\, a_{2j}\, a_{2k}\, d_{ijk} \quad , \tag{6.2.5}$$

where a_{ij} is a component of the rotation transform tensor. Substituting all the non-zero d-components, we get

$$\begin{aligned} d_{eff} = {} & a_{31}a_{23}a_{21}d_{131} + a_{32}a_{22}a_{23}d_{223} + a_{33}a_{21}a_{21}d_{311} \\ & + a_{31}a_{21}a_{23}d_{131} + a_{32}a_{23}a_{22}d_{223} + a_{33}a_{22}a_{22}d_{322} \\ & + a_{33}a_{23}a_{23}d_{333} \quad . \end{aligned} \tag{6.2.6}$$

Since we have

$$\mathbf{a} = \begin{vmatrix} a_{11} & a_{12} & a_{13} \\ a_{21} & a_{22} & a_{23} \\ a_{31} & a_{32} & a_{33} \end{vmatrix} = \begin{vmatrix} \cos\varphi & \sin\varphi & 0 \\ -\sin\varphi & \cos\varphi & 0 \\ 0 & 0 & 1 \end{vmatrix} , \qquad (6.2.7)$$

then, any terms in Eq. (6.2.6) having a_{ij} with 3 as one of the subscripts will be zero, apart from these with a_{33}. Eq. (6.2.6) becomes

$$\begin{aligned} d_{eff} &= a_{33}a_{21}a_{21}d_{31} + a_{33}a_{22}a_{22}d_{32} \\ &= d_{31}\sin^2\varphi + d_{32}\cos^2\varphi \quad , \end{aligned} \qquad (6.2.8)$$

which is exactly what we got in Eq. (6.2.4).

6.3 Optical Second Harmonic Generation

To give a general analytical description of nonlinear process, we need to see how the nonlinear polarisation (Eq. 6.1.11), which acts as a source term, is introduced into the fundamental electro-magnetic wave equations, i.e., Maxwell's equations,

$$\nabla \times \mathbf{H} = \mathbf{j} + \frac{\partial \mathbf{D}}{\partial t} = \mathbf{j} + \frac{\partial(\varepsilon \mathbf{E} + \mathbf{P}^{NL})}{\partial t} \quad , \qquad (6.3.1)$$

$$\nabla \times \mathbf{E} = -\frac{\partial(\mu_o \mathbf{H})}{\partial t} \quad . \qquad (6.3.2)$$

Here the linear polarisation is included in the dielectric constant ε and we

assume the material is nonmagnetic, that is,

$$\mathbf{B} = \mu_o(\mathbf{H}+\mathbf{M}) = \mu_o \mathbf{H} \quad .$$

If the medium is lossless, the term in $\mathbf{j}$ can be taken as zero in Eq. (6.3.1), which then becomes

$$\nabla \times \mathbf{H} = \frac{\partial(\varepsilon \mathbf{E} + \mathbf{P}^{NL})}{\partial t} \quad . \tag{6.3.3}$$

Taking the curl of both sides of Eq. (6.3.2) and substituting Eq. (6.3.3), we obtain

$$\nabla \times \nabla \times \mathbf{E} = -\mu_o \left(\varepsilon \frac{\partial^2 \mathbf{E}}{\partial t^2} + \frac{\partial^2 \mathbf{P}^{NL}}{\partial t^2} \right) \quad . \tag{6.3.4}$$

As

$$\nabla \times \nabla \times \mathbf{E} = \nabla \nabla \cdot \mathbf{E} - \nabla^2 \mathbf{E} \quad ,$$

and

$$\nabla \cdot \mathbf{E} \approx 0$$

(no free charge) is usually true, we finally get

$$\nabla^2 \mathbf{E} = \mu_o \, \varepsilon \frac{\partial^2 \mathbf{E}}{\partial t^2} + \mu_o \frac{\partial^2 \mathbf{P}^{NL}}{\partial t^2} \quad . \tag{6.3.5}$$

As described in Section 6.1, the general nonlinear process using the quadratic nonlinearity is a three-wave mixing process. So, without losing any generality, we limit the consideration to an electric field having three

frequency components, ω_1, ω_2 and $\omega_3=\omega_1+\omega_2$. Then the field can be described as

$$E(r,t) = \frac{1}{2}[\, E_1(r)\, e^{i(k_1\cdot r-\omega_1 t)} + E_2(r)\, e^{i(k_1\cdot r-\omega_2 t)} + E_3(r)\, e^{i(k_3\cdot r-\omega_3 t)} + c.c.\,] \quad . \tag{6.3.6}$$

Confining ourselves to a one-dimensional problem by assuming that these waves are all plane waves and propagating along the z direction, we can reduce Eq. (6.3.5) to

$$\frac{\partial^2 E(z,t)}{\partial z^2} = \mu_o\, \varepsilon \frac{\partial^2 E(z,t)}{\partial t^2} + \mu_o \frac{\partial^2 P^{NL}}{\partial t^2} \quad . \tag{6.3.7}$$

The three nonlinear polarisation components at ω_1, ω_2 and ω_3, according to the previous section, are

$$P_1^{NL}(z,t) = 2\varepsilon_o d_{eff} E_3(z) E_2^*(z) \exp[\, i(k_3-k_2)z - (\omega_3-\omega_2)t\,] \quad , \tag{6.3.8a}$$

$$P_2^{NL}(z,t) = 2\varepsilon_o d_{eff} E_3(z) E_1^*(z) \exp[\, i(k_3-k_1)z - (\omega_3-\omega_1)t\,] \quad , \tag{6.3.8b}$$

and

$$P_3^{NL}(z,t) = 2\varepsilon_o d_{eff} E_1(z) E_2(z) \exp[\, i(k_1+k_2)z - (\omega_1+\omega_2)t\,] \quad . \tag{6.3.8c}$$

Substituting Eq. (6.3.6) and Eq. (6.3.8) into the wave equation Eq. (6.3.7), and equating the terms with the same frequency on two sides, we arrive at a set of coupled amplitude equations:

$$\frac{dE_1}{dz} = - i \left(\frac{\omega_1}{n_1 c}\right) d_{eff} E_3 E_2^* \exp[\, i(k_3 - k_2 - k_1)z \,] \quad , \qquad (6.3.9a)$$

$$\frac{dE_2}{dz} = - i \left(\frac{\omega_2}{n_2 c}\right) d_{eff} E_3 E_1^* \exp[\, i(k_3 - k_1 - k_2)z \,] \quad , \qquad (6.3.9b)$$

$$\frac{dE_3}{dz} = - i \left(\frac{\omega_3}{n_3 c}\right) d_{eff} E_1 E_2 \exp[\, i(k_1 + k_2 - k_3)z \,] \quad , \qquad (6.3.9c)$$

where $c=1/(\varepsilon_o \mu_o)^{1/2}$ is the velocity of light in vacuum. In the derivation of Eqs. (6.3.9), the slowly varying amplitude approximation has been employed, which can be expressed as

$$\frac{d^2 E_i}{dz^2} \ll k_i \frac{dE_i}{dz} \quad .$$

From Eq. (6.3.9), we can see that an exchange of energy occurs between fields at different frequencies due to the optical nonlinearity of the material; the fields being coupled to each other by the effective nonlinear coefficient d_{eff}. We can simplify Eqs. (6.3.9) further by defining three new field variables A_i by

$$A_i = \sqrt{\frac{n_i}{\omega_i}}\, E_i \quad , \qquad i=1,2,3 \quad , \qquad (6.3.10)$$

so that the intensity at ω_i can be described in terms of A_i as

$$I_i = \frac{1}{2}\sqrt{\frac{\varepsilon_o}{\mu_o}}\, n_i \left|E_i\right|^2 = \frac{1}{2}\sqrt{\frac{\varepsilon_o}{\mu_o}}\, \omega_i \left|A_i\right|^2 \quad . \qquad (6.3.11)$$

Since the photon energy is $h\upsilon_i$, the quantity $|A_i|^2$ is proportional to the

photon flux at ω_i and is frequency independent. In terms of A_i, Eq. (6.3.9) becomes

$$\frac{dA_1}{dz} = -i\kappa A_3 A_2^* \exp[\, i\,\Delta k\, z] \quad , \tag{6.3.12a}$$

$$\frac{dA_2}{dz} = -i\kappa A_3 A_1^* \exp[\, i\,\Delta k\, z] \quad , \tag{6.3.12b}$$

$$\frac{dA_3}{dz} = -i\kappa A_1 A_2 \exp[\, -i\,\Delta k\, z] \quad , \tag{6.3.12c}$$

where

$$\Delta k = k_3 - (k_1 + k_2) \quad , \tag{6.3.13}$$

and

$$\kappa = \frac{d_{eff}}{c} \left(\frac{\omega_1 \omega_2 \omega_3}{n_1 n_2 n_3} \right)^{\frac{1}{2}} \quad . \tag{6.3.14}$$

It is obvious in Eq. (6.3.12) that the fields are now coupled through a single parameter κ. Multiplying both sides of Eq. (6.3.12a), Eq. (6.3.12b) and Eq. (6.3.12c) by A_1^*, A_2^*, and A_3^* respectively, and comparing them, we get

$$\frac{d|A_1|^2}{dz} = \frac{d|A_2|^2}{dz} = -\frac{d|A_3|^2}{dz} \quad , \tag{6.3.15}$$

which implies that one photon at ω_3 can create two photons of lower frequencies and vice versa. If Eqs. (6.3.15) are expressed in terms of photon number (by multiplying through out by $(\varepsilon_o/\mu_o)^{1/2}/2$), they are then known

as the Manley-Rowe relations.

In the case of second harmonic generation, we have $\omega_1=\omega_2=\omega$ and $\omega_3=2\omega$, so we can write

$$A_1(0) = A_2(0) = \frac{1}{\sqrt{2}} A_{tot}(0) \quad ,$$

where $A_{tot}(0)$ corresponds to the intial value of the fundamental field. From Eqs. (6.3.15), we have

$$\frac{d}{dz}(|A_1|^2 + |A_3|^2) = 0 \quad . \tag{6.3.16}$$

Applying the initial condition which assumed no input at ω_3, or 2ω, we get

$$|A_1|^2 + |A_3|^2 = \frac{1}{2}|A_{tot}(0)|^2 \quad , \tag{6.3.17}$$

and the differential equation for A_3 is

$$\frac{dA_3}{dz} = - i \kappa |A_1|^2 \exp(-i \Delta k z) \quad . \tag{6.3.18}$$

Substituting Eq. (6.3.17) into Eq. (6.3.18) gives

$$\frac{dA_3}{dz} = - i \kappa [\frac{1}{2}|A_{tot}^2(0)| - |A_3^2|] \exp(-i \Delta k z) \quad . \tag{6.3.19}$$

After rearrangement of Eq. (6.3.19), it becomes

$$\frac{d\left(\frac{A_3}{\frac{1}{\sqrt{2}}A_{tot}(0)}\right)}{\left[1-\left(\frac{A_3}{\frac{1}{\sqrt{2}}A_{tot}(0)}\right)^2\right]} = -i\kappa\left(\frac{A_{tot}}{\sqrt{2}}\right)\exp(-i\Delta k\, z)\, dz \quad . \qquad (6.3.20)$$

Integrating both sides of Eq. (6.3.20) and applying the initial condition $A_3|_{z=0} = 0$, we have

$$\operatorname{arctanh}\left(\frac{\sqrt{2}\,A_3(L)}{A_{tot}(0)}\right) = \kappa\left(\frac{A_{tot}}{\sqrt{2}}\right)\frac{\exp(-i\Delta k\, L) - 1}{\Delta k} \quad . \qquad (6.3.21)$$

And then the optical power conversion efficiency will be

$$\eta = \frac{P_{2\omega}}{P_{\omega}} = \frac{2\omega\left|A_3(L)\right|^2}{\omega\left|A_{tot}(0)\right|^2} = \tanh^2\left[\kappa\left(\frac{A_{tot}}{\sqrt{2}}\right)\frac{\exp(-i\Delta k\, L) - 1}{\Delta k}\right]. \qquad (6.3.22)$$

This is actually the second harmonic efficiency with a depleted input. In the case of small incident fields, Eq. (6.3.22) reduces to the low conversion efficiency approximation

$$\eta_0 = \kappa^2\frac{A_{tot}^2 L^2}{2}\frac{\sin^2(\Delta k\, L/2)}{(\Delta k\, L/2)^2}$$

$$= \frac{2\omega^2 d_{eff}^2 L^2}{\varepsilon_0 c^3 n_{\omega}^2 n_{2\omega}}\left(\frac{P}{Area}\right)\operatorname{sinc}^2(\Delta k\, L/2) \quad , \qquad (6.3.23)$$

which can be found in nearly all the literature about SHG.

So, the conversion efficiency with depletion, Eq. (6.3.22), can be expressed in terms of the conversion efficiency without depletion in the form of

$$\eta = \tanh^2(\sqrt{\eta_0}) \quad . \tag{6.3.24}$$

Conversion efficiency as given by Eq. (6.3.24) is derived for a plane wave geometry, but as an approximation it can also be used for other geometries, such as Gaussian beams, especially in the case of high conversion efficiency. Since η in Eq. (6.3.24) is a monotonically increasing function of η_0, when the input power and the crystal length are fixed, the maximization of η now reduces to the maximization of the value of η_0.

The optimization of SHG conversion efficiency η_0 (i.e., in the absence of depletion effects) involving a focused fundamental beam has been analysed by Boyd and Kleinman [10]. Here, some of the results will be summarised and discussed.

The Gaussian mode electric field with beam waist w_0 is described by

$$E(x,y,z) = E_0 \frac{w_0}{w(z)} \exp[\, i(kz - \varphi) - r^2\left(\frac{1}{w^2(z)} + \frac{ik}{R(z)}\right)\,] \quad , \tag{6.3.25}$$

where

$$\varphi = \tan^{-1}\left(\frac{\lambda z}{\pi w_0^2}\right)$$

is the phase factor which represents the additional phase shift to be added

to the usual plane wave phase shift; w(z) and R(z) are the beam waist and the radius of wavefront curvature respectively, and they are given by

$$w^2(z) = w_0^2 \left[1 + \left(\frac{2z}{b}\right)^2 \right] \quad ,$$

and

$$R(z) = z \left[1 + \left(\frac{b}{2z}\right)^2 \right] \quad ,$$

where $b\ (=w_0^2 k)$ is the confocal parameter describing the Gaussian beam. The parameters k, w, R and b are all within the crystal.

To characterise the nonlinear interaction, two parameters are defined. They are the focusing parameter

$$\xi = \frac{L}{b} \quad , \tag{6.3.26}$$

and the walk-off parameter

$$B = \frac{1}{2} \rho \left(L k_\omega \right)^{\frac{1}{2}} \quad , \tag{6.3.27}$$

where L is the crystal length, ρ is the walk-off angle of SHG due to the double refraction of materials, and k_ω is the fundamental wave vector.

Under the assumption of negligible absorption in the crystal at both fundamental and SHG wavelengths, and the assumption of the central location of the beam waist in the crystal, the SHG conversion efficiency at optimum phase match, is expressed by

$$\eta_0 = \left(\frac{2\,\omega^2\,d_{eff}^2}{\pi\,n_\omega^2\,n_{2\omega}\,\varepsilon_o\,c^3}\right) P_\omega\,L\,k_\omega\,h(B,\xi) \quad , \tag{6.3.28}$$

where n_ω and $n_{2\omega}$ are the refractive indices for the fundamental and the second harmonic respectively, and the reduction factor $h(B,\xi)$ is determined numerically. Fig. 6.3.1 shows curves of $h(B,\xi)$ as a function of ξ with B as a parameter. A maximum value of 1.068 can be obtained for $h(B,\xi)$ when

$$\xi = \xi_m = 2.84 \quad , \tag{6.3.29a}$$

and

$$B = 0 \quad . \tag{6.3.29b}$$

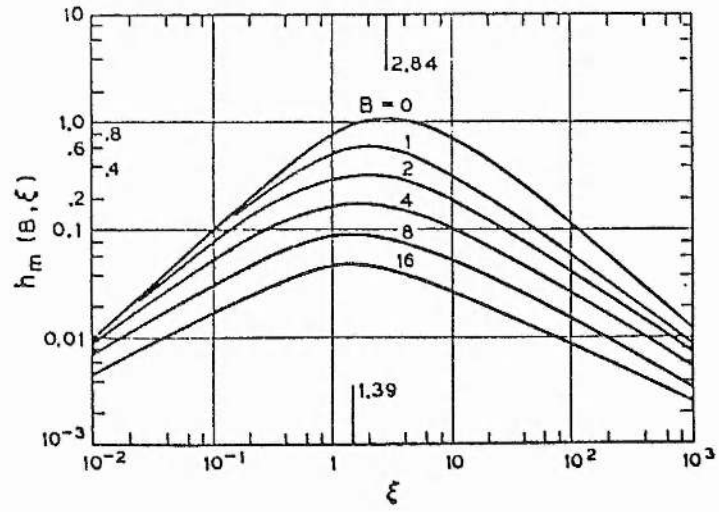

Figure 6.3.1 The reduction factor $h(B,\xi)$ as a function of ξ with as parameter (Ref. [10])

From Fig. 6.3.1, we can see that around the optimum, $h(B,\xi)$ is only a slowly varying function of ξ, so choice of ξ is not too critical. In practice, we can achieve the optimum condition of Eq. (6.3.29) by a non-critical phase

matching set-up (see next section) and suitable choices of crystal length and focal length of focusing lens.

6.4 Phase Matching Using Birefringence

In the previous sections of this chapter, we have noticed that the induced second harmonic power, or the conversion efficiency, is closely related to the value of Δk. There will always be an optimum value for Δk corresponding to each particular case. A plane wave geometry gives the generated electromagnetic wave a "sinc" type function (see Eq. (6.3.23)), and reaches its maximum conversion efficiency when

$$\Delta k = 0 \quad . \tag{6.4.1}$$

When a focused Gaussian wave geometry is considered, the optimum Δk-value no longer occurs at $\Delta k = 0$, and the stronger the beam is focused, the larger is the deviation of Δk from zero. In practice, however, this deviation is very small and is easily tuned experimentally by a fine adjustment of the crystal orientation or crystal temperature once the $\Delta k = 0$ position has been found. The requirement of Eq. (6.4.1) is normally referred to as phase matching condition.

In the case of collinear SHG with plane waves, the phase matching condition Eq. (6.4.1) gives

$$k_{2\omega} = 2\, k_{\omega} \quad , \tag{6.4.2}$$

which corresponds to

$$n_{2\omega} = n_{\omega} \quad , \tag{6.4.3}$$

as

$$k_{\omega} = \omega\, n_{\omega}/c \quad .$$

So sometimes phase matching is also referred to as index matching.

In order to satisfy the requirement $n_{2\omega} = n_{\omega}$, one technique which takes advantage of the natural birefringence of anisotropic crystals has been widely used. The crystal anisotropic character can be described through the index ellipsoid

$$\frac{x^2}{n_{x0}^2} + \frac{y^2}{n_{y0}^2} + \frac{z^2}{n_{z0}^2} = 1 \quad , \tag{6.4.4}$$

where x, y, z are the principal dielectric axes of the material and n_{x0}, n_{y0}, n_{z0} are the principal refractive indices respectively. The magnitudes of x, y, z are related to the electric displacement **D** by

$$x = \frac{D_x}{\sqrt{2\,\varepsilon_o W_e}} \quad ,$$

$$y = \frac{D_y}{\sqrt{2\,\varepsilon_o W_e}} \quad , \tag{6.4.5}$$

$$z = \frac{D_z}{\sqrt{2\,\varepsilon_o W_e}} \quad .$$

Here, D_i, i=x, y, z, are the electric displacements along the x, y, z axes

respectively; and W_e is the stored electric energy density in the medium. Eqs. (6.4.5) reminds us that the index ellipsoid is constructed in **D**-space rather than **E**-space. This is appropriate to our present analysis since we wish to define the propagation of an electromagnetic field in the first instance in terms of its **k** vector, and the **k** vector is orthogonal to the corresponding **D** vector. In general, the direction of the wave vector, **k**, is not the same as the ray direction (Poynting vector direction), which is known as the Poynting vector walk-off effect. It causes the polarisation wave and the generated electromagnetic wave (type-I) or two orthogonal polarised polarisation waves (type-II) to separate spatially. The **E** field is orthogonal to the ray direction, and it is possible to define an alternative ellipsoid in terms of electric fields and ray directions.

The procedure for finding the polarisation directions and the corresponding refractive indices for a given direction of propagation is as follows: Determine the ellipse formed by the intersection of a plane through the origin and normal to the direction of propagation (**k**) and the index ellipsoid Eq. (6.4.4). The directions of the major and minor axes of this ellipse are those of the two allowed polarisations and the lengths of these axes are $2n_{max}$ and $2n_{min}$, where n_{max} and n_{min} are the indices of refraction of the two allowed solutions of Eq. (6.4.4). For a further discussion of the ellipsoid of wave normals and its use see Ref. [2].

The exact expression for the phase matching direction differs from one case to another. It depends not only on the nature of the crystal, i.e., uniaxial or biaxial, positive or negative, but also on the type of phase matching, that is, Type-I or Type-II. In Type-I phase matching, there is only one eigenvector in the fundamental whilst in Type-II, there are two eigenvectors in the fundamental.

In the case of $KNbO_3$, the crystal is biaxial and classified as an orthorhombic crystal with mm2 point-group symmetry, the natural crystallographic axes a, b, c thus are mutually perpendicular. The assignments of a, b, c can be very different from one case to another, largely depending on the symmetry of the crystal concerned. For an orthorhombic mm2 crystal, the c-axis is usually chosen as the single diad axis of that material, and the a-axis and b-axis are chosen to be the two perpendiculars to the corresponding symmetry planes with unit cell dimensions $a_0<b_0$. In studies of the electric and elastic properties of crystals a set of rectangular axes are invariably adopted, and it is fortunate that in this case the natural crystallographic axes themselves are mutually perpendicular so that the set of rectangular axes X, Y, Z, often referred to as the piezoelectric axes, can be related to the crystallographic axes easily. The following convention for orthorhombic mm2 crystals are then adopted universally, namely, "X along a, Y along b, and Z along c" [13,14].

In Eq. (6.4.4), we introduced the principal dielectric axes x, y, z, which are essential to the definition of the ellipsoid of wave normals and hence the derivation of effective refractive indices in anisotropic medium. The principal dielectric axes are always orthogonal to each other and their orientation is determined by the symmetry properties of the crystalline material. In this respect they are more closely related to the piezoelectric axes X, Y, Z, than the crystallographic axes which are not always orthogonal. The principal dielectric axes and the piezoelectric axes are always fixed parallel to each other in the orthorhombic system, but the association of one particular dielectric axis with one particular piezoelectric axis is to some extent arbitrary. In order to have an unambiguous set of principal dielectric axes, the relation $n_{z0} > n_{y0} > n_{x0}$ [13,15] are often adopted, where n_{x0}, n_{y0} and n_{z0} are the principal

refractive indices.

The second order polarizability in the case of second harmonic generation has the same symmetry properties as the piezoelectric tensor, so nonlinear axes (1, 2, 3) can be readily related to the piezoelectric axes (X, Y, Z).

The conventions summarised above are relatively easy to follow. However, in early experiments [16], the structure of $KNbO_3$ at room temperature was shown to be strictly isomorphous with orthorhombic $BaTiO_3$, and the crystallographic axes a, b, c of $KNbO_3$ defined then were such that the c-axis was taken to coincide with the diad axis and the unit cell dimension a_0, instead of being shorter than b_0 as the convention requires, was taken to be larger than the unit cell dimension b_0. Further confusion has also arisen from the transformation between the piezoelectric axes X, Y, Z and the principal dielectric axes x, y, z. Though the criteria of $n_{z0} > n_{y0} > n_{x0}$ have been widely adopted, some people still use their own definitions (e.g. in Ref. [17]).

Because of discrepancies in the literature it is important to be specific about the conventions adopted in a particular analysis. The conventions adopted here are summarised in Table 6.4.1. We have retained the original convention first used by Katz & Megaw for defining the crystallographic axes (this differs from the standard convention of making $a_0<b_0$ discussed above). We have associated the piezoelectric axes and **d**-tensor axes with the crystallographic axes following the normal conventions. We have further chosen to define the principal refractive indices in terms of the crystallographic axes rather than introduce a fourth set of axes, the dielectric axes. In this case, it is important to note that we then have

$n_b > n_a > n_c$, which provides a useful test of our convention compared to conventions of other authors.

Table 6.4.1 Axis conventions for $KNbO_3$

Crystallographic axes	a (a_0=5.697 Å)	b (b_0=3.971Å)	c (c_0=5.720 Å)
Piezoelectric axes	X	Y	Z
d-tensor axes	1	2	3
Dielectric axes	n_a	n_b	n_c
	$n_b > n_a > n_c$		

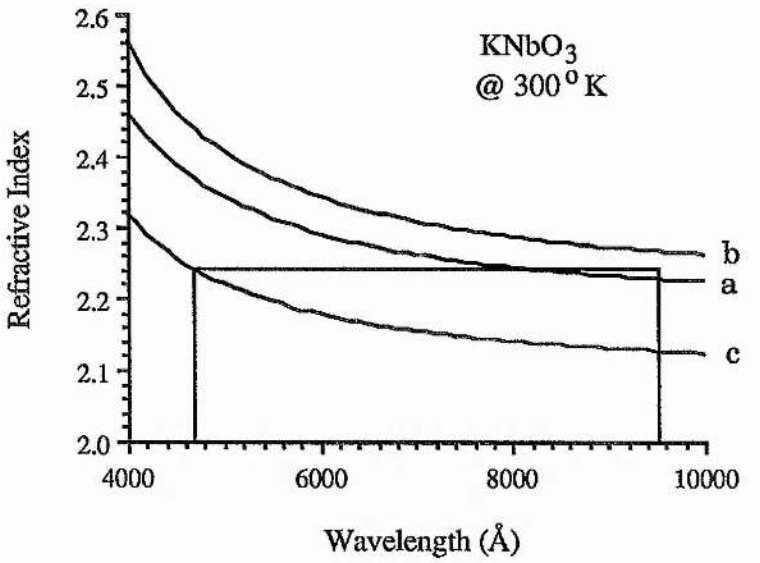

Figure 6.4.1 Dispersion of refractive indices in orthorhombic $KNbO_3$ at room temperature

Referring to the refractive index dispersion of $KNbO_3$ shown in Fig. 6.4.1, a Type-I matching condition can be achieved by angle tuning in the

a-b plane as long as the fundamental wavelength satisfies

$$n_b(\lambda) > n_c(\lambda/2) > n_a(\lambda) \quad . \tag{6.4.6}$$

The phase matching angle φ_{pm} in the a-b plane from the a-axis is

$$\sin\varphi_{pm} = \frac{n_a(\lambda)}{n_c(\frac{\lambda}{2})} \left[\frac{n_b^2(\lambda) - n_c^2\left(\frac{\lambda}{2}\right)}{n_b^2(\lambda) - n_a^2(\lambda)} \right]^{\frac{1}{2}} \quad . \tag{6.4.7}$$

An alternative Type-I phase matching geometry is when the angle tuning is performed in the a-c axes plane. Now, the fundamental light is polarised along the b-axis and the second harmonic light is polarised in the a-c plane. The phase matchable wavelength range is determined by

$$n_a\left(\frac{\lambda}{2}\right) > n_b(\lambda) > n_c\left(\frac{\lambda}{2}\right) \quad , \tag{6.4.8}$$

and the phase matching angle θ_{pm} in the a-c plane from c-axis is

$$\sin\theta_{pm} = \frac{n_c(\frac{\lambda}{2})}{n_b(\lambda)} \left[\frac{n_a^2\left(\frac{\lambda}{2}\right) - n_b^2(\lambda)}{n_a^2\left(\frac{\lambda}{2}\right) - n_c^2\left(\frac{\lambda}{2}\right)} \right]^{\frac{1}{2}} \quad . \tag{6.4.9}$$

If φ_{pm} or θ_{pm} become 90 ° or 0 °, then, a condition called "noncritical phase matching" is achieved. For thermally sensitive crystals, this noncritical phase matching condition can normally be satisfied by a method termed temperature tuning. In assessing a particular phase matching geometry, acceptance angle, temperature tuning width when appropriate, and

Poynting vector walk-off effects must be calculated. The acceptance angle is defined as the angle of tilt away from the phase match angle θ_{pm} or φ_{pm} at which the crystal length, L, is equal to the coherence length, l_c, which is defined as

$$l_c = \frac{\pi}{\Delta k} = \frac{\pi}{2k_\omega - k_{2\omega}} \quad ,$$

or

$$l_c = \frac{\lambda_1}{4} \frac{1}{n_\omega - n_{2\omega}} \quad , \qquad (6.4.10)$$

where λ_1 is the fundamental wavelength in vacuum. It corresponds to the SHG efficiency falling to 40.5% ($(2/\pi)^2$) of its on-axis value.

To expand $n(\theta,\varphi)$ about the phase matching angle, we get

$$n(\theta,\varphi) = n(\theta_{pm}, \varphi_{pm}) + \frac{\partial n}{\partial \theta}\Big|_{\substack{\theta=\theta_{pm} \\ \varphi=\varphi_{pm}}} \Delta\theta + \frac{\partial n}{\partial \varphi}\Big|_{\substack{\theta=\theta_{pm} \\ \varphi=\varphi_{pm}}} \Delta\varphi \quad , \qquad (6.4.11)$$

so the acceptance angle, as defined above, is

$$\Delta\theta_c = \frac{\lambda_1}{4L}\left[\frac{\partial n}{\partial \theta}\Big|_{\substack{\theta=\theta_{pm} \\ \varphi=\varphi_{pm}}}\right]^{-1} \qquad (6.4.12)$$

in one plane, and

$$\Delta\varphi_c = \frac{\lambda_1}{4L}\left[\frac{\partial n}{\partial \varphi}\Big|_{\substack{\theta=\theta_{pm} \\ \varphi=\varphi_{pm}}}\right]^{-1} \qquad (6.4.13)$$

in the other orthogonal plane. For uniaxial crystals, the last two equations reduce to a single equation.

Accordingly, the temperature width in the case of temperature tuning can be defined as the temperature departure from the phase match temperature in the same fashion as the acceptance angle. In analogy with Eqs. (6.4.12) and (6.4.13), we can derive the temperature tuning in the form of

$$\Delta T = \frac{\lambda_1}{4L} \left[\left| \frac{\partial n_\omega}{\partial T} - \frac{\partial n_{2\omega}}{\partial T} \right|_{T=T_{pm}} \right]^{-1} \quad . \tag{6.4.14}$$

To derive an expression for the Poynting vector walk-off angle in general, we rewrite the index ellipsoid Eq. (6.4.4) as

$$F(x,y,z) = \frac{x^2}{n_{x0}^2} + \frac{y^2}{n_{y0}^2} + \frac{z^2}{n_{z0}^2} - 1 = 0 \quad . \tag{6.4.15}$$

The Poynting vector direction is given by the normal direction to the ellipsoid surface at the phase matching point ($x=n_x$, $y=n_y$ and $z=n_z$) and hence the unit vector has components

$$\frac{1}{\sqrt{\left(\frac{\partial F}{\partial x}\right)^{-2}_{n_x n_y n_z} + \left(\frac{\partial F}{\partial y}\right)^{-2}_{n_x n_y n_z} + \left(\frac{\partial F}{\partial z}\right)^{-2}_{n_x n_y n_z}}} \left(\frac{\partial F}{\partial x}\right)^{-1}_{n_x n_y n_z} e_x \quad ,$$

$$\frac{1}{\sqrt{\left(\frac{\partial F}{\partial x}\right)^{-2}_{n_x n_y n_z} + \left(\frac{\partial F}{\partial y}\right)^{-2}_{n_x n_y n_z} + \left(\frac{\partial F}{\partial z}\right)^{-2}_{n_x n_y n_z}}} \left(\frac{\partial F}{\partial y}\right)^{-1}_{n_x n_y n_z} e_y \quad ,$$

$$\frac{1}{\sqrt{(\frac{\partial F}{\partial x})^{-2}_{n_x n_y n_z} + (\frac{\partial F}{\partial y})^{-2}_{n_x n_y n_z} + (\frac{\partial F}{\partial z})^{-2}_{n_x n_y n_z}}} \; (\frac{\partial F}{\partial z})^{-1}_{n_x n_y n_z} \, \mathbf{e}_z \quad ,$$

in comparision with the components of wavenumber unit vector,

$$(\sin\theta_{pm}\cos\varphi_{pm}\mathbf{e}_x , \quad \sin\theta_{pm}\sin\varphi_{pm}\mathbf{e}_y , \quad \cos\theta_{pm}\mathbf{e}_z) \quad .$$

Under phase matching condition, we find the walk-off angle ρ to be

$$\rho = \arccos \{[(\sin\theta_{pm}\cos\varphi_{pm}(\frac{\partial F}{\partial x})^{-1}_{n_x n_y n_z} + \sin\theta_{pm}\sin\varphi_{pm}(\frac{\partial F}{\partial y})^{-1}_{n_x n_y n_z}$$

$$+ \cos\theta_{pm}(\frac{\partial F}{\partial z})^{-1}_{n_x n_y n_z}] \; / \sqrt{(\frac{\partial F}{\partial x})^{-2}_{n_x n_y n_z} + (\frac{\partial F}{\partial y})^{-2}_{n_x n_y n_z} + (\frac{\partial F}{\partial z})^{-2}_{n_x n_y n_z}} \; \} \quad .$$

(6.4.16)

6.5 Other Phase Matching Methods

In the last section, we have discussed the most universally employed phase matching situations achieved by making use of birefringence properties of anisotropic crystals. However, a variety of other schemes for the achievement of phase matching have been explored and discussed, such as matching in optically active media [18,19], matching using Faraday rotation [20] and matching assisted by phonons [21].

Apart from these, some other ideas suggested in the early sixties [26] have been demonstrated experimentally. One of these ideas uses the phase change on total internal reflection [27,28]. Both the fundamental and the

second harmonic are reflected between the top and the bottom surface of a slab of crystal. The angle of reflection is so chosen that the phase mismatch is compensated by the phase shift upon reflection. A more successful revival of these early proposals is the one employing a periodically inverted crystal geometry. The crystal $LiNbO_3$ has attracted quite a lot of interest recently, because of the well established crystal growing technology for this material, the comparatively low price, and most of all, the large nonlinear coefficient, d_{33}. Several techniques have been demonstrated in growing periodic ferroelectric domain structured $LiNbO_3$ crystals [29-31]. The quasi-phase- matching condition can be achieved by setting the domain thickness equal to the coherence length or an odd multiple of the coherence length, so that the difference in phase between the polarisation wave and the generated wave is π at the end of the domain, when they are in phase at the beginning of the domain. The change of d-coefficient sign of the next domain gives an additional phase jump of π to the generated wave to catch up with the polarisation wave. The linear optical properties of the crystal with periodic ferroelectric domains is unaffected by its structure. In practice, the domain thickness of crystal is made slightly less than an odd multiple of the coherence length, and the final quasi-phase-matching condition is fulfilled by angle tuning.

There has been growing interest recently in a phase matching schemes based on a Cerenkov radiation type configuration applicable to waveguides [22-25]. The waveguide works in the regime where the nonlinear polarisation in a waveguide travels with a phase velocity greater than that of a free wave at the same frequency in the substrate medium. Analogous to the classical Cerenkov radiation in particle physics, the nonlinear polarisation, then, becomes a source of Cerenkov radiation, and accordingly the Cerenkov radiation condition takes the form

$$\cos \alpha = \frac{v_{2\omega}}{v_{\omega\ eff}} = \frac{n_{\omega\ eff}}{n_{2\omega}} \quad , \qquad (6.5.1)$$

where α is the Cerenkov angle, v is the phase velocity, $n_{\omega\ eff}$ the effective refractive index for the fundamental in the waveguide which is a function of the waveguide thickness, and $n_{2\omega}$ the refractive index of the second harmonic radiation in the substrate. The most interesting feature of this SHG is that the phase matching is satisfied automatically as long as the effective refractive index for the guided fundamental due to the waveguide thickness variation is kept smaller than $n_{2\omega}$, the refractive index for the radiated SHG in the substrate.

References

[1] F. Zernike and J. E. Midwinter, *Applied Nonlinear Optics*, John Wiley & Sons, New York, (1973);

[2] M. Born and E. Wolf, *Principles of Optics*, Macmillan, New York, (1964);

[3] A. Yariv, *Quantum Electronics,* Wiley, 2nd Ed., New York, (1975);

[4] A. Yariv, *Optical Electronics* , CBS College, 3rd Ed., New York, (1985);

[5] F. A. Hopf and G. I. Stegeman, *Applied Classical Electrodynamics, Vol. II, Nonlinear Optics*, John Wiley & Sons, New York, (1986);

[6] D. A. Kleinman, "Nonlinear dielectric polarisation in optical media", *Phys. Rev.*, Vol. 126, No. 6, (1962) 1977;

[7] D. A. Kleinman, "Theory of second harmonic generation of light", *Phys. Rev.*, Vol. 128, No. 4, (1962) 1761;

[8] P. Gunter, "Electro-optical properties of KN_bO_3", Electro-Optical/Laser International ' 76 U.K., (1976) 121;

[9] Tsuguo Fukuda and Y. Uematsu, "Preparation of KN_bO_3 single crystal for optical applications", *Japanese J. Appl. Phys.*, Vol. 11, No. 2, (1972) 163;

[10] G. D. Boyd and D. A. Kleinman, "Parametric interaction of focused gaussian light beams", *J. Appl. Phys.*, Vol. 39, No. 8, (1968) 3597;

[11] M. H. Dunn, "Introduction to nonlinear optics", Lecture Handout, (1985);

[12] R. L. Byer, "Parametric oscillators and nonlinear materials", *Nonlinear Optics* , P. G. Harper, et al., Eds., Academic Press, (1977).

[13] M. V. Hobden, "Phase-matched second-harmonic generation in biaxial crystals", *J. Appl. Phys.*, Vol. 38, No. 11, (1967) 4365;

[14] Standards Committee,1949-1950, and Piezoelectric Crystals Committee, 1947-1950,

"Standards on piezoelectric crystals, 1949", *Proc. I.R.E.* , 1378;

[15] E. Wiesendanger, "Optical properties of $KNbO_3$", *Ferroelectrics* , Vol. 1, (1970) 141;

[16] L.Katz and H.D.Megaw, "The structure of potassium niobate at room temperature: the solution of a pseudosymmetric structure by Fourier methods", *Acta Cryst.* , Vol. 22, (1967) 639;

[17] P. Gunter, "Near-infrared noncritically phase-matched second-harmonic generation in $KNbO_3$", *Appl. Phys. Lett.* , Vol. 34, No. 10, (1979) 650;

[18] P. P. Bey and H. Rabin, "Coupled-wave solution of harmonic generation in an optically active medium", *Phys. Rev.*, Vol. 162, No. 3, (1967) 794;

[19] H. Rabin and P. P. Bey, "Phase matching in harmonic generation employing optical rotatory dispersion", *Phys. Rev.*, Vol. 156, No. 3, (1967) 1010;

[20] C. K. N. Patel and N. VanTran, "Phase-matched nonlinear interaction between circularly polarised waves", *Appl. Phys. Lett.*, Vol. 15, No. 6, (1969) 189;

[21] D. F. Nelson and M. Lax, "Double phase matching of acoustically induced optical harmonic generation", *Appl. Phys. Lett.*, Vol. 18, No. 1, (1971) 10;

[22] P. K. Tien, R. Ulrich, and R. J. Martin, "Optical second harmonic generation in form of coherent Cerenkov radiation from a thin-film waveguide", *Appl. Phys. Lett.*, Vol. 17, No. 10, (1970) 447;

[23] E. Mathieu, "Conditions for quasi Cerenkov radiation, generated by optical second harmonic polarisation in a nonlinear crystal", *J. Appl. Math. & Phys.*, Vol. 20, (1969) 433;

[24] K. Hano and K. Takagi, "Optical second harmonic generation by guided-radiation mode coupling in a thin-film optical-waveguide", *Mem. Kyushu Institute of Technology and Engineering*, Vol. 10, (1980) 27;

[25] G. Tohmon, K. Yamamoto, and T. Taniuchi, "Blue light source using guided-wave frequency doubler with a diode laser", *SPIE*, Vol. 898, *Miniature Optics and Lasers*,

(1988) 70;

[26] J. A. Armstrong, N. Bloembergen, J. Ducuing, and P. S. Pershan, "Interactions between light waves in a nonlinear dielectric", *Phys. Rev.*, Vol. 127, No. 6, (1962) 1918;

[27] A. Ashkin, G. D. Boyd, and D. A. Kleinman, "Phase-matched second-harmonic generation in KDP without double refraction", *Appl. Phys. Lett.*, Vol. 6, No. 9, (1965) 179;

[28] G. D. Boyd and C. K. N. Patel, "Enhancement of optical second-harmonic generation (SHG) by reflection phase matching in ZnS and GaAs", *Appl. Phys. Lett.*, Vol. 8, No. 12, (1966) 313;

[29] D. Feng, N. Ming, J. Hong, Y. Yang, J. Zhu, Z. Yang, and Y. Wang, "Enhancement of second-harmonic generation in $LiNbO_3$ crystals with periodic laminar ferroelectric domains", *Appl. Phys. Lett.*, Vol. 37, No. 7, (1980) 607;

[30] A. Feisst and P. Koidl, 'Current induced periodic ferroelectric domain structures in $LiNbO_3$ applied for efficient nonlinear optical frequency mixing", *Appl. Phys. Lett.*, Vol. 47, No. 11, (1985) 1125;

[31] P. W. Haycock and P. D. Townsend, " A method of poling $LiNbO_3$ and $LiTaO_3$ below Tc", *Appl. Phys. Lett.*, Vol. 48, No. 11, (1986) 698.

Chapter 7

Frequency Doubling of 946-nm Light

In this chapter, we will first evaluate some interesting nonlinear crystals which are considered to be suitable for frequency doubling the 946-nm laser output of our previously described Q-switched Nd:YAG laser. Evaluations are made for potassium titanyl phosphate (KTP), beta-barium borate (BBO), lithium niobate ($LiNbO_3$) and potassium niobate ($KNbO_3$) crystals. The favourable properties of potassium niobate, such as its high second order (nonlinear) coefficient and potential for noncritical phase matching at the wavelength of interest, made it the final choice for our application. In section 7.2, we therefore discuss the physical properties of $KNbO_3$, especially its stress and temperature related depoling effects. With a 5-mm long $KNbO_3$ single crystal, we built a 22-W peak power all-solid-state blue laser. The experimental details will be described in section 7.3.

7.1 Nonlinear Crystals

With more and more nonlinear materials being discovered and synthetically grown, precise comparisons must be made amongst them in order to identify the best option for a particular application. The simultaneous requirements for transparency at the wavelengths of interest, optical quality, high effective nonlinear coefficient, and phase matching have limited the number of potentially useful nonlinear materials to a few out of the known selection of over 12,000 crystals. Further

restrictions on crystal choice are added if the laser has high average power and broad bandwidth. The key issues of material selection for frequency conversion can thus be summarised as:

(1) high conversion efficiency;

(2) high damage threshold;

(3) wide phase matching and transparency ranges;

(4) large size with good optical homogeneity;

(5) low cost and ease of fabrication; and

(6) chemical stability and insensitivity to moisture (non-hygroscopic).

It has been found that certain materials have larger nonlinearities than others. For a crystalline material to exhibit a second order optical nonlinearity, it must belong to a non-centro-symmetric crystal class. In addition to this, Miller propounded an useful empirical rule that the material should have a high refractive index if its nonlinearity is to be high [1]. The most familiar class having some of the largest nonlinear bond polarisabilities and some of the largest nonlinear coefficients is the oxygen-octahedra ferroelectrics containing Nb-O, Ti-O, or I-O bonds, such as $LiNbO_3$, $KNbO_3$, $Ba_2NaNb_5O_{15}$, $KTiOPO_4$, $LiIO_3$ and HIO_3 etc.. Recent researches on borate crystals showed that the planar structure of $(B_3O_6)^{-3}$ in boron-oxygen (B-O) compounds might provide high nonlinear effects [2]. New types of UV SHG crystals were thus developed, such as beta-barium borate (BBO) and lithium triborate (LBO).

In this section, we choose potassium titanyl phosphate (KTP), beta-barium borate (BBO), lithium niobate and potassium niobate as the candidates for second harmonic generation of the 946-nm wave. All these materials have relatively high optical nonlinear coefficients, in addition,

however, we should also consider other factors, such as (1) low absorption for both the fundamentals and harmonics, (2) large acceptance width for angle, spectrum, and temperature, and (3) large aperture length or small walk-off angle.

7.1.1 Potassium titanyl phosphate ($KTiOPO_4$)

Potassium titanyl phosphate (KTP) belongs to the orthorhombic point group mm2. Its lattice parameters are a= 1.2814 nm, b=0.6404 nm, and c=1.0616 nm and each unit cell contains eight formula units [3]. The structure is characterised by chains of TiO_6 octahedra which are linked at two corners and separated by PO_4 tetrahedra [3]. Alternating long and short Ti-O bonds occur along these chains that result in a net z-directed polarisation and are the major contributor to KTP's large nonlinear optical and electrooptic coefficients.

KTP is a widely used material for frequency doubling Nd:YAG lasers at 1.064 μm, and is also considered to be one of the most attractive material for various sum and difference frequency and optical parametric applications over its entire transparency range from 0.35 to 4.5 μm. The damage threshold of 15 GW/cm^2 in flux-grown KTP was reported for single 1-ns pulse at 1.064 μm [4], and the damage threshold in hydrothermally-grown KTP is expected to be even higher [3]. Table 7.1.1 lists the nonlinear optical coefficients of KTP.

Table 7.1.1 Nonlinear optical coefficients of KTP
(pm/V)

d_{31}	d_{32}	d_{33}	d_{24} [5]	d_{15} [5]
6.5	5.0	13.7	7.6	6.1

KTP crystals have been successfully grown by two methods, i.e., hydrothermal and flux techniques. Material grown by one technique shows slight differences in linear optical properties characterised by the Sellmeier equations compared to other [4,6]. The Sellmeier equations can be written in the form of

$$n^2 = A + \frac{B}{1 - C/\lambda^2} - D\lambda^2 \quad , \qquad (7.1.1)$$

where A, B, C and D are constant parameters, and λ is the vacuum wavelength in units of microns. The constant parameters in Eq. (7.1.1) are given for both flux-grown and hydrothermally-grown KTP in Table 7.1.2, the latter are enclosed in brackets.

Table 7.1.2 Sellmeier equation parameters for KTP

	A	B	C	D
n_x	2.16747 (2.1146)	0.83733 (0.89188)	0.04611 (0.04352)	0.01713 (0.01320)
n_y	2.19229 (2.1518)	0.83547 (0.87862)	0.04970 (0.04753)	0.01621 (0.01327)
n_z	2.25411 (2.3136)	1.06543 (1.00012)	0.05486 (0.05679)	0.02140 (0.01679)

Table 7.1.3 Principal refractive indices of KTP
@ 946 nm and 473 nm

	946 nm	473 nm
n_x	1.742 (1.744)	1.794 (1.794)
n_y	1.750 (1.752)	1.806 (1.807)
n_z	1.836 (1.835)	1.913 (1.911)

For the 946 nm wavelength and its SHG, the three principle refractive indices are shown in Table 7.1.3, in which the indices in the brackets are for the hydrothermally-grown KTP.

Studies of SHG at a fundamental wavelength of 1.064 μm indicates that KTP crystals perform most effectively when they are Type-II phase matched. However, for a fundamental wavelength of 946 nm, the Type-II phase match condition, i.e.,

$$\frac{1}{2}[\, n_z(\omega) + n_x(\omega)\,] > n_x(2\omega) \quad , \tag{7.1.2}$$

cannot be satisfied. The Sellmeier fit to the refractive index of the flux grown KTP crystal indicates that the shortest wavelength for Type-II SHG is 0.993 μm. The only choice left for 946nm wavelength is thus the Type-I phase match. Under the conditions of a large difference between n_z and n_x or n_y and a small difference between n_x and n_y, see Table 7.1.3, the allowed polarisation of the second harmonic radiation can be taken to be parallel to the x-y plane, and the polarisation of the fundamental to be mutually perpendicular to the direction of propagation and the polarisation of the second harmonic. The effective nonlinear coefficient in Type-I phase matching case can then be simplified to [7]

$$d_{eff} \approx \frac{1}{2}(\, d_{15} - d_{24}\,) \sin 2\theta \ \sin 2\phi \quad , \tag{7.1.3}$$

where θ is the angle relative to the z axis, and φ is the angle in the x-y plane relative to the x axis. In the case of $\phi = 45^o$, d_{eff} is maximised to

$$d_{eff} \approx \frac{1}{2}(\, d_{15} - d_{24}\,) \sin 2\theta \quad . \tag{7.1.4}$$

The phase matching angle of θ is calculated to be 53 ° for ϕ set at 45 °. The effective optical nonlinear coefficient given by Eq. (7.1.4) is only 0.72 pm/V. Applying Eq. (6.4.16) to the case here, we get the walk-off angle of 2.7 °. For comparison of crystals, the figure of merit describe by d_{eff}^2/n^3 is commonly adopted, and that for Type-I phase matched KTP crystal at 946 nm is 7.4×10^{-2} $(pm/V)^2$.

7.1.2 Beta-barium borate (β-BaB_2O_4)

Beta-barium borate (BBO) belongs to the trigonal system with point symmetry 3m. It has a wide transparency range between 190 nm and 3.5 μm. The high UV light transmission is believed to be mainly due to the large electro-negativity difference between boron and oxygen in the B-O bond [2]. It also has an extremely high damage threshold; 13.5 GW/cm^2 for 1-ns 1.064-μm pulses and of 7.0 GW/cm^2 for 532-nm pulses have been reported [8].

BBO is a negative uniaxial crystal with large birefringence and relatively small dispersion. The corresponding Sellmeier equation is given in the form of [8]

$$n^2 = A + \frac{B}{1 - C/\lambda^2} \quad , \tag{7.1.5}$$

where λ is the vacuum wavelength in units of microns, and A, B and C are parameters, whose values are given in Table 7.1.4.

Table 7.1.4 Sellmeier equation coefficients for BBO

	A	B	C
n_o	1.2365	1.4878	0.01451
n_e	- 0.3061	2.6622	0.00635

The refractive indices for ordinary and extraordinary beams at 946 nm and 473 nm can thus be calculated from Eq. (7.1.5), and they are listed below in Table 7.1.5.

Table 7.1.5 Refractive indices of BBO @ 946 nm and 473 nm

	946 nm	473 nm
n_o	1.6580	1.6815
n_e	1.5411	1.5601

In the case of Type-I phase maching in a negative uniaxial crystal, the phase mathing angle, θ_m, measured from the optic axis, can be obtained from

$$\sin^2\theta_m = \frac{(n_o^{\omega})^{-2} - (n_o^{2\omega})^{-2}}{(n_e^{2\omega})^{-2} - (n_o^{2\omega})^{-2}} \quad . \tag{7.1.6}$$

For BBO, the phase matching angle at 946 nm is 24.9 °, and the expression for the effective nonlinear optical coefficient is [8]

$$d_{eff} = d_{15} \sin\theta - d_{22} \sin 3\phi \cos\theta \quad , \tag{7.1.7}$$

where ϕ is the azimuthal angle. When a coordinate system with the y-axis parallel to a lattice mirror plane is used, the nonlinear optical coefficients obtained are d_{22} = 2.2 pm/V [9], and d_{15} =d_{31} = 0.07d_{22} [8]. Since d_{22} >> d_{15}, the way to maxmise the absolute value of d_{eff} in Eq. (7.1.7) is to set ϕ = 30° (or 90°). As an approxination, d_{eff} is simply d_{22} cosθ, and which is about 2 pm/V for the phase matching condition at 946 nm. The figure of merit then becomes 0.91 (pm/V)^2 in this case. The walk-off angle for phase matching at θ = 24.9 ° and ϕ = 30 ° is calculated to be 3.4 °. Such a large walk-off effect is caused by the large birefingence of this material.

7.1.3 Lithium niobate ($LiNbO_3$)

Lithium niobate ($LiNbO_3$) is one of the most well studied optical nonlinear crystals. It belongs to the trigonal point group, 3m, and is a negative uniaxial crystal. As such, there are only four nonzero coefficients, (d_{22}, d_{31}, d_{15}, and d_{33}) allowed for the nonlinear polarizability. By applying the Kleinman symmetry condition, we have d_{31} = d_{15}. The expression for the effective nonlinear coefficient is thus the same as Eq. (7.1.7), which gives d_{eff} for BBO. For $LiNbO_3$, however, d_{15} is about two times larger than d_{22} [10],so the maximum effective nonlinear coefficient,of value d_{15} is obtained by propagateing the beam in the x-y plane. For 5% MgO doped $LiNbO_3$, the effective nonlinear coefficient, d_{eff}, is 4.7 pm/V [9].

The doping of $LiNbO_3$ by magnesium oxide (MgO) has been found extremely advantageous. Pure $LiNbO_3$ crystals suffere from so-called refractive-index damage problem, which greatly limits the use of the crystal in many applications, especially those involving high power densities. Doping by MgO significantly increases the damage threshold,

and in addition, it is also used as a way to increase the noncritical phase matching temperature for some fundamental wavelengths. (For phase matching temperature greater than 180 °C, any index damage in the crystal anneals out instantaneously [11].) For a fundamental at 1.064 μm, an ideal congruent crystal has the noncritical phase matching temperature of -8 °C [11], and a 5% MgO doped one has the phase matching temperature of about 111 °C [9].

The refractive indices of $LiNbO_3$ crystal have been found to be very sensitive to composition and temperature. The mole ratio of Li/Nb in the melt can be varied from 0.8 to 1.2 without apparently altering the crystal quality [12]. Normally, the higher the lithium content of the melt, the higher the phase matching temperature. An elevated phase matching temperature can thus also be achieved by changing the composition ratio of the crystal. Because of this sensitivity of the refractive index to composition, it is difficult to have definite Sellmeier equations for $LiNbO_3$. For the evaluation purpose, we use the Sellmeier equations derived by Hobden and Warner for a stoichiometric crystal [13]. For the ordinary ray, the Sellmeier equation is

$$n_o^2 = 4.9130 + \frac{1.173\times10^5 + 1.65\times10^{-2}\,T^2}{\lambda^2 - (2.12\times10^2 + 2.7\times10^{-5}\,T^2)^2} - 2.78\times10^{-8}\,\lambda^2 \quad , (7.1.8)$$

and for the extraordinary ray, it is

$$n_e^2 = 4.5567 + 2.605\times10^{-7}\,T^2 + \frac{0.970\times10^5 + 2.70\times10^{-2}\,T^2}{\lambda^2 - (2.01\times10^2 + 5.4\times10^{-5}\,T^2)^2} - 2.24\times10^{-8}\,\lambda^2 \quad ,$$

(7.1.9)

where the temperature, T, is in degrees Kelvin and the wavelength, λ, is in nanometers (nm). In order to adjust the predictions of phase matching temperature given by the above equations to apply to some other composition, a good approximation formed to work in practice is to add to the predicted temperature from Eqs. (7.1.8) and (7.1.9), the value of the phase matching temperature difference known for some other wavelengths.

From the Sellmeier equations (Eqs. (7.1.8) and (7.1.9)), we conclude that $LiNbO_3$ cannot be phase matched for 946 nm at room temperature. Although, as discussed above, by changing the composition and doping MgO, it is possible to increase the phase matching temperature by the order of 100 °C, this is still too small to compensate for the impractically low phase matching temperature predicted at 946 nm.

In Section 6.5, we mentioned several other phase matching methods apart from the most commonly used phase matching technique employing the natural crystalline birefringences. One of them is called quasi-phase-matching (QPM), which uses a periodically poled ferroelectric crystal, in which the sign (domain) of the second-order nonlinear susceptibility is inverted with an appropriate spatial period determined by the coherence length. This technique has been successfully applied to $LiNbO_3$ [14-17]. In QPM, the nonlinear coefficient is modulated spatially with a period $\Lambda = 2ml_c$, where m=1, 3, 5, $\cdots$ is the order of QPM and l_c is the coherence length, given by Eq. (6.4.10), i.e.,

$$l_c = \frac{\lambda^{\omega}}{4\,(n^{\omega} - n^{2\omega})} \quad , \tag{7.1.10}$$

where λ^{ω} is the fundamental wavelength, and n^{ω} and $n^{2\omega}$ are the refractive indices at the fundmental and second harmonic wavelengths respectively. The effective nonlinear coefficient, d_{eff}, thus derived can be expressed by

$$d_{eff} = \frac{2}{m\pi} d_{ij} \quad , \tag{7.1.11}$$

where d_{ij} is the real nonlinear coefficient of the crystal. From Eq. (7.1.11), it is obvious that the lowest order QPM condition (m=1 and $\Lambda=2l_c$) is prefered in order to obtain the highest effective nonlinear coefficient. Nonuniformity of the periodicity significantly limits the effective interaction length and thus the conversion efficiency. So far, this uniformity has not been achieved over long enough lengths to make this material interesting in the context of the present application.

7.1.4 Potassium niobate ($KNbO_3$)

In chapter 6, potassium niobate was chosen to be our example to calculate phase matching angles, as well as to clarify the confusions among some frequently used sets of axes, i.e., the principal dielectric axes, the piezoelectric axes and the crystallographic axes. The attractiveness of $KNbO_3$ as a second-harmonic generator comparing with the above discussed crystals is its large optical nonlinear coefficients (d_{13} = 15.8 pm/V and d_{32} = 18.3 pm/V at λ = 1064 nm) and the possibility of noncritical phase matching in the range of 840 nm - 950 nm [18]. The corresponding temperature tuning range is between -40 °C and 200 °C, in which the $KNbO_3$ crystal belongs to the orthorhombic system with point group symmetry mm2. The crystal undergoes phase changes at about -50 °C, 223 °C and 418 °C [20].

The Sellmeier equations used for $KNbO_3$ have the form of [19]

$$n^2 - 1 = \frac{S_1 \lambda_1^2}{1 - (\lambda_1^2 / \lambda^2)} + \frac{S_2 \lambda_2^2}{1 - (\lambda_2^2 / \lambda^2)} \quad , \qquad (7.1.12)$$

where n is the refractive index at the wavelength λ (in m.); S_1, S_2, λ_1 and λ_2 are all experimentally fitted parameters, which represent the oscillator strengths and the oscillator positions respectively. At room temperature, the values of the Sellmeier constants are given in Table 7.1.6.

Table 7.1.6 Sellmeier equation coefficients for $KNbO_3$

	$S_1 \lambda_1^2$	λ_1^2 (10^{-20} m^2)	$S_2 \lambda_2^2$	λ_2^2 (10^{-20} m^2)
n_a	1.4392	5985156	2.3592	2302662
n_b	0.1362	11308698	3.8013	4087914
n_c	0.0875	10724149	3.3023	3130828

The dispersion curves given by Eq. 7.1.12 have already been plotted in Fig. 6.4.1. From such dispersion curves, it may be shown that $KNbO_3$ cannot be phase matched at wavelengths below 857 nm at room temperature. For Type-I phase matching, there are two possible angle tuning configurations, one is where the polarisation of the second harmonic wave is along the c-axis and beams propagate in the a-b plane (i.e., the phase matching angle from the c-axis, θ, is 90 °), and the other is where the polarisation of the fundamental wave is along the b-axis and beams propagate in the a-c plane (i.e., ϕ=0°). In practice, the first configuration is to be preferred to the second due to difficulties in preparing good optical quality crystals in the second phase matching configuration,

which will be discussed more in the next section.

At room temperature, phase matching can be achieved at any fundamental wavelengths between the two noncritical phase matching wavelengths 857 nm and 982 nm by using d_{32} (20.5 pm/V @ 857 nm) and d_{31} (16.4 pm/V @ 982 nm) respectively in the first phase matching configuration. The phase matching angle, ϕ, which is the angle from the a-axis, is given by Eq. (6.4.7). At the wavelength of 946 nm, ϕ is calculated to be 60.4 °, and Eq. (6.2.4) then gives the value of about 17.4 pm/V for the effective nonlinear optical coefficient. The walk-off angle, ρ, can be obtained by

$$\tan(\rho+\phi) = \left(\frac{n_a^{\omega}}{n_b^{\omega}}\right)^2 \tan\phi \quad , \qquad (7.1.13)$$

where n_a^{ω} and n_b^{ω} are the refractive indices at the fundamental wavelength. From the Sellmeier equation (Eq. (7.1.12)), n_a^{ω} and n_b^{ω} are found to be 2.2283 and 2.2669 respectively for a wavelength of 946 nm. The walk-off angle thus obtained at the phase matching angle, ϕ=60.4 °, is 0.85 °.

In addition to the large effective nonlinear coefficient and small walk-off angle in the angle tuning case, temperature tuned noncritical phase matching is another attraction of $KNbO_3$. It has been shown that the refractive indices, especially n_c, strongly depend on the temperature [18]. At about 185 °C, the two Type-I noncritical phase matching wavelengths 857 nm and 982 nm at room temperature move to 946 nm and 1064 nm, so any wavelengths between 857 nm and 946 nm, and between 982 nm and 1064 nm can be noncritical phase matched by adjusting the crystal temperature between room temperature and 185 °C and using nonlinear coefficients d_{32}

and d_{31} respectively. The relation between the noncritical phase matching wavelength and the temperature can be described by a second degree polynomial, which is

$$\lambda = a_0 + a_1 T + a_2 T^2 \quad , \tag{7.1.15}$$

where a_0, a_1 and a_2 are the experimentally fitted coefficients, and they are given in Table 7.1.7 [18].

Table 7.1.7 Coefficients for noncritical phase matching wavelength polynomial

d_{eff}	a_0 (nm)	a_1 (nm/°C)	a_2 (nm/°C^2)
d_{32}	850.40	0.294	1.234x10-3
d_{31}	976.04	0.253	1.146x10-3

7.2 Some Properties of Potassium Niobate

Despite the excellent linear and nonlinear optical properties of $KNbO_3$, such as the high optical nonlinear coefficients, and the noncritical phase matching geometries, there are problems with its practical utilisation. The most common problems associated with $KNbO_3$ crystal are crystal discolouration, cracking and depoling, and they are closely related to the conditions of crystal growth, such as the starting materials, the potassium to niobium ratio, the melt soak time and cooling rate etc.

It has been shown that optically pure crystals can be grown from melts comprised of niobium pentoxide (Nb_2O_5) and potassium oxide (K_2O) with favourable potassium to niobium ratio of somewhere between 1.105 to 1.273 [21]. The use of K_2CO_3 and Nb_2O_5 as the starting materials were also reported by other researchers [22-24]. It was found that cracking could be minimised by improving the thermal stability and axial uniformity during the cooling process and special care needed to be taken when the temperature passed through the tetragonal to orthorhombic phase change temperature, 225 °C. Provided the cooling rate did not exceed 3 °C/hr at this particular phase change temperature, an uniform phase change might be expected [21]. Below this temperature, the cooling rate can be increased to 20 °C/hr, but , whatever precautions may be taken during crystal growth, the as-grown crystals are normally multi-domain structured due to the unusual ferroelectric dipole mobility in $KNbO_3$. Multi-domain crystals are typically transparent when viewed perpendicular to the b-axis and flawed or cloudy when viewed along the b-axis, thus the final crystals purchased are normally polished on faces perpendicular to b-axis, through which they have been inspected.

In order to get single-domain crystals, the as-grown crystals should undergo a poling procedure, to align all the ferroelectric domains within a crystal into one common direction. An improved version of the usual poling technique has been suggested and successfully employed by Virgo Optics [21], in which the strong photoconducive effect in $KNbO_3$ is made use of by focusing an intense, broad band light beam into the $KNbO_3$ crystal. It was observed that, with the intense light shining on the crystal, the original poling voltage ranging from 1 to 10 KV/cm could be greatly reduced, as could the poling time. As the result of the reduced dc voltage across a

crystal during the poling process, the risk of surface discharging is reduced as well.

All the above mentioned precautions involved in the production of single $KNbO_3$ crystals remain important in the application stage. For SHG of 946-nm wave, the noncritical phase matching temperature of ~ 185 °C means that the crystal needs to be thermally cycled to that temperature repeatedly without causing any depoling problems.

Depolings are commonly caused by excessive thermal or mechanical stresses. $KNbO_3$ is least sensitive to the thermal depoling effect within the temperature range of 0 °C to 70 °C. Above 70 °C, more uniform heating and cooling are required in order to avoid partial or catastrophic depoling. By applying a dc voltage of the order 1 KV/cm along the c-axis of the crystal, the cycling time from room temperature to 180 °C can be shortened to 10 min [21]. In practical applications, however, such uniform heating and cooling are very difficult to realise. The thermal gradient in the crystal can be caused by three major factors. Firstly, the oven in the SHG application has a size much smaller than that used in crystal preparation; secondly, the oven normally does not have windows; and thirdly, it is impractical to heat or cool a crystal to the required temperature at such low rates. The first $KNbO_3$ crystal used in our experiment was mounted in a temperature controlled oven but without the electrical poling field. We found that the SHG power decreased every time it was used, which indicated that deterioration had occurred in the crystal. Looking through the crystal along the a-axis, we saw lines parallel to b-axis indicating an alteration of the refractive indices along the c-axis.

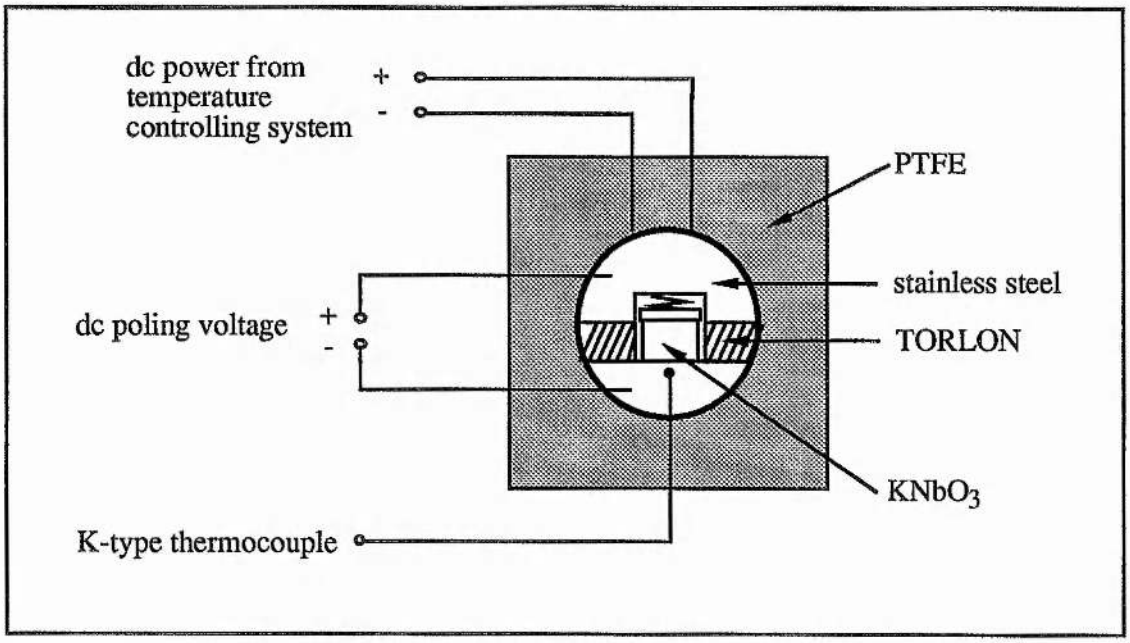

Figure 7.2.1 Oven structure

Subsequently, we built a modified temperature controlled oven with a facility for applying a poling field to the crystal, see Fig. 7.2.1. The two halves of the stainless-steel crystal housings were connected to a high-voltage power supply to provide a crystal poling electrical field. For depoling prevention, a voltage of around 100 V was used for a crystal of 3-mm thickness along the c-axis. Between the electrodes on each side of the crystal, TORLON was used as the electrical insulation material due to its superior mechanical and electrical properties. The resistive heating element was made from nickel wire with total length of 1.2 m and resistance of 10.4 Ω. The crystal was mounted with its a-axis colinear with the oven core axis, and with its c-axis along the electrical field formed by the metal housings. To avoid any excessive mechanical stresses, a spring loaded stainless steel plate contacted the crystal on one side. The oven core was thermally insulated by a PTFE housing. A k-type thermocouple embedded in the half housing on another side of the crystal was used for feedback to a temperature controller, which was a CAL 9000 module with a

proportional, integral and derivative (PID) type feedback circuit. The schematic of the whole temperature controlling unit is shown in Fig. 7.2.2.

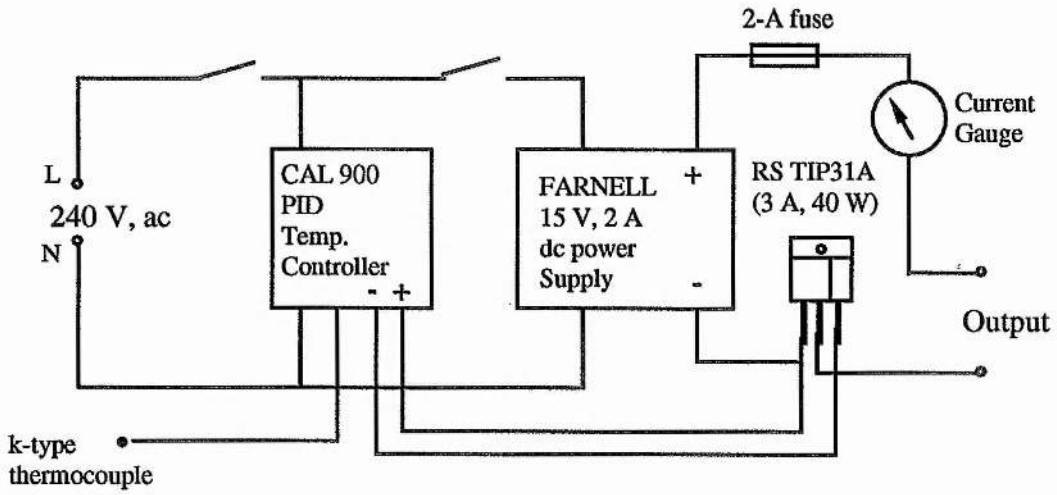

Figure 7.2.2 Temperature controlling system

Before mounting a crystal into the oven, it is necessary to know the polarities of the crystal. Usually, they are marked by manufacturers, but if they are not, the polarities can be determined by measuring the induced voltage across the faces normal to the c-axis when the crystal is being heated or cooled. During the heating-up period, the induced surface charge forms so as to produce an induced field in the same direction as the field required for poling, while during the cooling-down period, the induced field is opposite to the external poling field and it may be sufficient to depole the crystal in the absence of the external dc field, so it is more likely that catastrophic thermal depoling occurs in this period of the heating-cooling cycle.

7.3 Second Harmonic Generation in $KNbO_3$

The laser source used in these experiments was the diode laser pumped Q-switched 946-nm Nd:YAG laser, which we have described in the chapter 5. The high non-linear coefficient and the noncritical phase matching property of potassium niobate allow efficient frequency doubling at a relatively low power of the fundamental, as in our case. The whole experimental set-up is shown in Fig. 7.3.1.

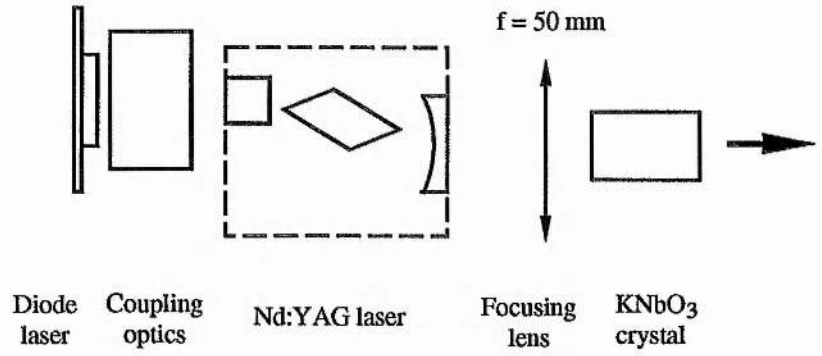

Figure 7.3.1 Experimental set-up of frequency doubling 946-nm wave with $KNbO_3$ crystal

The noncritical phase matching configuration was adopted in our experiment. The $KNbO_3$ crystal had a dimension of (5.1 mm) x b (3.1 mm) x c (3.06 mm). The crystal was mounted in the temperature controlled oven with the a-axis along the oven core axis and the b-axis in the polarisation plane of the 946-nm laser output. A voltage of 100 V was kept across the faces normal to c-axis, whenever the crystal was in use. The optimum temperature of the crystal for noncritical phase matching at 946 nm was found at 185.0 °C.

Due to the insertion of the Brewster angled Q-switch in the laser cavity,

the laser output beam was both astigmatic and elliptical, having, for the tangential and sagittal planes, the apparent waists of 40 μm and 69 μm at the pump input end respectively , and 208 μm and 127 μm at the output coupler respectively. The Boyd and Kleinman focusing requirement, Eq. (6.3.29a), gives the optimum beam waist size for a 5.1-mm long crystal of 11 μm, which implies that a pair of cylindrical lenses with focal lengths of about 40 mm and 25 mm at some distance of 100 mm away from the laser output coupler is required. The result of using such a cylindrical lens pair, however, was not very satisfactory in practice due to the surface losses of the uncoated lenses and the aberrations caused by cylindrical lenses of such short focal lengths. Several spherical lenses with focal lengths of 30 mm, 50 mm, and 70 mm were then tried. The second harmonic generation powers obtained by using the 30-mm focal length lens and the 50-mm focal length lens were the same, and slightly higher than that obtained by using the 70-mm focal length lens, but the second harmonic generation beam quality in the case of using the 30-mm focal length lens was poorer than that in the other two cases, because of the tight focusing in one plane. With the 50-mm spherical lens at 110 mm away from the laser output coupler, the laser beam waists then become 13 μm and 42 μm in the two orthorgonal planes respectively at the centre of the crystal, and 29 μm and 42.8 μm at the input or output surface. This was close to the optimum focusing condition in one plane, but in the other plane, the focusing power was much weaker. In this case, the fundamental electric field can be expressed by

$$E_1(x,y) = E_0 \, e^{-(x^2/w_{0x}^2 + y^2/w_{0y}^2)} , \qquad (7.3.1)$$

where w_{0x} and w_{0y} are the beam waists in the two planes respectively.

Using the fundamental wave power,

$$P_\omega = \frac{1}{2}\sqrt{\frac{\varepsilon_0}{\mu_0}} \int_{-\infty}^{\infty}\int_{-\infty}^{\infty} \left|E_1(x,y)\right|^2 dx\, dy = \sqrt{\frac{\varepsilon_0}{\mu_0}}\, E_0^2 \left(\frac{\pi\, \omega_{0x}\, \omega_{0y}}{4}\right) \quad , \tag{7.3.2}$$

and assuming that the depletion of the fundamental wave due to conversion of its power to 2ω is negligible, we obtain the conversion efficiency, by integrating both sides of Eq. (6.3.9c),

$$\eta = \frac{2\,\omega^2\, d_{eff}^2\, L^2}{\varepsilon_0\, c^3\, n_\omega^2\, n_{2\omega}} \left(\frac{P_\omega}{\pi\, w_{0x}\, w_{0y}}\right) \mathrm{sinc}^2(\Delta k\, L/2) \quad , \tag{7.3.3}$$

where L is the length of the nonlinear crystal, and Δk is the phase mismatch between the fundamental and the second harmonic waves.

The 946-nm laser pulses of 62-ns duration (FWHM) and 76-W peak power were converted to blue light pulses with 42-ns duration and 22-W peak power, which corresponded to an internal peak-power doubling efficiency of 40 %. From Eq. (7.3.3) and Eq. (6.3.24), the peak-power conversion efficiency of 41.5 % can be obtained by using d_{32}=19.5 pm/V, L=5.1 mm, n_ω=$n_{2\omega}$=2.267, and the average beam waists w_{ox}=21 μm and w_{oy}=42.4 μm. The measured external mean power conversion efficiency was 19 %, giving a mean power in the blue of 1.55 mW (1.04 μJ per pulse). The mean conversion efficiency can be increased by increasing the repetition rate, though there is a trade-off between the peak and the mean power in the blue light. Improvements can be made by using anti-reflection coatings to reduce the substantial Fresnel loss of about 15 % associated with each crystal surface.

The pulse narrowing effect of the second harmonic generation can be seen from the pulse traces of fundamental and second harmonic pulses in Fig. (7.3.2). The duration of the blue light pulses was 42 ns, while the duration of the fundamental pulse was 62 ns. This was in excellent agreement with the theoretical predicted 32.5 % narrowing effect. (see the theoretical pulse traces in Fig. 7.3.3, for the case where the Q-switched laser has the initial population inversion, r, of 3.0.)

A photograph of the overall system in operation is included as Fig. 7.3.4. This demonstrates the compactness, relative simplicity, and high intensity of this type of Q-switched all-solid-state blue laser.

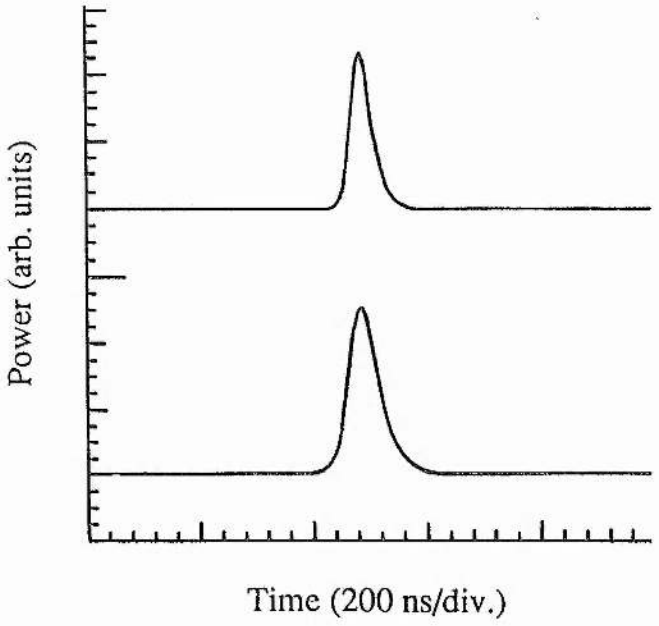

Figure 7.3.2 Fundamental pulse (lower trace) and second harmonic pulse (upper trace)

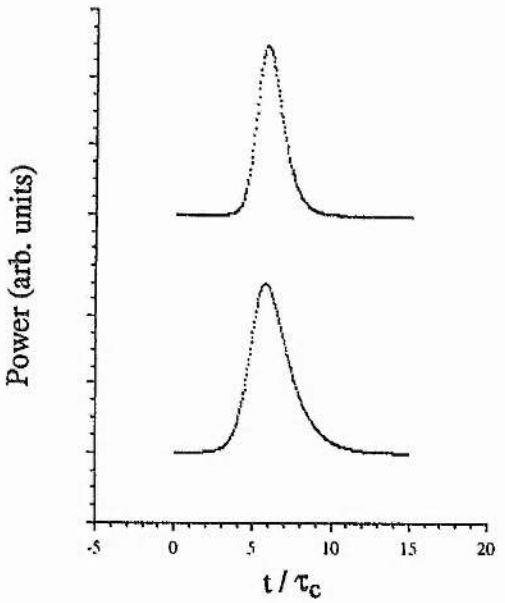

Figure 7.3.3 Theoretical pulse traces for the fundamental and the second harmonic. The initial population inversion (r) is chosen to be 3.0.

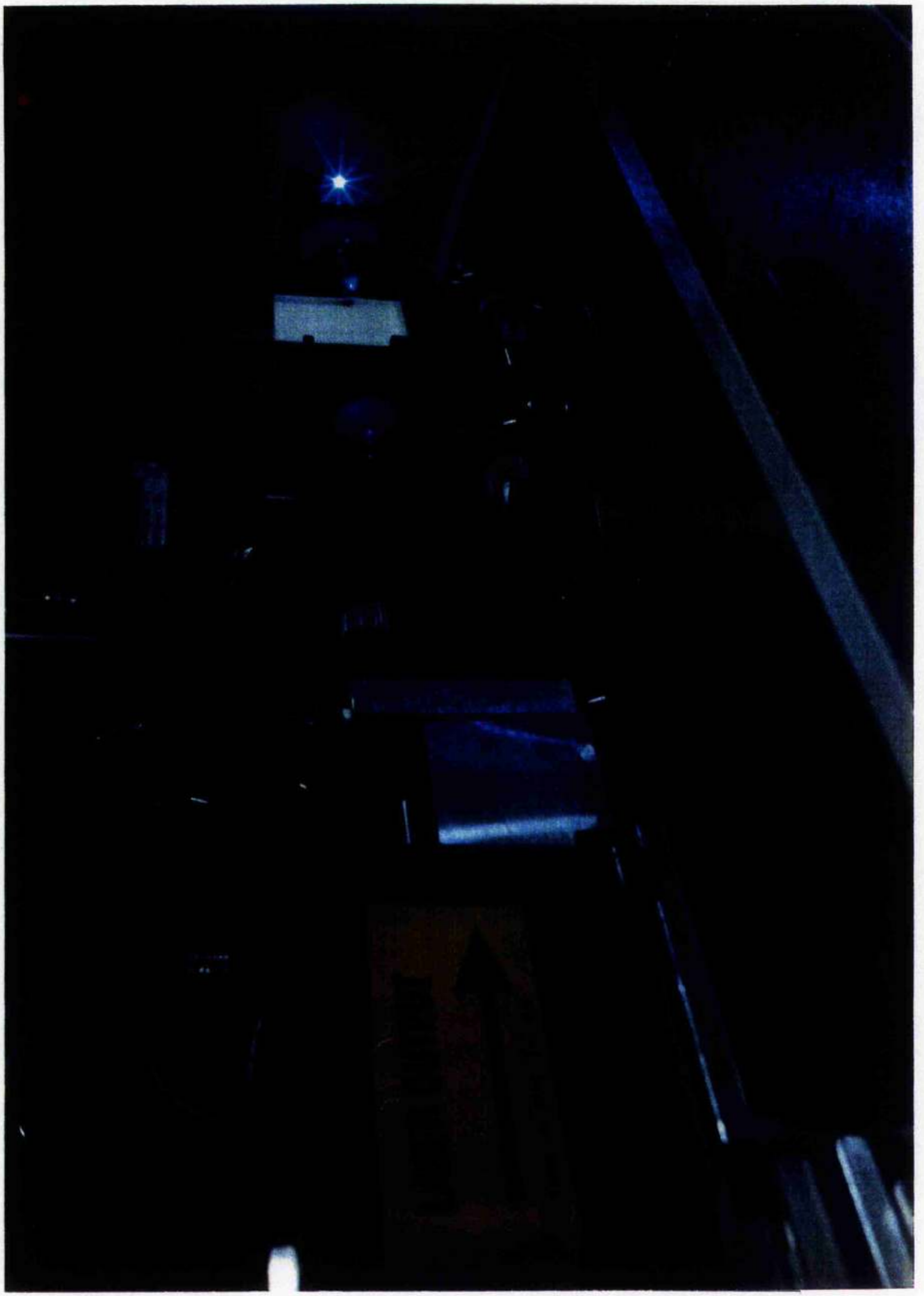

Figure 7.3.4 Photograph of the system in operation

References

[1] R. C. Miller, "Optical second harmonic generation in piezoelectric crystals", *Appl. Phys. Lett.*, Vol.5, No.1, (1964) 17;

[2] R. S. Adhav, S. R. Adhav, J. M. Pelaprat, "BBO's nonlinear optical phase-matching properties", *Laser Focus / Electro-optics*, Sept., (1987) 88;

[3] J. D. Bierlein, "Potassium titanyl phosphate (KTP): properties, recent advances and new applications", *SPIE*, Vol.1104, (1989) 2;

[4] T. Y. Fan, C. E. Huang, B. Q. Hu, R. C. Eckarolt, Y. X. Fan, R. L. Byer, and R. S. Feigelson, "Second harmonic generation and accurate index of refraction measurements in flux-grown KTiOPO4", *Appl. Opt.*, Vol.26, No.12, (1987) 2390;

[5] F. C. Zumsteg, J. D. Bierlein and T. E. Gier, "$K_xRb_{1-x}TiOPO_4$: a new nonlinear optical material", *J. Appl. Phys.*, Vol.47, No.11, (1976) 4980;

[6] M. Vanherzeele, J. D. Bierlein and F. C. Zumsteg, "Index of refraction measurements and parametric generation in hydrothermally-grown $KTiOPO_4$", *Appl. Opt.*, Vol.27, No.16, (1988) 3314;

[7] H. Ito, H. Naito and H. Inaba, "Generalized study on angular dependence of induced second-order nonlinear optical polarizations and phase matching in biaxial crystals", *J. Appl. Phys.*, Vol.46, No.9, (1975) 3992;

[8] C. Chen, Y. X. Fan, R. C. Eckardt and R. L. Byer, "Recent developments in barium borate", *SPIE*, Vol.681, (1986) 12;

[9] R. C. Eckardt, H. Masuda, Y. X. Fan and R. L. Byer, "Absolute and relative nonlinear optical coefficients of KDP, KD*P, BaB_2O_4, $LiIO_3$, MgO:$LiNbO_3$, and KTP measured by phase-matched second-harmonic generation", *IEEE J. Quantum Electron.*, Vol.26, No.5, (1990) 922;

[10] G. D. Boyd, R. C. Miller, W. L. Bond and A. Savage, "$LiNbO_3$: an efficient phase matchable nonlinear optical material", *Appl. Phys. Lett.*, Vol.5, No.11, (1964) 234;

[11] F. Zernike and J. E. Midwinter, *Applied Nonlinear Optics*, John Wiley & Sons,

USA, (1973) 91;

[12] J. G. Bergman, A. Ashkin, A. A. Ballman, J. M. Dziedzic, H. J. Levinstein and R. G. Smith, "Curie temperature, birefringence, and phase-matching temperature variations in $LiNbO_3$ as a function of melt stoichiometry", *Appl. Phys. Lett.*, Vol.12, No.3, (1968) 92;

[13] M. V. Hobden and J. Warner, "The temperature dependence of the refractive indices of pure lithium niobate", *Phys. Lett.*, Vol.22, No.3, (1966) 243;

[14] D. Feng, N. Ming, J. Hong, Y. Yang, J. Zhu, Z. Yang and Y. Wang, "Enhancement of second-harmonic generation in $LiNbO_3$ crystals with periodic laminar ferroelectric domains", *Appl. Phys. Lett.*, Vol.37, No.7, (1980) 607;

[15] A. Feisst and P. Koidl, "Current induced periodic ferroelectric domain structures in $LiNbO_3$ applied for efficient nonlinear optical frequency mixing", *Appl. Phys. Lett.*, Vol.47, No.11, (1985) 1125;

[16] P. W. Haycock and P. D. Townsend, "A method of poling $LiNbO_3$ and $LiTaO_3$ below T_c", *Appl. Phys. Lett.*, Vol.48, No.11, (1986) 698;

[17] G. A. Magel, M. M. Fejer and R. L. Byer, "Quasi-phase-matched second-harmonic generation of blue light in periodically poled $LiNbO_3$", *Appl. Phys. Lett.*, Vol.56, No.2, (1990) 108;

[18] I. Biaggio, P. Kerkoc, L. S. Wu, P. Gunter and B. Zysset, "Refractive indices of orthorhombic $KNbO_3$ Part II: Phase matching configurations for nonlinear optical interactions", submitted to *J. Opt. Soc. Am. B* ;

[19] J. C. Baumert, J. Hoffnagle and P. Gunter, "Nonlinear optical effects in $KNbO_3$ crystals at $Al_xGa_{1-x}As$, dye, ruby and Nd:YAG laser wavelengths", *SPIE*, Vol.492, (1984) 374;

[20] B. Zysset, I. Biaggio and P. Gunter, "Refractive indices of orthorhombic $KNbO_3$ Part I: Dispersion and temperature dependence", submitted to *J. Opt. Soc. Am. B* ;

[21] G. J. Mizell, W. R. Fay and Y. Shimoji, "Advances in the production of $KNbO_3$ crystals", *SPIE*, Vol.968, (1988) 88;

[22] E. Wiesendanger, "Optical properties of $KNbO_3$", *Ferroelectrics*, Vol.1, (1970) 141;

[23] T. Fukuda and Y. Uematsu, "Preparation of $KNbO_3$ single crystal for optical applications", *Jap. J. Appl. Phys.*, Vol.11, No.2, (1972) 163;

[24] S. G. Ingle and A. P. David, "Tailored domain structures in $KNbO_3$ single crystals", *Ferroelectrics*, Vol.97, (1989) 201.

Chapter 8

Conclusions

As one way of developing an all-solid-state blue laser system, we have demonstrated the applicability of frequency doubling the unusual laser line at 946 nm in Nd:YAG. The Q-switched peak power level and both the laser efficiency and the second harmonic generation efficiency attainable on this line demonstrate the potential of the system for some practical applications. Since the 946-nm laser line suffers from reabsorption loss due to population of the lower laser level, its cw laser behaviour was studied both theoretically and experimentally to facilitate optimisation. Modelling of Q-switching on this line was also carried out and some close comparisons were made with the 1064-nm Nd:YAG laser. The models developed and the knowledge gained on this particular laser line, however, can be applied to laser lines in other laser materials which exhibit reabsorption losses due to lower laser level populations.

The theoretical model for a cw quasi-three-level laser system was developed in chapter 3. From the discussion, it is obvious that cooling of the Nd:YAG crystal is an effective way to encourage oscillation on the 946-nm laser line. The model shows that there exists a particular value of crystal length for minimum threshold, which may not be the optimum length from the point of view of maximum output power. This optimum crystal length can, however, be obtained numerically with pump power and output coupler transmission as parameters. By reducing the pump beam size and laser cavity mode size, we see the great improvement in laser performances, which implies the importance of the quality of the pump

beam. Because of the nature of diode lasers, it is difficult to obtain a diffraction-limited beam at high power level at the present time. While the diffraction-limited beam operation with ever-increasing power levels remains a long-standing goal for the diode laser industry, coupling optics are generally required for diode lasers at the moment. In this study, several typical arrangements of coupling optics for diode lasers were investigated. In the experiment, a combination of a collimating lens, an anamorphic prism pair and a focusing lens were used to collimate, circularise and focus the pump beam. With such coupling optics, the astigmatism of the diode laser was also corrected. In order to generate a small mode volume in the Nd:YAG crystal, a hemispherical cavity was used with the crystal located at one end of the cavity. By adjusting the cavity length close to the cavity stability limit, the optimum mode size for matching the pump beam size was obtained. With 360 mW of pump power coupled into the Nd:YAG rod, 28 mW of 946-nm output power was obtained at the Nd:YAG crystal temperature of 5 ^{o}C.

A model of Q-switched quasi-three-level lasers was developed in chapter 4, in which we can see the close resemblance between a quasi-three-level laser and an ideal 4-level laser. The reabsorption loss in a quasi-three-level laser can be regarded as an additional loss to the cavity loss, and the sole effect of the lower laser level population is to increase the pump power requirement to reach threshold. This reduces the ratio of pump power to the threshold pump power, and thus reduces the total extraction efficiency of the laser system. In the experiments, 360 mW of pump power was coupled into the Nd:YAG crystal, which was kept at 5 ^{o}C, when 5.6 μJ pulses of 76-W peak power and 62-ns pulse duration were generated. These experimental results were in excellent agreement with the Q-switched model.

The Q-switched 946-nm laser pulses were frequency doubled in potassium niobate to give a compact, reliable, and efficient blue laser source. The evaluations of several favourable nonlinear crystals showed that $KNbO_3$ is the most efficient second harmonic generator at the fundamental of 946 nm, but there are some special properties associated with this material. In the work, the problems associated with $KNbO_3$ were closely investigated. Precautions were specially taken to prevent the crystal from depoling. Temperature uniformity along the crystal during the period of the heating-cooling cycle is one of the important factors in this respect, since multidomains can be easily observed when the crystal is not evenly heated or cooled. This temperature uniformity requirement decides the heating and cooling rate. In addition to the restriction set by the temperature uniformity, the electric charges induced by changes in temperature is another restriction to the heating / cooling rates, especially during the cooling period, as the direction of the induced electric field during that period is opposite to the applied poling field normally required. If the cooling speed is too fast, the induced field may be sufficient to depole the crystal. In order to prevent the crystal from depoling and to increase the heating / cooling speeds, an external electric field was applied to the crystal. The direction of the field is decided by the polarity of the c-axis of the crystal, which was identified by the induced voltage across the c-axis. The applied external poling field should always be in the same direction as the induced field during the heating-up period. With a $KNbO_3$ crystal of 5.1-mm length, an internal peak-power doubling efficiency of 40 % was attained resulting in a peak power of 22 W in a pulse of duration 42 ns.

As higher power and better beam quality diode lasers become available, the present system has the potential for scaling to much higher power levels, which may be extremely useful in applications such as undersea

communications and large screen projectors. Although diode lasers and frequency converted diode lasers may in future address most applications requiring continuous-wave sources, for those applications requiring pulses of high peak power, the diode-laser-pumped solid-state laser will still be the preferred route, as the solid-state laser can store pump energy and release it rapidly in the form of a Q-switched pulse. We regard our demonstration of a blue pulsed laser as the first-steps along this path which is a path that becomes easier and more efficient as the available pump powers increase. These first steps though, have pointed the way in terms of potentials and precautions.